TECHNICAL UNIVERSITY OF CRETE

SCHOOL OF ELECTRICAL AND COMPUTER ENGINEERING

Diploma Thesis

Dielectric Properties of Pole Insulation of Traction Motors Under Ageing with Thermal Cycling

Author:

Dimitrios Chronopoulos

Thesis Committee:

Assoc. Prof. Konstantinos Gyftakis (Supervisor)

Prof. Eftychis Koutroulis

Dr. Eleftheria Sergaki

Chania, 2024

ABSTRACT

This diploma thesis investigates the dielectric properties of pole insulation in traction motors subjected to aging through thermal cycling. It is a part of the TEAMstress project at the Technical University of Crete, which aims to understand the degradation processes of insulating materials in traction motor poles. The project encompasses the development of quality testing procedures, model design, and analysis of various aging mechanisms, with a particular focus on thermal cycling stress in this thesis. Impedance spectroscopy serves as the monitoring technique utilized throughout the project to generate results. The initial section of the thesis provides a concise overview of electric vehicles and their traction motors. It also examines the permanent magnet synchronous motor utilizing the YASA topology, characterized by axial flux pathing between two external rotors and an internal stator, which is the specific traction motor under investigation. Following this, the thesis outlines the typical faults that electric motors may encounter. It delves into fault generation, focusing on prevalent sequences such as inter-turn short circuits, eccentricity, and demagnetization. Additionally, it discusses the widely employed diagnostic methods aimed at early fault detection. Subsequently, the thesis delves into pole insulation monitoring and thermal aging. It describes the insulation system, diagnostic tests to assess insulation condition, and analyzes the thermal cycling mechanism, along with relevant literature on thermal cycling testing. During the experimental process, impedance spectroscopy is the primary method for monitoring pole insulation condition. The thesis outlines the FRAX analyzer instrument and the procedure for conducting experimental tests. The section on performed work begins with the development of a complex equivalent circuit for the pole specimen. It then explores thermal cycling stress and analyzes results using impedance spectroscopy plots, Nyquist diagrams and breakdown voltage distributions. The thesis also investigates fixed thermal degradation to understand the absence of thermomechanical effects and examines multi-stress mechanisms, including electromechanical stress, using an in-house designed mechanical accelerator. In summary, this thesis provides insights into thermal cycling stress and other degradation mechanisms while examining impedance spectroscopy as a monitoring technique for assessing pole insulation condition.

ACKNOWLEDGMENTS

CONTENTS

1) ELECTRIC VEHICLES AND TRACTION MOTORS

1.1 Electric Vehicles [1], [2]

Electric vehicles (EVs) have emerged as a revolutionary and environmentally sustainable alternative to traditional internal combustion engine vehicles. It is a fact that, nowadays, combustion engines are the most prevailing type of vehicle running on the road. Although combustion engines currently dominate the roads, their reliance on fossil fuels has prompted a paradigm shift toward electricity as the primary energy source. The escalating environmental concerns arising from the exhaust emissions of conventional vehicles have spurred experts in the automotive sector to explore transportation alternatives that significantly reduce environmental pollution. In this context, electric vehicles utilizing clean energy and electrical power have garnered increasing interest within the realm of automotive technology. This heightened attention is attributed to their distinct advantages, including zero carbon emissions, heightened efficiency, cost-effectiveness, and the abundance of renewable resources.

The functionality of electric vehicles (EVs) mirrors that of traditional gasoline vehicles, with the key distinction being the use of electric motors instead of a gasoline-powered internal combustion engine (ICE) for propulsion. Rather than storing energy in a tank as gasoline, electric vehicles store energy as electricity in a battery. Advances in battery technology have played a crucial role in the widespread acceptance of electric cars. Modern electric vehicles are equipped with high-capacity batteries ensuring extended driving ranges and alleviating concerns related to range anxiety—the fear of depleting the battery charge before reaching a charging station. Ongoing research and development efforts in battery technology aim to enhance energy density, charging speed, and overall performance, making electric cars an increasingly viable and convenient option for consumers.

The sales figures for electric vehicles (EVs), especially battery electric vehicles (BEVs) and plug-in hybrid vehicles (PHEVs) are witnessing a significant surge. This trend is attributed to increasingly

stringent regulations targeting pollutant and CO_2 emissions, coupled with government initiatives providing subsidies for the acquisition and use of such vehicles. Projections indicate a noteworthy trajectory in the global annual sales of electrified powertrain vehicles, escalating from 2.8 million units in 2019 to capturing one-third of the market share by 2025. This anticipated growth is expected to translate into approximately 35 million vehicles sold in the year 2025 signaling a substantial shift towards sustainable transportation solutions [1].

1.2 Traction Motors [1], [2], [3]

A traction motor is a vital component in electric and hybrid vehicles, responsible for converting electrical energy into mechanical motion to propel the vehicle. Serving as the driving force, this motor significantly influences the overall performance of the vehicle by efficiently utilizing the power stored in the batteries to provide the necessary torque for wheel propulsion. Essentially, the electric motor can be considered the heart of an electric vehicle. With continuous technological advancements, the trajectory of sustainable and high-performance transportation across various sectors is expected to be increasingly shaped by the evolving role of traction motors.

The importance of a vehicle's traction system becomes apparent when aiming to match the competency of their fuel-driven counterparts. Vehicles powered by internal combustion (IC) engines, relying on traditional fuels, exhibit robustness and resilience, effortlessly navigating through challenging conditions such as rough terrains, abrupt braking, sudden jerks, and uneven road surfaces. These attributes highlight the durability and adaptability of fuel-driven vehicles, underscoring the necessity of developing a traction system for alternative power sources capable of seamlessly handling similar demanding scenarios.

The global shift towards hybrid and battery electric vehicles signifies a monumental stride, fundamentally reshaping perceptions of the technology propelling these electric machines. Modern electric traction motors introduce a paradigm shift compared to the advancements seen in industrial electric motors over recent decades, particularly in operating range and drive cycle

requirements. Beyond disparities in power and torque-speed ranges within the operating field, challenges extend to encompass harsh environmental conditions, including shock, vibration, operating temperature cycles, and service life specifications. Consequently, addressing these diverse demands necessitates distinct design approaches, specialized material applications, and the establishment of mass production facilities tailored to the unique requirements of electric traction motors.

In broad terms, the specifications for driving motors in electric vehicles encompass compact dimensions, lightweight construction, high power and torque density, high overload capacity, efficiency across a broad speed spectrum, adaptability to diverse environmental conditions, exceptional reliability, and cost-effectiveness. The design and characteristics of traction motors can vary depending on the specific application and vehicle type. A traction motor in an electric vehicle needs to satisfy a different set of operating criteria compared to those used in industrial settings, where most loads are constant and classified. On roads, electric vehicles may need to continuously change speed, increase torque on slopes, and apply sudden brakes, among other dynamic demands.

Currently, countries around the world predominantly utilize four types of electric motors for electric vehicle driving:
- ❖ Direct Current Motors (DCM)
- ❖ Induction Motors (IM)
- ❖ Permanent Magnet Synchronous Motors (PMSM)
- ❖ Switched Reluctance Motors (SRM).

The performance of the four driving motors has been studied and discussed in [2] & [3] and the results are shown in the table below:

Table 1.1: Characteristics of traction motors
[3]

Types	DCM	IM	PMSM	SRM
Power Density	Low	Medium	High	Low
Efficiency (%)	Medium	High	V. High	Low
Noise	High	Medium	Low	High
Reliability	Bad	Good	Excellent	Good
Controllability	Excellent	Good	Good	Good
Mechanical Strength	Bad	Good	Good	Excellent
Cost	Low	Medium	V. High	Low
Overall Performance	Bad	Medium	Excellent	Bad

By comparing various types of existing electric vehicle driving motors, Permanent Magnet Synchronous Motors (PMSM) stand out due to their high efficiency, high power density, and superior reliability, making them the most fitting choice for electric vehicles. Other advantages include compact structure, diminutive size, lightweight construction, and low inertia. The abovementioned studies align with reality, as a matter of fact, in the 21st century, PMSM has emerged as the preferred motor for drive systems. Major automotive enterprises consistently refine their approach to enhance motor performance by optimizing structures, augmenting permanent magnet magnetism, and reducing costs, among other factors. This ongoing commitment to improvement underscores the significance of PMSM in the evolution of electric vehicle technology.

1.3 Synchronous Machines [4]-[8]

Synchronous machines and asynchronous machines, commonly called induction machines, constitute the primary categories within AC machines.

In the realm of electrical power systems, synchronous generators, a subset of synchronous machines, play a pivotal role in power generation. They are extensively deployed in large-scale power plants, contributing significantly to the equilibrium and stability of electrical grids.

Conversely, synchronous motors exhibit exceptional efficiency, particularly in domains demanding precision, offering high efficiency and contributing to an enhanced power factor. This attribute renders them advantageous in applications related to transportation and automobility.

Some foundational insights into synchronous machines, covering aspects such as synchronous speed, structural considerations, and cooling mechanisms are provided. Furthermore, recognizing the dominance of synchronous motors in the automotive industry, a concise exploration of their operational dynamics is presented.

Synchronous Speed

As the name suggests, in synchronous machines, the rotor's rotational speed synchronously matches the revolving magnetic field, invariably resulting in a slip of zero. Consequently, the speed of a synchronous motor remains unaffected by variations in load and voltage, hinging solely on the interplay of frequency and the number of poles.

It is given by the formula:

➢ $n_s = \frac{60 \cdot f_s}{p}$

where:

- n_s is the synchronous speed in revolution per minute (r.p.m)
- f_s is the supply frequency
- p is the number of pair poles of the machine

＋ <u>Structure</u>

1) Stator

The stator in a three-phase synchronous machine is the immobile component housing a three-phase winding, strategically positioned at 120° electrical intervals around its perimeter. Within the stator, an armature winding, energized by an AC source, is situated to facilitate the machine's operation.

2) Rotor

The rotor constitutes the rotating segment of the synchronous machine, typically comprising a field winding constructed from coils. Positioned within the rotor, the field winding is energized by a DC source.

Synchronous machines exhibit two primary rotor structures: cylindrical rotor machines and salient-pole rotor machines. The chosen rotor type significantly impacts the machine's performance characteristics and its suitability for various applications.

o   Cylindrical Rotor Machines:

In cylindrical rotor synchronous machines, the rotor adopts a cylindrical shape, with the field winding uniformly distributed across its entire surface. These machines are characterized by a substantial core length, small diameter, and a consistent air gap along the perimeter. The cylindrical rotor design inherently generates balanced mechanical forces, diminishing the likelihood of rotor vibrations. Consequently, these machines find widespread application in high-speed and high-power settings, such as large power plants and industrial facilities.

o   Salient-Pole Rotor Machines:

In contrast, salient-pole rotor machines feature projecting poles with the field winding concentrated in these areas. These machines exhibit a smaller core length, larger diameter, and a non-uniform air gap, resulting in irregular magnetic resistance based on the air gap. The presence of salient poles introduces the potential for unbalanced mechanical forces, leading to vibrations.

Careful design and damping techniques are essential to mitigate these vibrations. Salient-pole synchronous machines are commonly employed in applications requiring variable speed operation, such as hydroelectric generators, where variations in water flow and turbine speed are prevalent.
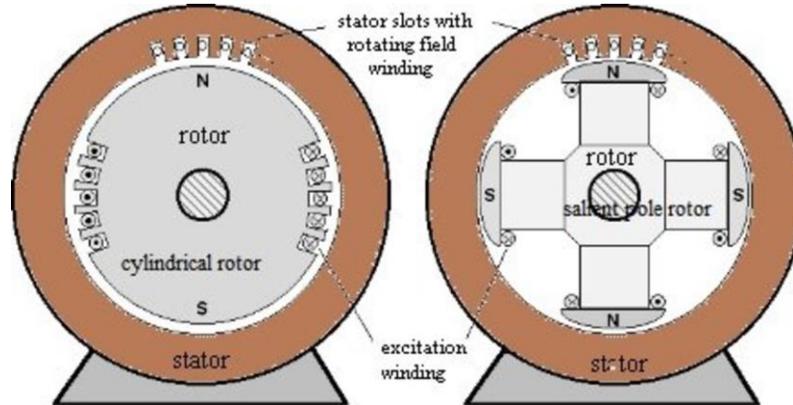

Figure 1.1: Cylindrical rotor & salient pole rotor
https://discover.hubpages.com/technology/Synchronous-machines-Construction-Principle-of-operation

3) Excitation System

The excitation system (ES) plays a crucial role in synchronous machines, residing on the rotor and furnishing essential DC to the field winding. Beyond this fundamental function, it also controls the field voltage, field current, and reactive power flow within the system. Moreover, the excitation system significantly enhances stability during synchronous machines' startup phase.

Based on [5]-[8], over the years, numerous excitation systems (ESs) and evolving trends have been meticulously studied and implemented in synchronous machines. Some systems have been discarded, while others have undergone improvements and further refinements. Notably, there exists no standardized categorization of excitation systems, with each author presenting a variety of types.
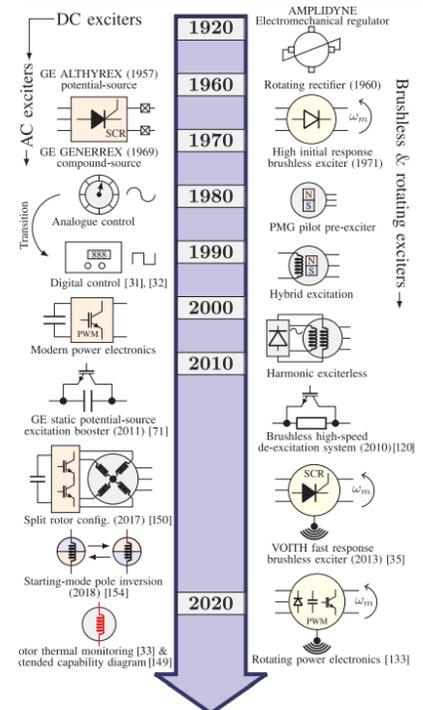

Figure 1.2: Development history of excitation systems [8]

12

The earliest excitation systems were founded on DC exciters, utilizing DC generators as a power source. These generators were driven by a separate motor or the primary alternator shaft, delivering DC to the field through slip rings. Despite representing early commercial systems (from the 1920s to the 1960s), DC excitation methods now hold primarily historical value, having been surpassed by AC exciters.

Presently, static exciters take precedence, particularly in large synchronous generators with power ratings in the order of several MVAs. These systems employ controlled rectifiers connected via slip rings and brushes to the generator's field coil. While dynamic in performance, static systems rely on carbon brushes, necessitating a higher degree of maintenance. Consequently, they are less common in small machines or challenging environments.

In contrast, brushless excitation systems eliminate slip rings and brushes. Instead, they feature a rotating exciter with a three-phase winding on the rotor, mounted on the primary machine shaft. This design not only minimizes maintenance requirements but also enhances overall reliability.

Ultimately, the selection of the excitation system hinges on critical factors such as the generator's size, intended application, and the desired level of control. This intricate decision-making process ensures that the excitation system aligns seamlessly with the specific requirements of the synchronous machine.

Cooling

Cooling plays a pivotal role in the reliable operation of synchronous machines due to the substantial currents flowing through their windings, generating considerable resistive losses. Efficient cooling is paramount in preventing performance degradation, insulation breakdown, and potential failure, making it a critical aspect of design and operation.

o   Forced-Air Cooling:

Applied primarily to synchronous machines up to 50 MVA, forced-air cooling utilizes strategically placed fans to augment airflow around the machine. This enhances convective heat dissipation, ensuring that critical components like windings and the core receive adequate cooling.

o   Hydrogen Cooling:

Hydrogen, with its superior cooling properties compared to air, is employed in machines with power ratings up to 250 MVA. The method involves cooling hot hydrogen before reintroducing it into the machine's interior, leveraging its higher thermal conductivity and specific heat capacity for enhanced cooling efficiency.

o   Water/Oil Cooling:

In larger synchronous machines with higher power ratings, where cooling is even more crucial, water/oil cooling becomes a preferred method. This direct cooling approach achieves lower temperatures, substantially extending insulation durability and the machine's overall life expectancy.

Efficient cooling is indispensable in averting overheating and ensuring the continuous, reliable operation of synchronous machines. Continuous research and improvements are directed towards cooling systems to enhance their effectiveness. The selection of a cooling method is contingent on factors such as machine size, power rating, operating environment, and specific application requirements. This nuanced approach ensures that the chosen cooling solution aligns seamlessly with the unique demands of the synchronous machine in question.
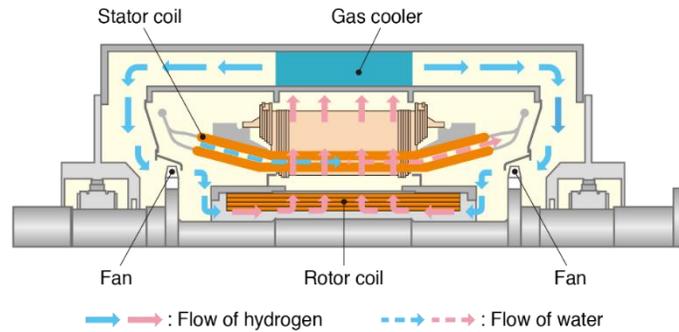
Figure 1.3: Cooling structure
https://www.mitsubishielectric.com/eig/energysystems/products/pg/generator/index_03.html

Principle of operation

In a nutshell, the synchronous motor operates through a dynamic interplay of constant and rotating magnetic fields, ensuring a consistent speed profile. The rotor of synchronous motors generates a steadfast magnetic field, while the stator produces a revolving magnetic field when energized by a three-phase AC supply. This revolving magnetic field rotates at a fixed speed tied to the power frequency, known as synchronous speed. In operation, the coils of the rotor are powered by direct current, generating a magnetic field with alternating polarity akin to magnets.

Assuming an initial rotation is imparted to the rotor in the same direction as the revolving magnetic field (RMF), a harmonious interaction occurs. The opposite poles of the stator and rotor attract, compelling the rotor to rotate at synchronous speed. This rotation is facilitated by the Laplace force developed in the conductors, ensuring synchronization.

However, in the absence of initial rotation, a different scenario unfolds. The North Pole of the rotor is initially attracted by the South Pole of the RMF, initiating movement in the same direction. Due to rotor inertia, the starting speed is minimal. Subsequently, as the South Pole of the RMF replaces the initial North Pole, a repulsive force hinders further progress. This stalling effect prevents the rotor from initiating rotation, potentially leading to vibrations that could cause damage. Thus, the synchronous motor's behavior is contingent on the interplay of magnetic forces, emphasizing the significance of initial rotor conditions in its operational dynamics.

Starting the motor

As highlighted earlier, synchronous motors lack inherent self-starting capabilities. Initiating the operation of a synchronous motor requires transitioning it from a stationary state to its synchronous speed, enabling it to synchronize with the power supply frequency.

There are two main methods for starting a synchronous motor: one involves incorporating damper windings, while the other utilizes a variable frequency inverter.

To enable self-starting in a synchronous motor, they are equipped with damper windings on the rotor, forming a cleverly designed squirrel cage arrangement. Initially, the rotor field coils remain unenergized, yet eddy currents induced in the squirrel cage bars generate torque, setting the rotor into motion akin to an induction motor. Once the rotor reaches its maximum speed, the rotor field coils are energized. As discussed earlier, this causes the rotor poles to lock onto the poles of the revolving magnetic field (RMF), initiating rotation at the synchronous speed. At this point, there is zero relative motion between the squirrel cage and the RMF, resulting in no current or force on the squirrel cage bars. This lack of interference ensures the synchronized operation of the motor.

Advancements in electronic components, particularly inverters, have facilitated modifications to both the frequency and power supply voltage. This technological enhancement allows the motor to initiate from a low frequency, gradually increasing the frequency until the motor attains its synchronous speed. This gradual frequency adjustment results in a slowly rotating field, enabling the rotor's poles to effectively keep pace with the synchronous speed.
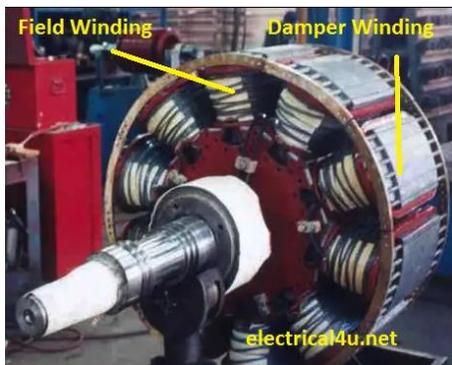

Figure 1.4: Damper winding
http://ww25.bakemotor.org/what-are-the-uses-of-damper-winding-in-a-synchronous-motor/?subid1=20240116-2243-430c-a992-dffd9bb9029a
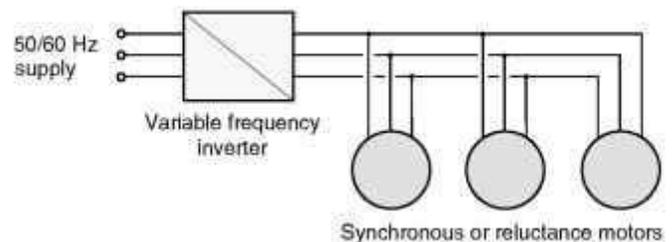

Figure 1.5: Variable frequency inverter
https://learn4electrical.altervista.org/synchronous-motor-and-methods-of-starting-a-synchronous-motors/

➕ Common types of Synchronous Motor

Considering applications and characteristics, various synchronous motor types are commonly utilized:

o   Permanent-Magnet Synchronous Motor (PMSM):

A PMSM employs embedded permanent magnets in the rotor, establishing a constant magnetic field. Known for high efficiency and precise control, it finds applications in diverse fields such as robotics, electric vehicles, and household appliances.
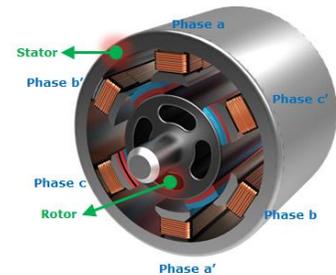

Figure 1.6: Permanent magnet motor
https://www.linquip.com/blog/types-of-synchronous-motors/

o   Reluctance Motor:

Operating on the principle that an unrestrained piece of iron moves to complete a magnetic flux path with minimum reluctance, this motor generates torque by increasing reluctance between rotor poles and the stator magnetic field. A squirrel-cage winding in the rotor facilitates startup by providing torque below synchronous speed.
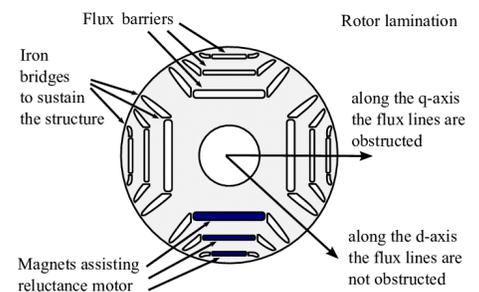
Figure 1.7: Reluctance motor
https://www.linquip.com/blog/types-of-synchronous-motors/

o   Hysteresis Motor:

In Hysteresis Motors, the rotor is composed of ferromagnetic material with high hysteresis loss. The stator incorporates main and auxiliary windings, producing a revolving magnetic field from a single-phase supply. These self-starting motors, devoid of additional windings, are designed for sub-fractional horsepower ratings. They excel in applications where maintaining a constant speed is crucial, such as servomotors and timing motors, particularly in scenarios requiring high torque at low speeds.
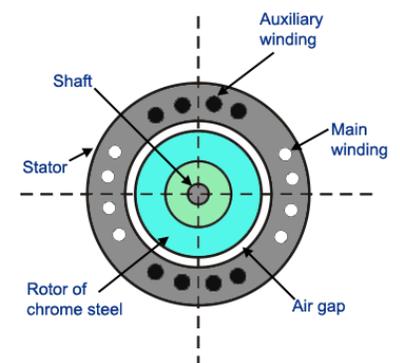
Figure 1.8: Hysteresis motor
https://www.linquip.com/blog/types-of-synchronous-motors/

This overview offers insight into the various synchronous motors designed to meet specific operational requirements, with a later, more in-depth discussion on Permanent-Magnet Synchronous Motors (PMSMs).

1.4 Permanent Magnet Synchronous Motors

A Permanent Magnet Synchronous Motor (PMSM) is an electric motor utilizing permanent magnets either embedded in or affixed to the rotor to generate a magnetic field. The structure and functioning of PMSMs resemble that of synchronous motors. The stator is energized with three-phase AC power, producing a rotating magnetic field. Subsequently, the permanent magnets on the rotor interact with this field, prompting the rotor to track the rotating magnetic field, thereby initiating motor rotation.

The Permanent Magnet Synchronous Motor (PMSM) is renowned for its uncomplicated structure, reliable performance, compact dimensions, lightweight design, low inertia, swift response, high power factor, and high power density. This makes it the preferred choice for electric vehicles. However, PMSMs present challenges, including cost considerations and the temperature sensitivity of permanent magnets.

➕ Permanent Magnets [9]-[11]

Magnets are crafted from magnetic materials, primarily comprising various metallic alloys. The classification of these magnetic materials hinges on their relative permeability (μ_r), which is intricately tied to the internal atomic structure and the extent of magnetization occurring within the material. There are three principal categories for classifying magnetic materials: ferromagnetic materials, paramagnetic materials, and diamagnetic materials.

Ferromagnetic materials boast notably high positive values of magnetic permeability, displaying a robust attraction to magnetic fields and retaining their magnetic properties even after the external field is removed. The relative permeability of ferromagnetic materials can range from a few hundred to several thousand, exhibiting a highly nonlinear behavior.

Those ferromagnetic materials that easily undergo magnetization are labeled as soft magnetic materials. These materials exhibit a steeply rising magnetization curve, and a relatively modest and narrow hysteresis loop, and find applications in devices such as inductors, motors, actuators, transformers, sonar equipment, and radars.

On the other hand, ferromagnetic materials characterized by a gradually rising magnetization curve, a large hysteresis loop area, and substantial energy loss during each cycle of magnetization are termed hard magnets or permanent magnets. The demagnetization characteristic of permanent magnets is effectively described by examining the second quadrant of the hysteresis loop, positioned between remanence and coercive force. This quadrant is particularly valuable for elucidating the load characteristic as it intersects with the operating point (H_L, B_L) [9].
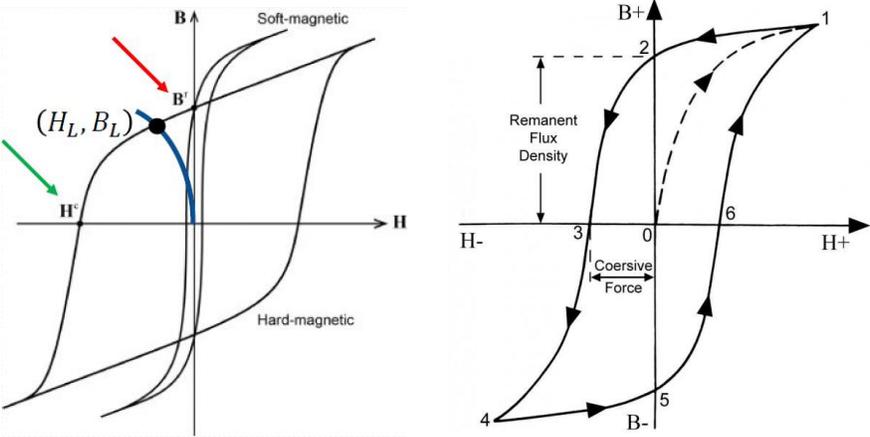
Figure 1.9: Hysteresis loop
[9]

The selection of permanent magnets for a Permanent Magnet Synchronous Motor (PMSM) is crucial, and various types of permanent magnet materials come with their distinct characteristics. Commonly used permanent magnet materials in PMSMs include Neodymium Iron Boron (NdFeB) magnets, Samarium Cobalt (SmCo) magnets, Aluminium Nickel Cobalt (AlNiCo), and ferrite magnets.

o   Neodymium Iron Boron (NdFeB):

Sumitomo Special Metals patented the sintered NdFeB hard magnetic material in 1983, marking a significant advancement in electric motor performance. Neodymium, part of the Light Rare Earth Elements (LREE) family, contributes to these magnets' exceptional performance, characterized by high magnetic strength, impressive coercivity and energy product, and reliable temperature stability.

o   Samarium Cobalt (SmCo):

Developed in the 1970s, SmCo magnets find frequent application in aerospace contexts due to their ability to withstand higher temperatures compared to NdFeB magnets without undergoing demagnetization. Despite this advantage, SmCo magnets are often costlier than NdFeB magnets and involve the use of the rare earth material Samarium, coupled with the expensive Cobalt.

o   Aluminium Nickel Cobalt (AlNiCo):

Originating in the 1930s, AlNiCo magnets offer high remnant flux densities. However, their remarkably low coercivity poses a significant risk of demagnetization, rendering them less favorable for high-power-density electrical machines.

o   Ferrite Magnets:

Ferrite magnets, a choice since the 1950s, are composed of Iron Oxide in conjunction with metals like Strontium, Barium, or Cobalt. While these magnets have lower magnetic strength, they are cost-effective. However, they are susceptible to demagnetization, especially at lower temperatures.

Comparison among various types of permanent magnet materials can be illustrated through three distinct figures [9], [10]. The first figure portrays the Maximum Energy Product, a metric gauging the magnetic energy stored per unit volume within a magnetic material. This value is derived from the product of a material's maximum residual magnetic flux density (degree of magnetization) and its coercivity (capacity to resist demagnetization after magnetization). The second figure

provides separate depictions of the remnant flux density and coercivity for a comprehensive understanding. Lastly, the third figure illustrates the linear demagnetization curve for these diverse permanent magnets.
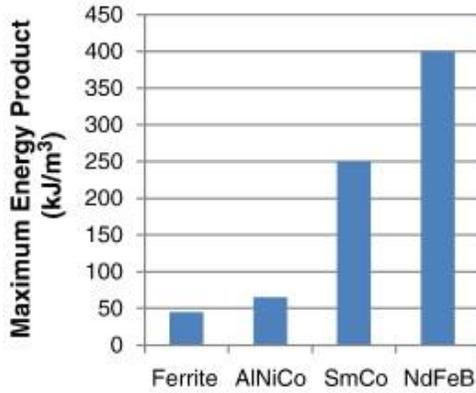

Figure 1.10: Maximum energy product [10]
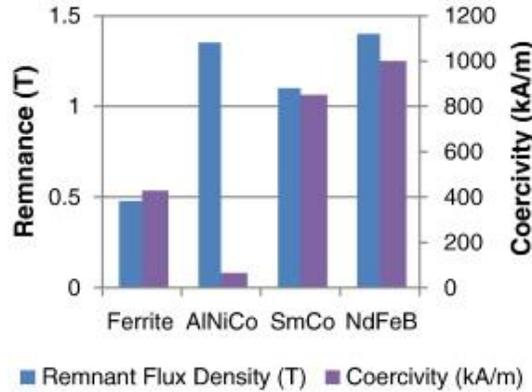
Figure 1.11: Remnant flux density & coercivity [10]
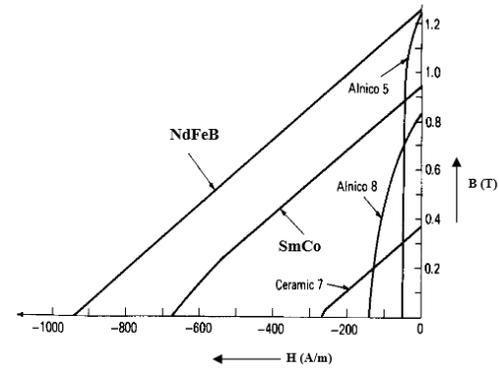
Figure 1.12: Demagnetization curve [9]

The distinctive characteristics of hard magnetic material Neodymium Iron Boron (NdFeB) offer noteworthy performance advantages not achievable with alternative technologies, primarily due to its significantly elevated Maximum Energy Product, coercivity, and remnant flux density. In the context of an electric traction motor, NdFeB magnets facilitate the generation of a potent magnetic field within a remarkably compact volume. This capability enables the development of electric traction motors that are not only compact but also possess high torque and power density.

It is noteworthy that Dysprosium, a Heavy Rare Earth Element (HRE), plays a pivotal role in enabling NdFeB magnets to operate effectively at elevated ambient temperatures [10]. Dysprosium is incorporated into NdFeB to enhance magnet coercivity, preventing demagnetization under conditions of high temperatures and flux weakening. However, it is essential to acknowledge that Dysprosium also significantly contributes to the overall cost of NdFeB magnets.

⬥ Types of Permanent Magnet Synchronous Motors [1], [3]

Permanent Magnet Synchronous Motors (PMSMs) can be divided into two main types based on the positioning of the permanent magnets: Surface-Mounted PMSMs (SPMSMs) and Interior PMSMs.

o   Surface-Mounted PMSM (SPMSM):

In this design, permanent magnets are attached to the rotor's outer surface, facing outward. SPMSMs are commonly employed in applications where cost-effectiveness and reliability are critical. Despite having a simple structure and high magnetic density, they exhibit drawbacks such as poor stability, limited magnetic flux, a restricted maximum velocity range, and increased loss levels.
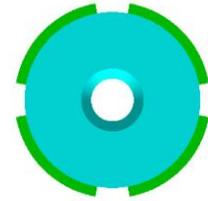
Figure 1.13: Surface-Mounted [3]

o   Interior PMSM (IPMSM):

IPMSMs feature permanent magnets embedded within the rotor core, providing better protection and enhancing overall motor robustness. This design is often chosen for applications that require a balanced combination of cost, efficiency, and durability. IPMSMs offer advantages such as enhanced structural temperature and swift response, but they may have a higher magnetic leakage coefficient.
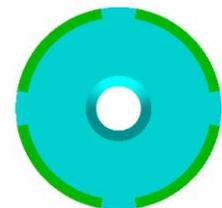
Figure 1.14: Interior [3]

Interior permanent magnets are typically classified into several categories, including I-type, V-type, V+I type, Double V-type, and Inset Radial type. These classifications are based on the shapes of the magnets and their positioning on the rotor. The illustrations below showcase the distinct structures of these various permanent magnet configurations [3].

I type   *V type*   *V+I type*   *Double V type*   *Inset Radial Type*

Figure 1.15: Interior PM classes [3]

The authors of [3] conducted a comprehensive study on six structures (Surface-mounted type, I-type, V-type, V+I type, Double V-type, and Inset Radial type). Throughout the investigation, consistency was maintained in the stator structure, amount of permanent magnet (PM), input current, voltage, and PM weight. The focus of the study was on altering the PM structure and subsequently comparing the resulting performance parameters.

Table 1.2: Parameter performance of PM structures
[3]

Performance parameter	I-type	V type	V+I type	Double V type	Surface-mount	Inset Radial
Magnet mass (kg)	1.966	1.962	1.965	1.965	1.964	1.964
Peak Power (kW)	241.48	118.76	274.51	267.67	298.09	297.43
Continuous power @ knee (kW)	157.31	93.07	180.53	178.46	177.29	192.20
Continuous Knee point (rpm)	9500	9000	9000	9500	8500	9000
Max Speed (rpm)	15000	15000	15000	15000	15000	15000
Peak Torque (Nm)	247.34	142.21	281.79	268.48	287.11	296.20
Continuous Torque @ knee (Nm)	166.92	98.75	191.54	181.65	197.39	204.45
Continuous Torque @ max speed (Nm)	120.34	48.22	125.85	125.47	27.41	101.29
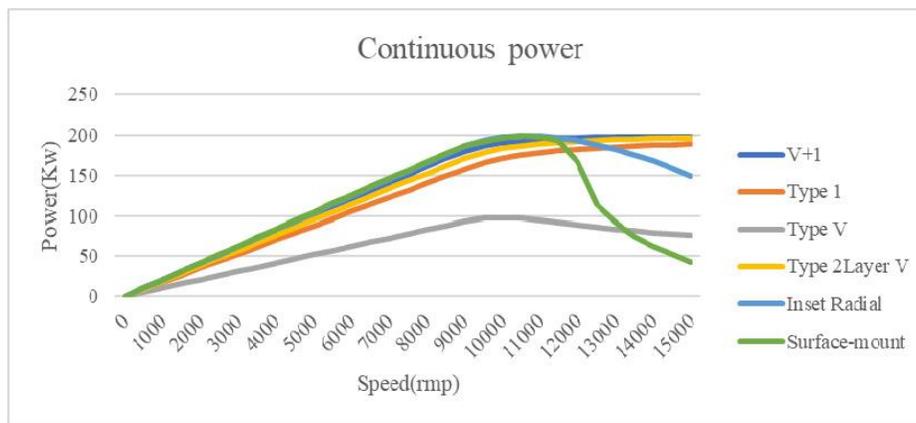
Figure 1.16: Power-Speed characteristic of PM structures
[3]

To establish a connection with the automobility industry, the study presented in [1] delves into the examination of ten traction motors utilized in battery electric and full hybrid vehicles. The primary focus centers on a detailed comparison of the rotor lamination design, specifically emphasizing motors with buried permanent magnets. These ten motors employ the structures mentioned above.

An overarching observation reveals a commonality among all motors, featuring buried magnets and specific rotor structures known as flux barriers. This design strategy serves a dual purpose: minimizing the application of magnet material while incorporating flux barriers to harness reluctance torque. This approach enables a broad constant power speed range for field weakening operation. Notably, the study highlights the widespread utilization of various rotor structures.

The incorporation of cavities in the rotor sheets, surrounding and beneath the permanent magnets, primarily serves to enhance the electromagnetic performance of the motor. This enhancement is achieved by augmenting reluctance torque and diminishing torque ripple. Moreover, particularly in recent designs, the cavities below the magnets contribute to weight reduction and facilitate improved air cooling. Ultimately, the precise design of these cavities involves a delicate trade-off between guiding magnetic flux for torque production, reducing torque ripple, ensuring mechanical strength, and managing the rotating weight of the motor.
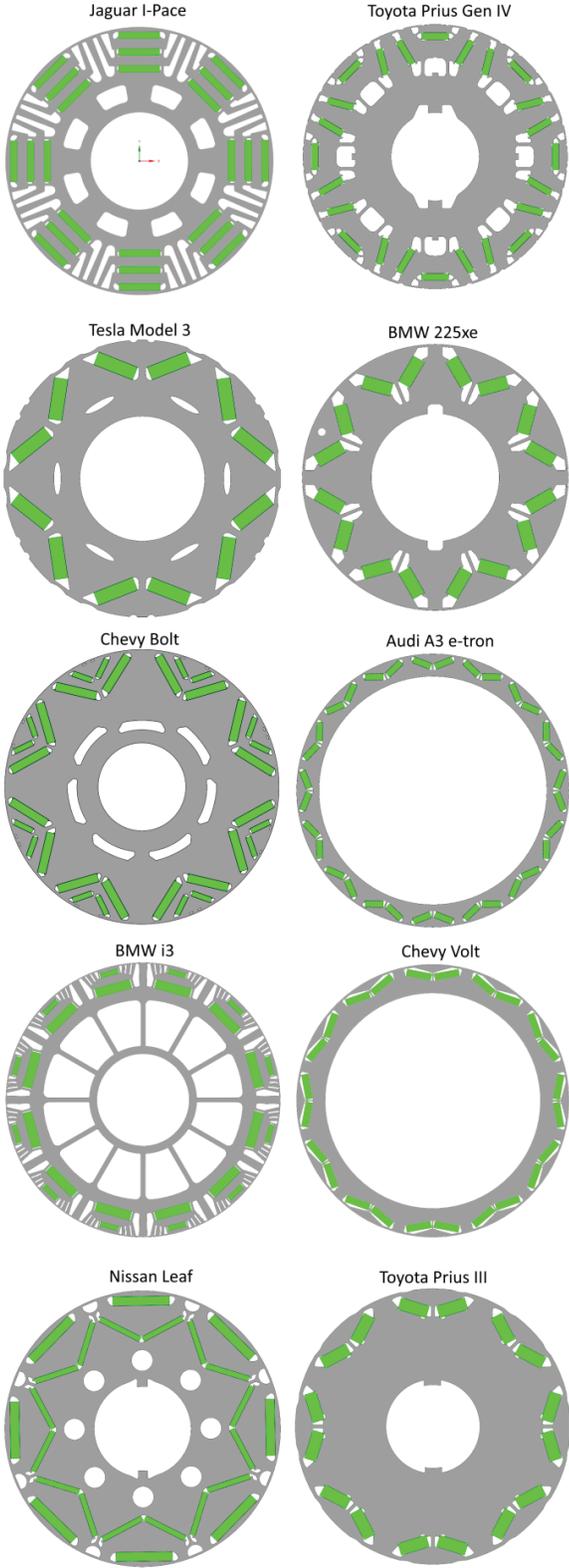

Figure 1.17: Traction motors' structure utilized in automobility [1]

Radial Flux Permanent Magnet Synchronous Motors (RFPMSM) and Axial Flux Permanent Magnet Synchronous Motors (AFPMSM) are two distinct motor designs characterized by the direction of the magnetic flux within the motor.

o   Radial Flux Permanent Magnet Synchronous Motor (RF PMSM):

Radial flux motors, as the name suggests, have a magnetic flux path that follows a radial direction within their structure. The stator and rotor are arranged radially, with the magnetic flux flowing from the motor's center to its periphery, perpendicular to the shaft. Permanent magnets are typically embedded circumferentially on the rotor.

With a rich history of successful applications, radial flux motors are known for their well-established and refined technology. Renowned for robust and reliable performance, they are suitable for applications requiring consistent power delivery. However, the trade-off is a larger and bulkier design.

o   Axial Flux Permanent Magnet Synchronous Motor (AF PMSM):

The stator and rotor are oriented axially in axial flux motors, guiding the magnetic flux lines along an axial path parallel to the motor shaft. The permanent magnets are typically arranged radially on a disc-shaped rotor.

Characterized by a shorter axial length, axial flux motors provide a more direct flux path compared to radial-flux machines. They offer high output power, power density, torque, and energy efficiency, all while remaining relatively lightweight, leading to reduced raw material usage. With a higher active winding copper and less overhang, they can accommodate more turns and generate less heat due to end effects. However, efficient heat dissipation can be challenging due to the compact design, necessitating effective cooling solutions. Axial flux motors represent a modern and innovative approach to electric motor design, featuring a unique configuration that distinguishes them from traditional radial flux motors. Consequently, their construction can be more intricate, demanding meticulous attention to design and manufacturing processes.
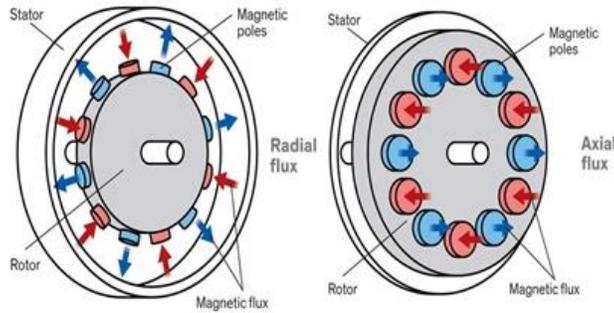
1.5 The Yokeless And Segmented Armature

The Yokeless and Segmented Armature (YASA) topology represents a novel axial flux design that exhibits a significant leap in torque density and efficiency compared to other axial flux motors. This innovative configuration revolves around magnetically separated segments that collectively form the stator of the machine.

➕ Development of YASA topology [12], [13]

The evolution of YASA was initiated through a comprehensive study [12], which scrutinized the performance of two highly efficient axial flux machines: the NS Torus-S and the NN Torus-S topologies.

The NS Torus-S (lap) topology boasts a brief stator yoke, enhancing power density and minimizing losses. However, it necessitates a lap winding for torque generation, resulting in a suboptimal fill factor and prolonged end-windings. This, in turn, enlarges the outer diameter, leading to diminished power density and increased losses.

Conversely, the NN Torus-S topology requires a substantial stator yoke to manage flux from both rotors, elevating losses and decreasing power density. Despite this, a back-to-back winding with a high fill factor can be employed, reducing the protrusion of end windings, and thus increasing power density and efficiency.

26
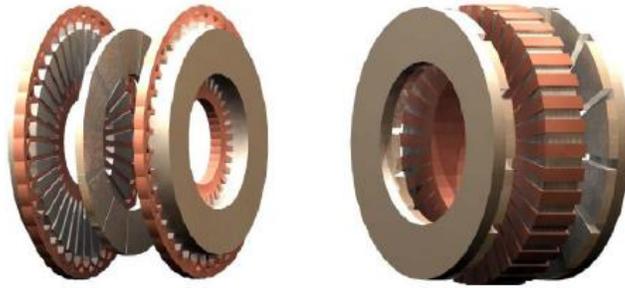
Figure 1.19: NS Torus-S & NN Torus-S topology
[13]

The YASA topology emerges as a breakthrough, combining the favorable attributes of both machines. The YASA topology is crafted by manipulating the NS Torus-S machine [13]:

- The stator yoke, unnecessary for magnetic reasons, is eliminated, rendering the teeth magnetically unconnected.
- The teeth's pitch is expanded, aligning their arcs with those of the magnets.
- Each tooth is individually wound, and teeth and windings are securely bonded with high-strength material.
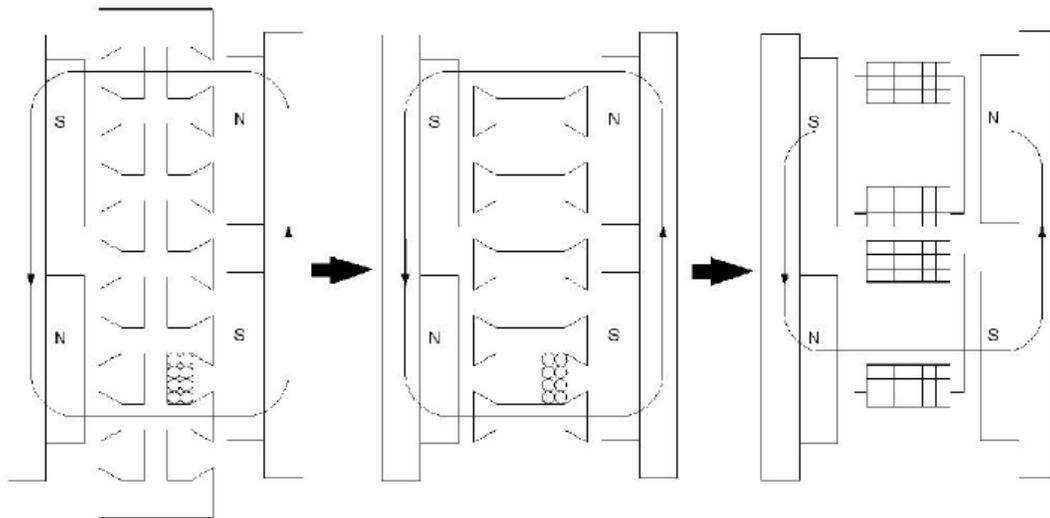
Figure 1.20: NS Torus-S + NN Torus-S -> YASA topology
[13]

Various axial flux permanent magnet (AFPM) topologies exist, with the one-stator-two-rotors and two-stators-one-rotor configurations being particularly appealing. The YASA stands out with two external rotors featuring surface-mounted PMs and an internal stator comprising multiple segments with concentrated winding.

Compared to alternative topologies, the YASA boasts numerous advantages. The concentrated winding with a short overhang results in a high filling factor and reduced copper losses. Moreover, the large air gap area, especially in constrained spaces, contributes to enhanced efficiency. Reduced mutual inductances among machine phases improve phase independence and fault tolerance. Lastly, the iron content in the YASA motor's stator is significantly diminished in comparison to other axial flux motors, usually by approximately 50%, leading to an overall boost in torque density of about 20% [13]. The absence of the stator yoke markedly reduces stator weight and losses, further optimizing efficiency.

Soft Magnetic Composites (SMCs) [14], [15]

In the past decade, there has been substantial progress in the realm of Soft Magnetic Composites (SMCs) and their application in electrical machines. The appeal of these materials lies in their favorable characteristics, including isotropic magnetic and thermal properties, and minimal eddy current loss, particularly at medium and higher frequencies. Employing a cost-effective powder metallurgy process not only reduces post-production steps but also significantly minimizes yield losses in manufacturing, all while boasting lower energy consumption compared to alternative production technologies. SMC materials excel in large-scale mass production, delivering complex components with precise tolerances, and smooth surfaces, eliminating the need for secondary operations, and virtually minimizing material waste. This contrasts with traditional stamped, laminated silicon steels commonly utilized in various electromagnetic devices.

SMC materials are crafted from pure iron powder particles, each meticulously coated with an ultra-thin electrically insulating layer. This creates a magnetically active material that is concurrently electrically resistive, preventing Joule losses. Moreover, SMC components can be efficiently shaped into intricate net forms through the powder metallurgy process. These unique properties

enable space and weight-efficient three-dimensional magnetic circuit designs. SMC components offer advantages in both motor design and production processes, featuring compact size, reduced weight, high specific performance, and excellent cost efficiency due to a streamlined design that requires less material and involves a straightforward net-shaping production process, thereby minimizing waste and subsequent operations. It's noteworthy to highlight their capability in directing three-dimensional magnetic flux, resulting in crucial design advantages attributed to their powdered nature.

SMC finds application in producing rotor yokes and stator segments, comprising numerous surface-insulated iron particles. The pre-alloyed or pure iron powder undergoes uniform mixing with insulation material—organic, inorganic, or a combination thereof—alongside additional additives like binders and lubricants. Following compaction and heat treatment, the result is uniform isotropic components with intricate shapes achieved in a single step. While the mechanical and electromagnetic properties of SMC may be somewhat lower than conventional electrical steel, its unique structure makes it a preferred choice. The stator segments, made from Höganäs SMC material, consist of three distinct parts: two flat side components and a trapezoidal middle part.

⬥ YASA AF PMSM [15]-[17]

Considering all the aspects discussed earlier, the Permanent Magnet Synchronous Motor emerges as a potentially optimal choice for an electric vehicle, combining the benefits of Yokeless and Segmented Armature (YASA) and Axial Flux (AF) pathways. Accordingly, the paper in [15] presents the mechanical design and analysis of a yokeless and segmented armature axial flux permanent-magnet (PM) synchronous machine, featuring two external rotors and an internal stator.
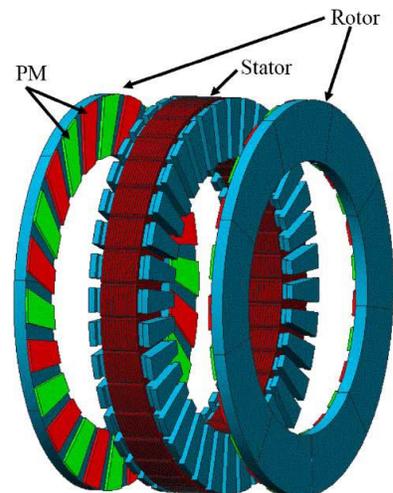

Figure 1.21: YASA AF PMSM with two external rotors [15]

29

o   Stator

The stator comprises three essential subsystems: a component fixing subsystem for the stator segments, an electrical subsystem, and a water-cooling subsystem. PEEK material plates secure the stator segments, selected for their high electrical resistivity, manufacturing feasibility, cost-effectiveness, electromagnetic properties, and the stator's maximum working temperature. Epoxy resin with high thermal conductivity firmly binds the stator components, significantly reducing thermal resistance and enhancing stability. The electrical subsystem connects the current source with the stator, ensuring an even distribution of current from the inverter's three phases within the concentrated windings. The compact and robust design of this subsystem is crucial given the limited space. Additionally, a water-cooling subsystem is integrated into the stator to efficiently dissipate heat, enhancing the electrical load capacity. Placing the water-cooling system close to the stator segments and windings optimizes the rapid export of generated heat.

o   Rotor

To address the significant forces between the stator and rotors resulting from asymmetric air gaps due to manufacturing tolerances and thermal distortion of the shaft, a fixed-floating bearing arrangement is employed. The fixed bearing handles radial and axial forces to secure the shaft in both directions, while the floating bearing provides radial support with axial freedom. Both rotor carriers connect through a shaft sleeve, bound to the shaft through shrinking. An aluminum alloy with robust mechanical properties is utilized to withstand the large centrifugal forces experienced by the rotor yoke, especially at high rotational speeds. Precise alignment of the permanent magnets on both rotors is achieved with annular plates made from PEEK, known for its exceptional magnetic, mechanical, and electrical properties. These plates also play a crucial role in supporting the PM tangentially during high-speed rotation. Using a hollow shaft made of steel reduces weight and deflection caused by asymmetric loads, maintaining accuracy with the bearings' thermal expansion. Technical adhesive firmly bonds the rotor carrier, rotor yokes, and PM. The steel shaft is paired with an aluminum alloy shaft sleeve on both rotors, employing a high-fit excess shrink fit to ensure a secure connection even at elevated temperatures.
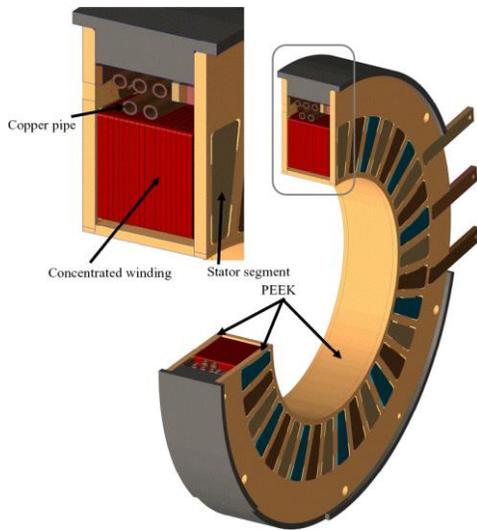
Figure 1.22: Cut view of assembled stator
[15]
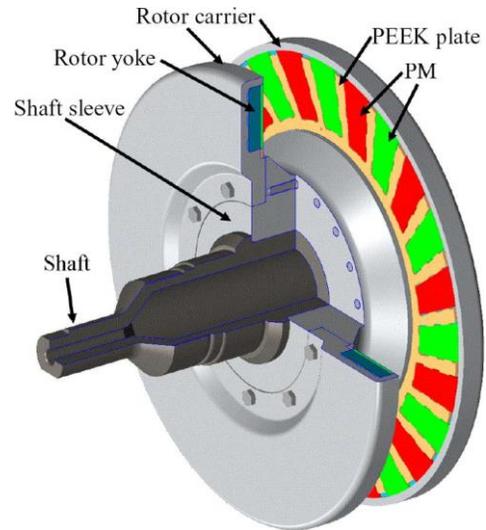
Figure 1.23: Cut view of assembled rotor
[15]

o   Magnetic Flux Pathing

The primary magnetic flux in YASA machines follows an axial flux pathing, illustrated in the figure below [16], [17]. Originating from the N-pole permanent magnet, it traverses the air gap, stator core, and air gap to reach the S-pole on the opposite side. Passing through the rotor core on the second side, the flux starts anew from the N-pole and completes the loop by going through the air gap, stator core, and air gap to reach the S-pole on the first side. Ultimately, the main magnetic flux forms a closed loop.
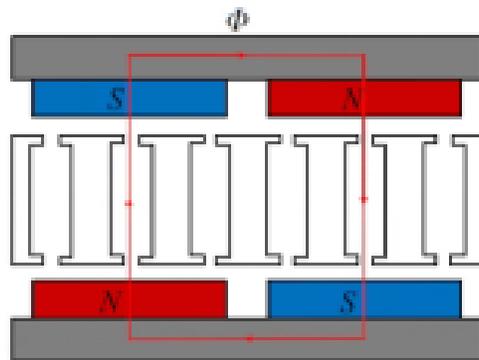
Figure 1.24: Main magnetic flux in YASA
[16]

2) FAULTS

2.1 Fault Generation

Electric machines play a crucial role in modern society, powering essential appliances, transportation, and industries, contributing significantly to convenience, efficiency, and global progress. The extensive use of these machines inevitably leads to potential faults, which can degrade their performance and efficiency. Faults generally arise from three main sources: manufacturing defects, degradation and aging primarily affecting insulation and bearings due to operational factors, and misoperation attributed to human factors.

o   Manufacturing Defects

Manufacturing defects occur because manufacturing operations are not flawless, resulting in inherited asymmetries and stresses in newly produced machines. Typical examples of manufactured asymmetries include porosity, thin film insulation variations, and static eccentricity.

➤   Porosity is inevitably introduced during the die-casting process and can lead to motor performance discrepancies, decreased output power, imbalances in rotor bar current density, and increased rotor bar loss [18], [19].
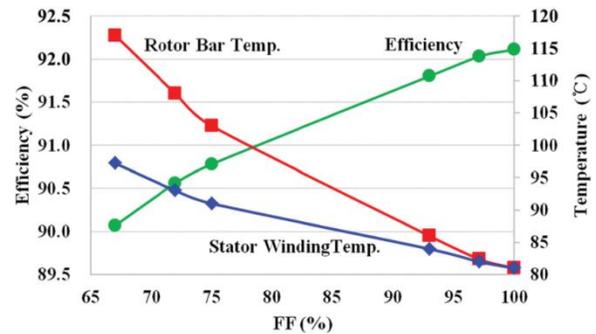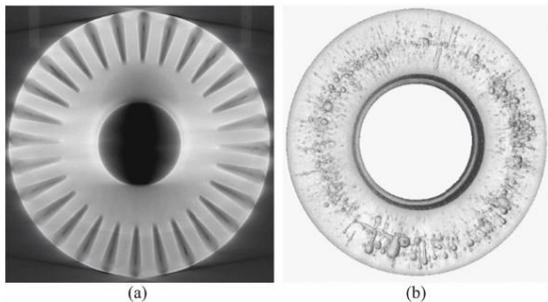
Figure 2.1: X-ray scan of porosity distribution in the rotor bar slot portion (a) and end ring (b)
[18]

Figure 2.2: Rotor bar and stator winding temperature and efficiency as a function of FF
[18]

➢ Based on R and C measurements taken place in [20] on unaged thin film insulation material, it is observed that the measurements present notable variation and asymmetries.
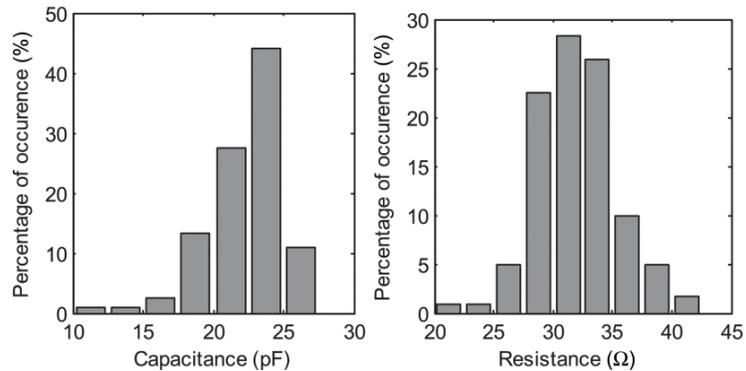
Figure 2.3: Histograms of capacitance and resistance of unaged insulation [20]

➢ Static eccentricity may arise due to manufactured imperfections. More specifically, it can be caused by either the non-perfect circular inner surface of the stator or by the incorrect placement of the rotor inside the stator during the assembly.

Manufactured stresses also play a role, based on [21] for example, where stator manufacturing and assembly processes can potentially degrade insulation integrity. Processes such as stamping, laser cutting, or wire-based electro-discharge machining can damage slot edges or stator teeth, introducing interlaminar faults [22]-[25]. Mechanical stresses occur during the bending/stretching of coils when inserted into slots, and pre-forming processes can introduce additional stresses through pressing, local heating, or mechanical forces to shape coils [25], [26].

o Degradation & Aging

Degradation and aging are inherent challenges faced by electric machines operating in demanding environmental conditions. The combined thermal, electrical, ambient (environmental), and mechanical stresses, collectively known as "TEAM" stress, contribute to the aging profile. These always occur in combination with each other, at different intensities and sometimes affecting each other, which makes the evolution of the aging profile unstable and unpredictable.

Surges and partial discharges are common electrical stresses, while thermal stresses result from load currents causing heat loss and insulation expansion [21]. Mechanical stresses arise from differential expansion between insulation layers and conductors [21] and vibrations due to magnetic forces [27]. Ambient stresses from adverse environmental conditions amplify other stresses, trigger aging, and accelerate the process. There are several examples such as humidity, dust, dirt, debris, moisture, and traces of chemicals, the extents of which depend on the application [21].

o   Human Factor

The human factor also significantly contributes to fault generation in electric machines. Aside from manufacturing defects, humans can impact efficiency through machine selection, mode of operation, and overall functionality. Incorrect choices, regarding the size and characteristics of both the machine and the task, can lead to catastrophic errors. Regular and meticulous maintenance is essential, as machines operate continuously in demanding environments. Accurate diagnosis of faults in the early stages is crucial to prevent catastrophic failures, as cases of undiagnosed faults can lead to severe consequences later on.

2.2 Faults and Consequences

PMSMs are susceptible to significant degradation induced by various factors, including but not limited to humidity, pollution, mechanical vibration, thermal stress, electrical stress, and overload. The demand for higher power/torque density exposes PMSMs to increased mechanical, thermal, and electrical stress, thereby augmenting their vulnerability to faults [28]. In challenging environmental conditions, motor faults become inevitable, posing potential risks such as elevated maintenance or replacement costs, prolonged downtime, and even threats to personal safety [28].

The components most prone to faults in PMSMs encompass the stator winding, rotor cage, winding, magnets, bearings, and airgap eccentricity [29]. The spectrum of faults in PMSM machines spans electromagnetic issues like short circuits and demagnetization, as well as mechanical problems such as rotor eccentricities and bearing damages [30]. These faults are typically categorized into three types: electrical, magnetic, and mechanical [31]. Notably, the

detection of electrical faults in faulty PM becomes more straightforward when compared to identifying magnetic or mechanical faults, owing to easy access to the stator of the motor [32].

Interturn short circuit

The primary cause of motor stator winding failure often stems from the breakdown of turn insulation, a consequence of short circuits within the stator windings. These short circuits can manifest in various types, including inter-turn shorts of the same phase, shorts between coils of the same phase, shorts between two phases, and shorts between a phase and ground [33]. Research in [34], indicates that stator winding faults contribute to nearly 40% of potential motor faults, with the inter-turn short-circuit fault identified as the primary culprit. The susceptibility of winding insulation to faults is noteworthy, as short circuits in the stator winding can occur between turns of the same phase (turn-to-turn or inter-turns), between turns of different phases (phase-to-phase), and between turns and the stator core (phase-to-ground) [29].

The Inter-turn short-circuit fault arises from insulation degradation, which may be induced by factors such as thermal stress, mechanical stress, power surges, and foreign objects [28], [35]. Following the emergence of incipient faults, an inconspicuous electrical contact between two turns forms, creating a loop coupled to the original winding. In this loop, back-EMF and inductor coupling serve as voltage sources, while the impedance of shorted turns and the resistance in the short path act as current limiters [28], [30], [35]. Typically, the impedance of the shorted turn is very low, allowing the circulating current to be several times higher than the rated current. This substantial induced current significantly increases the temperature in the affected area, leading to local overheating [28], [30]. The impact of the inter-turn short-circuit fault progressively expands, causing harm to the motor, particularly to Permanent Magnet Synchronous Motors (PMSMs). The large circulating current weakens the magnetic coercivity, producing magnetic field intensities that result in the permanent demagnetization of the rotor magnets, limiting the functionality of the traction machine, especially under high loads or transient conditions [28], [31], [36]. If not addressed promptly in the early stages, the fault can give rise to secondary faults, such as phase-to-phase and phase-to-ground faults. Hence, early detection of the stator inter-turn short fault is crucial [34].

Based on [26], [35], [37], [38], the analysis of the inter-turn short-circuit fault involves modeling. Without loss of generality, the fault is assumed to be in phase a, and the equivalent circuit considers the resistance, self-inductance, mutual inductance, and back-EMF of PMSM stator windings. The inter-turn short-circuit fault is modeled by adding a circuit to the insulation fault part of phase a, utilizing the short-circuit contact resistance (R_f) to simulate the degree of degraded insulation. The current in the circulating path is divided into two components: the short-circuit current (i_f) flowing in the short path and the fault current (i_s) in the shorted turns.
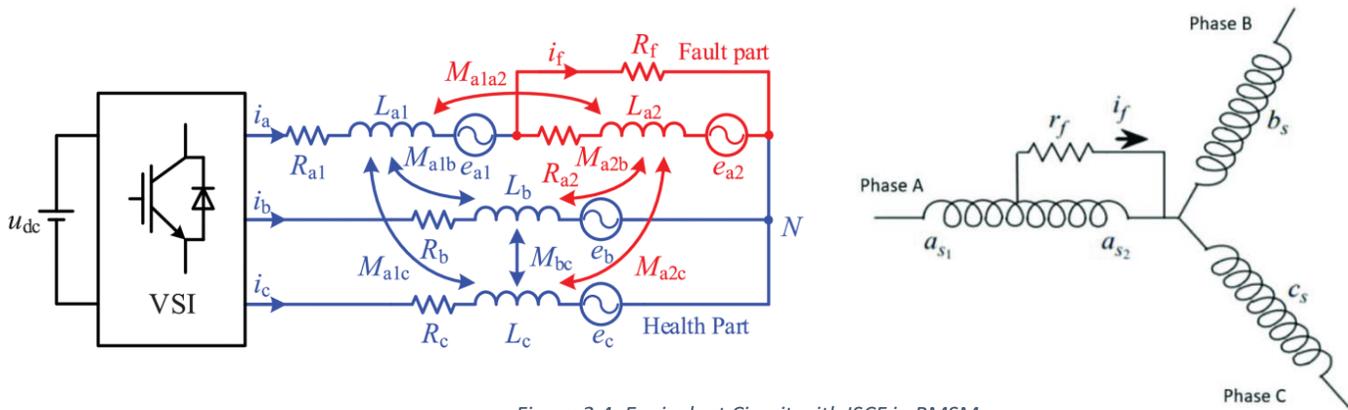
Figure 2.4: Equivalent Circuit with ISCF in PMSM
[28], [37]

In the early stages, shorted turns in stator windings may not disrupt normal operation. However, they can escalate into severe motor failure over time. Depending on the type of shorts and the motor's condition (age, working condition, etc.), the motor may initially continue to operate despite the flow of short-circuit current, leading to increased overheating and potential complete failure if left unaddressed [33]. While the motor might persist in running with inter-turn and coil shorts of the same phase, shorts between phases and phase-to-earth are detrimental, resulting in instantaneous motor shutdown and rendering the machine unusable [39]. Regarding the failure mode trend, it is generally asserted that undetected shorts in a specific phase could evolve into phase-to-phase faults. Although exclusive data on the transition time between inter-turn and groundwall insulation failure are lacking, the detection of inter-turn shorts during motor operation can mitigate damage to adjacent coils and the stator core, reducing repair costs and motor downtime [33].

Figure 2.5: Catastrophic electrical failures
https://www.ti.com/document-viewer/lit/html/SSZT

✚ Eccentricity

Mechanical faults encompass issues related to bearings and eccentricity. Recently, rotor eccentricity and bearing failures have been identified as major contributors to problems in Permanent Magnet Synchronous Motors (PMSMs). These faults may arise from manufacturing defects, operating stresses, and misoperation, leading to the irreversible degradation of motor performance and efficiency. Therefore, regular monitoring of the rotor condition is imperative for ensuring optimal motor performance and the overall efficiency of the associated processes [40]. Remarkably, 80% of mechanical faults lead to eccentricity issues [31].

In healthy synchronous machines, the air gap length remains constant, but eccentricity disrupts this uniformity, making the air gap non-uniform [31]. The fault of stator and rotor eccentricity primarily stems from mechanical causes, specifically due to manufacturing imprecisions such as unbalanced mass, shaft bow, bearing tolerance, or factors introduced during motor operation. This fault results in the displacement of the symmetrical axes of the stator, rotor, and rotor rotation axis. Such displacement is classified into static, dynamic, and mixed eccentricity [40].

In static eccentricity (SE), the rotor rotation axes coincide with its symmetrical axes but are displaced concerning the stator symmetrical axes. In such instances, the air gap distribution around the rotor lacks uniformity but remains time-independent, with its level unchanged over time [32], [40]. Static eccentricity typically arises from the misplacement of the rotor on the bearings.

Dynamic eccentricity (DE) occurs when the rotor rotation axes differ from its symmetrical axes. Unlike static eccentricity, the asymmetry of the air gap changes over time, making it time-dependent. This form of eccentricity can be caused by worn bearings, a bent shaft, asymmetric thermal expansion of the rotor, or a high level of static eccentricity [40].

Mixed eccentricity combines the characteristics of both static and dynamic eccentricity, with all three axes—symmetrical axis of the stator, symmetrical axis of the rotor, and rotation axis of the rotor—displaced from each other. Similar to dynamic eccentricity, the air gap's asymmetry is time-dependent and can occur due to the causes mentioned above.
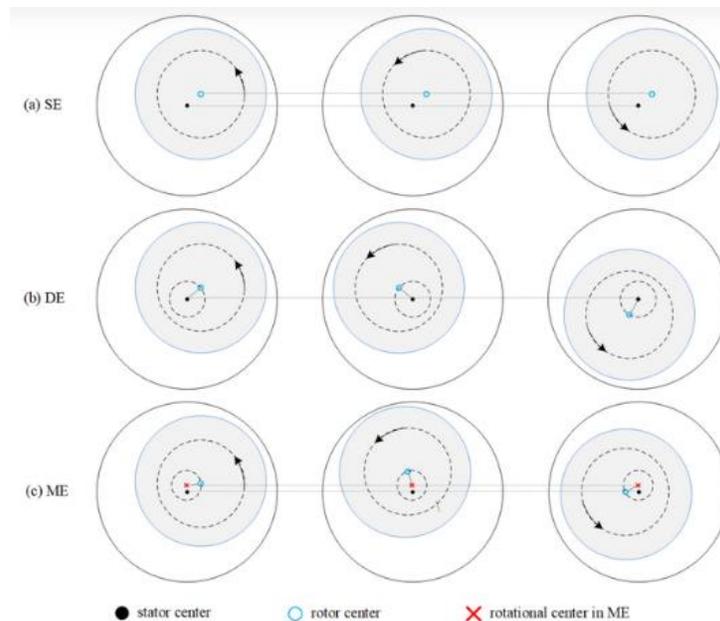

Figure 2.6: Types of eccentricity
https://encyclopedia.pub/entry/12700

In Permanent Magnet Synchronous Motors (PMSMs), the occurrence of eccentricity results in a portion of the stator being closer to the rotor's permanent magnets. Consequently, airgap eccentricity induces a force on the rotor, known as Unbalanced Magnetic Pull (UMP), which endeavors to draw the rotor toward the stator bore, aligning with the direction of the minimum airgap [29]. The distortion of back EMF and phase current amplifies torque ripples and, in the most adverse scenarios, escalates both the unbalanced force and cogging torque of the PMSM [32]. Furthermore, eccentricity can give rise to magnetic and dynamic issues, introducing additional vibrations, acoustic noises, torque pulsations, bearing wear, and rotor deflection [32], [40]. Failure to maintain eccentricity within specified limits (typically 5%–10%) [40] can subject the motor to undue stress. Severe airgap eccentricity has the potential to culminate in rotor-to-stator rubbing, causing consequential damage to the stator, rotor core, and winding [29].
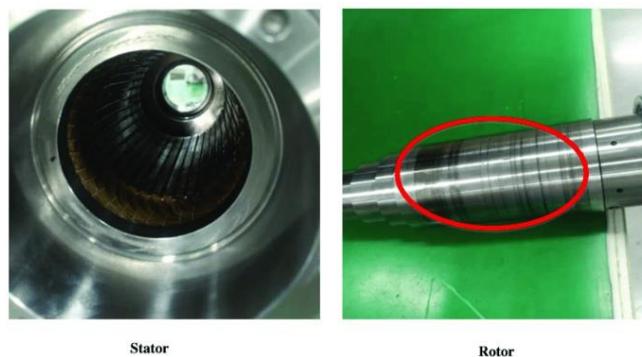

Figure 2.7: Rotor-stator rub caused by eccentricity fault
https://www.researchgate.net/figure/Rotor-stator-rub-of-an-induction-motor-caused-by-eccentricity-fault_fig1_327793894

🔸 Demagnetization

Demagnetization faults pose a significant challenge in permanent magnet synchronous motors, exerting a substantial impact on motor performance [39]. Regular monitoring of the magnet quality becomes crucial not only to ensure optimal motor functionality but also for the reliability and efficiency of the entire operational process [41]. Demagnetization can manifest in either complete/uniform or partial/local demagnetization, where accordingly, the entire magnet uniformly loses its magnetization, or it occurs only in a specific region of the pole [30].

The intricacies of partial or uniform demagnetization are attributed to a confluence of thermal, electrical, mechanical, and environmental stresses on the permanent magnet (PM) [40], resulting in irreversible degradation of motor performance and efficiency [41]. In the context of [41], PM demagnetization is elucidated and examined as follows:

Sustained exposure to elevated temperatures can lead to permanent demagnetization, causing alterations in the metallurgical structure and impairing the magnet's remagnetization capability. It is imperative to maintain the motor's operating temperature below the maximum service temperature to prevent demagnetization.

The magnet's operation occurs at the intersection between the demagnetization curve of the PM (second quadrant of the B−H curve) and the load line, influenced by the magnetic circuit and armature current. While the motor typically operates at point a' under normal load conditions, large armature currents generating demagnetizing MMF can drive the operating point below the knee of the curve to a'', following the relative recoil permeability line (a''−b'−b−B'_r). Recovery to b' under normal load conditions results in irreversible demagnetization [42], [43]. Studies [43]-[45] indicate that faults in the inverter or motor, such as open or short circuit switches/phases or stator winding insulation failure, can significantly increase demagnetizing MMF, leading to irreversible PM demagnetization. Hence, limiting the armature current is essential, in addition to controlling temperature, to prevent irreversible demagnetization.

Under normal conditions, the operating point can also deviate from the knee of the curve due to changes in operating temperature, resulting in irreversible demagnetization. Remanent flux density B_r generally decreases with temperature increase, and coercivity H_c decreases with elevated temperatures for SmCo and NdFeB magnets. In this scenario, the operating point falls off the knee of the curve to point c' under normal load conditions at elevated temperature T_2. The operating point is then formed on the recoil line connecting c' and B''_r, not on the B−H curve. If the temperature decreases to T_1, the operating point is formed on the a''−B'_r recoil line, leading to irreversible demagnetization [42].
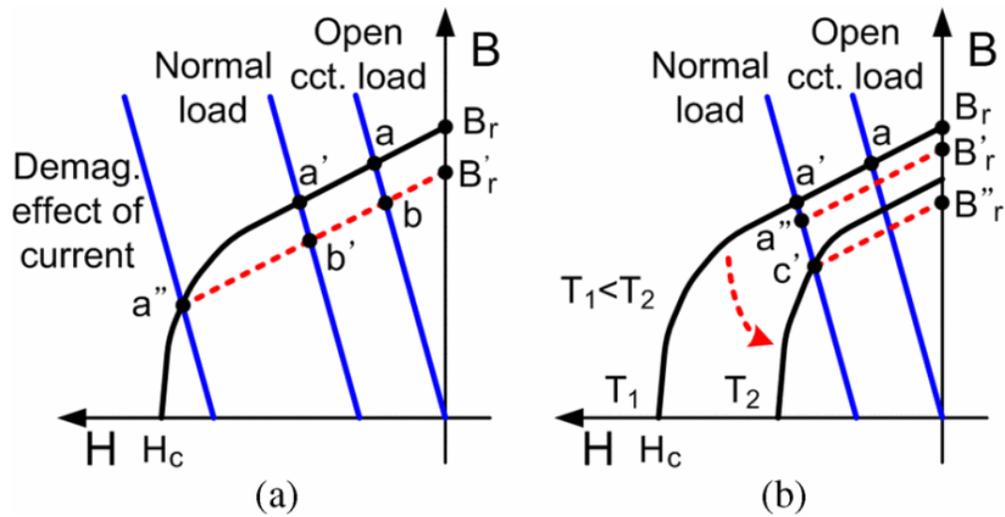
Figure 2.8: PM operation point (demagnetization and load line)
[41]

Rare-earth magnet materials are susceptible to metallurgical structural changes resulting from corrosion or oxidation, leading to demagnetization [42], [46]-[48]. The oxidized segment of the magnet undergoes structural changes over time, especially in elevated temperatures and/or humid or chloride-containing environments [46]. This altered portion, characterized by reduced flux density and coercivity, is more brittle and may, in extreme cases, experience total disintegration. Other potential demagnetization causes include a gradual decline in magnet strength (domain relaxation [33]) and damage, such as chipping or cracking, induced by vibration, shock, or mechanical forces during operation.

NdFeB magnets have gained popularity in electric machines due to their high energy product (elevated B_r and H_c) and relatively lower cost compared to SmCo magnets. However, they are prone to both reversible and irreversible demagnetization owing to unfavorable thermal characteristics (high negative temperature coefficient and low maximum service temperature). Additionally, their corrosion resistance is diminished in humid and chloride-containing environments, and the material exhibits subpar mechanical strength [47], [48]. Consequently, protective measures, such as coating or incorporating various composite materials, are employed with NdFeB magnets to enhance corrosion resistance.

The impact of a demagnetization fault on the machine is profound, significantly diminishing the electromotive force (EMF) of the PM machine and inducing disturbances in air-gap flux [29], [30]. Mechanically, it results in an unbalanced magnetic pull, giving rise to magnetic force harmonics that trigger acoustic noise and vibrations within the machine [30]. The demagnetization of rotor permanent magnets can substantially decrease the output torque of a PMSM, necessitating a higher current in the stator winding to generate the same output torque. Consequently, demagnetization leads to an escalation of copper losses and temperature [29], [39]. Additionally, defects in permanent magnets can cause air-gap flux disturbances.
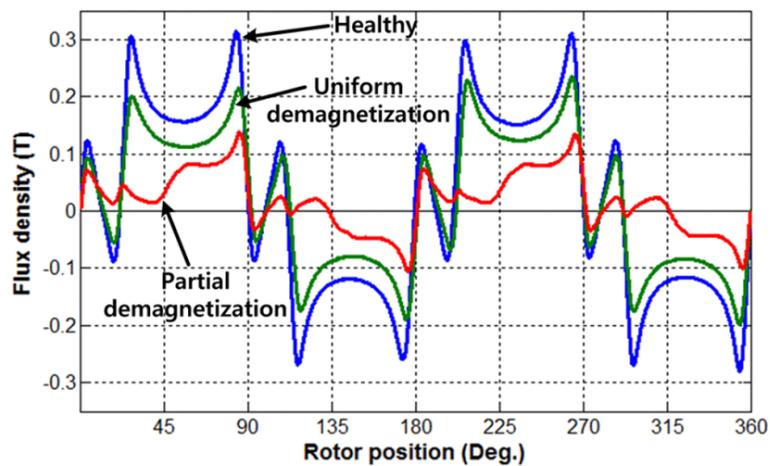

Figure 2.9: Flux density measurements
[40]

Despite implementing preventive measures in the design, fabrication, and operation of PM machines to avert local or uniform PM demagnetization, occurrences can arise due to a combination of the aforementioned operational stresses [43], [49]. Hence, regular monitoring of magnet quality is imperative to ensure the optimal performance, efficiency, and reliability of PM motor drive systems.

2.3 Diagnostic Methods

Continuous monitoring of electrical equipment has become imperative in modern industries to enhance reliability and safety. Over time, various condition-monitoring techniques have been developed to assess the health of electrical equipment like motors, generators, transformers, and compressors. The integration of computerized measurement and data processing systems has significantly simplified and improved the effectiveness of condition monitoring [50].

In the realm of motor health assessment, the fundamental objective of fault diagnosis is early identification, ensuring detection while the fault is still in its incipient stage. This means identifying issues before they become severe while the machine is operating within normal parameters. The overarching goal is to avert catastrophic failures that could potentially lead to the shutdown of the entire machine. As a result, issues such as open circuits or short circuits between phases, or between phases and ground, are not within the scope of diagnostics, as they cause immediate failure and necessitate different strategies, typically involving relays.

Regardless of the specific diagnostic method employed, they all share a common starting point. The acknowledgment is that emerging faults induce asymmetries or distortions in the magnetic field, and consequently, this asymmetry extends to electrical, magnetic, and mechanical waveforms. The impact of the fault is then revealed through appropriate method analysis, utilizing harmonic signatures. The subsequent section provides a concise analysis of the primary diagnostic methods in use.

o   Stator Current Monitoring

Stator Current Monitoring, commonly known as Motor Current Signature Analysis (MCSA), relies on observing the stator current and conducting spectral analysis through Fast Fourier Transform (FFT) [50]. Distinct frequency components in the motor current waveform are generated by various motor faults. Through the analysis of these unique frequency components in the motor current spectrum, MCSA can precisely identify specific fault types and assess their severity. The underlying concept is that if these components exhibit a high amplitude in the FFT spectrum, the fault's severity is elevated, whereas minimal amplitude suggests the fault's absence or its presence in an early stage [51].

While current monitoring has proven valuable for diagnosing various failure types, it has demonstrated exceptional reliability in detecting rotor damages and eccentricities [51]. MCSA is a non-intrusive testing method, eliminating the need for physical contact with the motor or additional sensors. This characteristic makes it a safe and convenient option for remotely monitoring motors during regular operation without causing downtime. Moreover, MCSA boasts reduced implementation costs, utilizing simple measurement equipment, and often leveraging pre-existing sensors [51]. It provides continuous, online monitoring capability and comprehensive coverage for diagnosing various faults.

Figure 2.10: Remote monitoring of current
[51]

o   Magnetic Flux Monitoring

Magnetic Flux Monitoring has emerged as a highly promising technique for condition monitoring of electrical machines, gaining substantial momentum in the last decade. Key to its advancements is the improvement in sensor technologies, facilitating precise measurements of both air gap magnetic flux and stray magnetic flux around motors [52].

The magnetic flux within electrical machines manifests internally in the airgap and externally as stray magnetic flux around the machine's periphery [52]. Internal flux measurement involves invasive techniques, necessitating sensor placement inside the machine. In contrast, measuring external stray magnetic flux involves placing sensors near the housing. For stray flux, sensors can be strategically installed to capture radial or axial flux portions or a combination of both.

Noteworthy advantages of magnetic flux-based condition monitoring include the availability of low-cost and straightforward measurement systems, with the added benefit that the magnetic field serves as a direct indicator of the machine's health [52]. According to [52]-[56], a comparison between stray and air-gap flux can be drawn. Stray flux monitoring, a method gaining popularity, can be applied online, is non-intrusive, and is cost-effective. It possesses the capability to discriminate various conditions, albeit being less sensitive to mechanical failures. Conversely, air-gap flux monitoring exhibits high fault sensitivity and diagnostic reliability but is considered intrusive [52].
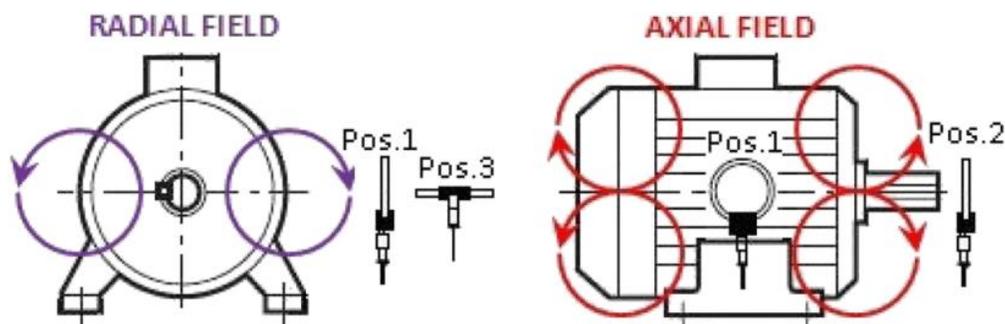

Figure 2.11: Coil Sensor in different measurement positions
[55]

o   Vibrations – Acoustic Noise Analysis

The operation of a machine or moving vehicle is invariably accompanied by vibrations, imposing dynamic loads on the structure. These loads directly impact structural fatigue, thereby influencing material integrity. The vibration signature changes concomitant with structural alterations. Consequently, vibration serves as a significant health indicator or diagnostic parameter in machinery, primarily employed for the detection of mechanical faults [59].

Within electric machines, vibrations manifest as a composite of three distinct components: aerodynamic, mechanical, and electromagnetic, constituting the primary sources of acoustic noise in electrical motors [57], [61]. Aerodynamic vibration arises from pressure fluctuations in the air gap, while mechanical vibration is a byproduct of the rotational movement of machine components such as the rotor, bearings, and shaft. The vibroacoustic behavior of an electrical machine directly reflects the structural excitation induced by the electromagnetic force during operation [50]. Even a minute harmonic of magnetic force can trigger substantial acoustic noise and vibrations owing to machine resonance.

In Permanent Magnet Synchronous Motors (PMSM), noise and vibration predominantly stem from electromagnetic forces, encompassing tangential components like cogging torque and torque ripple, along with radial components [58]. However, a notable challenge arises in the installation of vibration sensors on the machine, as external sensors are typically required. This poses a complication as machines are rarely designed by manufacturers with this purpose in mind [60].

o   Torque – Speed Monitoring

Torque and speed monitoring, as outlined in references [62]-[64], typically involves the direct measurement of mechanical torque and speed using specialized sensors. However, the installation of these sensors is often deemed impractical and costly. Consequently, electromagnetic torque and speed are commonly estimated by leveraging voltage and current measurements. Subsequently, through spectrum analysis utilizing the fast Fourier transform (FFT), higher harmonic components associated with occurring faults can be discerned.

o   Instantaneous Power Monitoring

Instantaneous Power Monitoring, as facilitated by Instantaneous Power Spectra Analysis (IPSA), offers both fault detection and an estimation of probable damage levels by scrutinizing appropriate harmonic values. Specifically, the analysis of the power signal spectrum, unlike the spectra of stator phase currents, not only reveals the presence of corresponding damage or defects but also enables an estimation of the damage level based on the power value of the corresponding harmonic component [66], [67].

For the analysis of instantaneous power, all phase currents and voltage signals are required, and it can be represented by the following expression [65]:

➤ $p(t) = u(t) \cdot i(t)$

Theoretical analysis indicates that, in comparison to common methods for current or voltage spectrum analysis, the instantaneous power spectrum holds the advantage of not requiring external sensors or additional hardware devices [68].

o   Temperature Monitoring

Temperature monitoring relies on infrared thermography, an increasingly utilized technology in recent years for assessing conditions in electric machines. This method stands out as noninvasive and nondestructive, offering the advantage of detecting the thermal conditions of equipment without causing harm [69].

Infrared thermography operates on the physical principle that objects with temperatures above 0 K (-273 °C) emit electromagnetic radiation in the infrared region of the electromagnetic spectrum. Sensors designed to respond to this radiation generate thermal images, where pixel colors correspond to a temperature-based scale. Typically, these thermal images, or thermograms, are presented in a red, green, and blue (RGB) scale [70].

Given that most motor faults result in temperature increases, either overall or in specific regions, infrared data analysis proves valuable for fault detection [71], [72]. Thermography, being non-destructive and non-intrusive, does not necessitate physical contact with the object [70], [73].

Moreover, the relevance of infrared thermography in monitoring processes has surged due to advancements in infrared cameras, characterized by enhanced resolution, reduced dimensions, reliability, functionality, and lower costs [74]. Nevertheless, visually distinguishing fault types in thermal images can be challenging due to subtle differences. Therefore, the application of advanced image processing methods and machine learning algorithms becomes essential for extracting fault features and detecting patterns and anomalies from thermal images [71], [73].

Initially employed as secondary elements in machine condition monitoring, infrared sensors now, thanks to modern data processing techniques, can provide a preliminary or even direct diagnosis in a nonintrusive manner in various industrial applications [74].


Figure 2.12: Infrared inspection of motor with deficient cooling before and after cleaning [72]
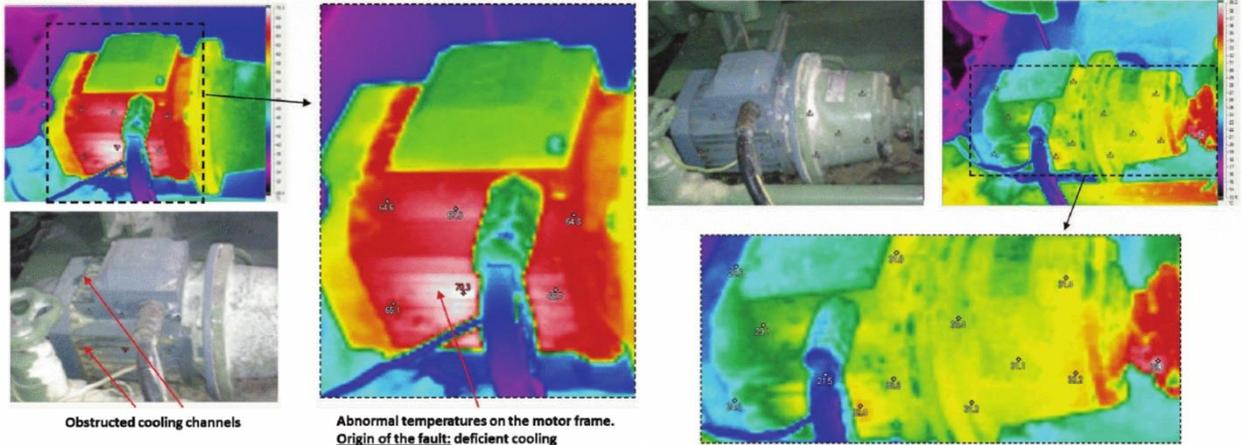
3) INSULATION MONITORING AND THERMAL AGING

3.1 Insulation System

One of the paramount technologies crucial for the optimal performance of electrical machines is arguably the electrical insulation system, recognized as the most vital factor in constraining performance [21]. Despite being a passive component in an electrical machine that doesn't generate torque, the insulation system plays a pivotal role in influencing machine cooling, consequently impacting electrical loading and torque production [26]. Its significance is underscored by the potential repercussions of insulation breakdown, leading to failures, unforeseen downtime, negative financial implications, and, in certain applications, a safety hazard [26]. The insulation systems in electrical machines serve two primary functions: facilitating the dissipation of heat from conductors to prevent short circuits between winding turns and between winding turns and the ground (iron core) and offering mechanical support and restraint by preventing winding movement in both the rotor and stator [21], [26]. The insulation systems for various types of electrical machines can be categorized into two main types: stator winding insulation and rotor winding insulation [26].

- Rotor Windings [25], [75]

The rotor windings in synchronous machines encompass both turn and ground insulation. Turn insulation is typically crafted from slender strips of aramid "paper," while ground insulation commonly comprises strips of epoxy-glass laminates or aramid paper. Rotor winding encounters formidable stresses, primarily stemming from temperature fluctuations and mechanical forces induced by rotation and thermal expansion. Electrical stress is generally modest, usually below 500 V DC.

The failure of turn insulation, even across multiple locations, doesn't necessarily prompt the shutdown of a generator or synchronous motor. Instead, it manifests in heightened rotor vibration, attributed to asymmetrical magnetic fields and uneven rotor heating/expansion.
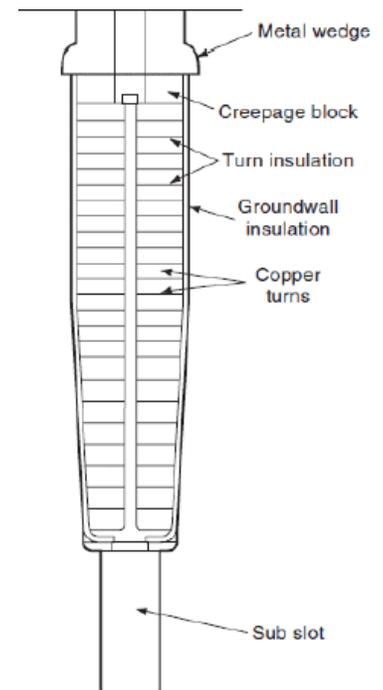

Figure 3.1: Rotor winding [75]

As long as the vibration remains within acceptable limits, the machine can persist in operation. However, a proliferation of turn faults may eventually lead to a ground fault or trigger a "high bearing vibration" trip. In the case of a ground insulation fault in a synchronous machine's rotor winding, the usual course of action involves shutting down the machine. Ground faults may result from the direct deterioration of ground insulation or the cumulative impact of an increasing number of turn faults.

⬇ Stator Winding [36]

The essential components of a traction machine's stator include a magnetic stator core, electric conductors (typically made of copper), and an insulation system. The primary function of the core is to establish a low reluctance path for the magnetic field, and it is commonly composed of thin sheets of magnetic steel. Electric conductors are responsible for carrying the currents supplied to the machine, and their dimensions must be carefully determined to ensure operational integrity without overheating. Stator windings fall into two general categories: random-wound and form-wound windings.

○   Random-wound Windings [21], [25], [26]

In random-wound windings, circular insulated copper conductors (commonly known as magnet wire or enamel wire) are wrapped around the stator teeth in a random arrangement. Typically, these windings find application in systems with a power level in the range of several hundred kilowatts and a voltage level below 1000V. Random-wound windings consist of enamel wire, separator, slot liner, and slot wedge, among other components. The use of random-wound windings introduces the possibility of a high-voltage turn (connected to the input terminal) being close to a lower-voltage turn (near the low-voltage neutral point). Consequently, there exists a significant voltage difference between the first and last turns in random-wound stators, necessitating thicker insulation. Despite this challenge, random-wound windings are preferred for their simplicity, cost-effectiveness, and shorter manufacturing time.

o   Form-wound Windings [21], [25], [26]

Form-wound coils are crafted from rectangular section copper bars, with the copper conductors pre-shaped into the desired geometry and pre-insulated with secondary insulation before being positioned in the stator slots. The meticulous placement of individual turns in form-wound coils is enhanced by the pre-shaping process, enabling a consistent arrangement of conductors. This results in the development of minimal turn-to-turn voltage, allowing for the use of exceptionally thin layers of turn insulation. This particular winding technique is commonly applied in high-performance scenarios where efficiency, reliability, and precision play pivotal roles. The precision afforded by form-wound coils proves crucial in ensuring optimal performance in such applications.
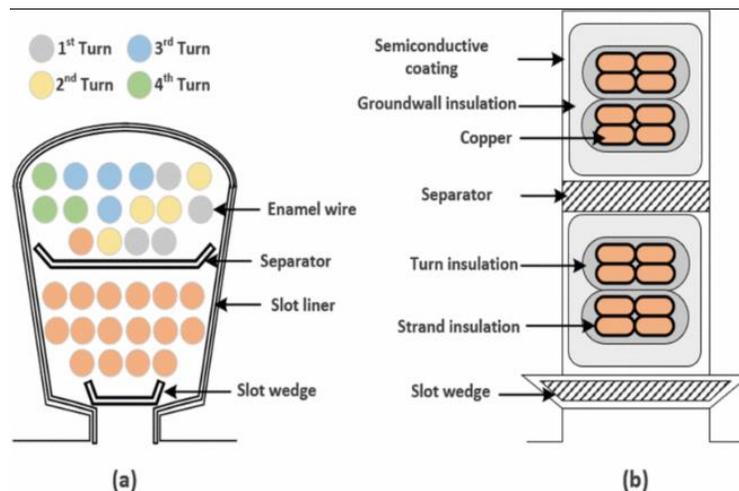

Figure 3.2: Cross section of stator slot: (a) Random-wound winding, (b) Form-wound winding [26]

The stator insulation system is bifurcated into primary and secondary insulation [36]. Within the realm of stator primary insulation, three key categories exist: insulation, which entails insulated magnet wire for each conductor (strand insulation); coil separator for multi-layer windings (turn insulation); and slot cell insulation (groundwall insulation). Secondary insulation is occasionally employed to bolster the electrical insulating capabilities of the winding, safeguarding it against environmental factors like dirt and moisture, while also imparting additional mechanical strength. A prevalent method for incorporating secondary insulation involves impregnating the stator.

- <u>Strand Insulation</u> [21], [25], [76], [77]

The individual copper conductors are enveloped in a layer of insulation known as strand insulation, which serves to manage voltages between adjacent strands. The presence of strands is driven by several factors. From a mechanical standpoint, a conductor must possess a large cross-sectional area to efficiently carry the required current. However, such a conductor is challenging to bend for the creation of windings. To overcome this, the conductor is divided into smaller strands, allowing for easier shaping. Electrically, the use of multiple strands helps mitigate the skin effect, as the resistance of the conductor is not significantly influenced by AC, leading to reduced electrical losses. Additionally, this configuration contributes to the reduction of losses from harmonics and eddy currents. Strand insulation is typically crafted from materials such as enamel, polyester, polyimide, or glass fabric tape, either individually or in combination.

- <u>Turn Insulation</u> [21], [25], [75], [76]

In the context of multiturn windings, the turns are enveloped in turn insulation. This insulation serves to safeguard the winding from potential short circuits between turns, facing various voltage stresses, including phase-to-ground, turn-to-turn, coil-to-coil, and transient voltage surges. Essential for the protection of the winding, the turn insulation must exhibit sufficient thermal properties to withstand elevated temperatures resulting from losses. Its significance is underscored by its pivotal role in preventing the occurrence of inter-turn short circuit faults, a fault recognized in the literature for its rapid evolution and escalating severity, posing hazards to machine operation and carrying the potential for a ground-wall fault. In the case of random-wound coils, the strand and turn insulation are identical. Turn insulation commonly employs materials such as Kapton, polyimide, mica, epoxies, and various combinations in film form.

+ <u>Groundwall Insulation</u> [21], [25], [75], [76], [79]

Groundwall insulation serves as the primary high-voltage electrical insulation that separates copper conductors from the grounded stator core in stator windings. This insulation component holds critical significance, acting as a protective barrier for the stator core surface, slots, teeth, and end-winding. The groundwall insulation also bears the entire phase voltage, especially stressing coils connected to terminals. Consequently, it necessitates robust electrical, thermal, and mechanical properties. The proper fastening of the winding in the slot, ensuring mechanical support, is achieved through the use of packing materials and slot wedges. An additional crucial need for groundwall insulation is the avoidance of air voids. The presence of air voids may heighten insulation thermal resistance, allow conductor vibrations, and potentially lead to partial discharges.

The groundwall insulation consists of three basic components. A barrier against PD and tree growth, made of mica flakes, a support material for mechanical strength, made of glass fiber, polyethylene terephthalate (PETP) film, or polyester fleece, and a binder material filling the air gaps between the different layers of barrier and support material, made of polyester or epoxy resin. The mica flakes are bound together by a binder material (polyester or epoxy resin), forming what is known as mica paper. However, mica paper has low mechanical strength, necessitating the inclusion of support material, such as glass fiber, resulting in the creation of mica tapes. When these tapes are wrapped around copper conductors, air voids may form between different tape layers. To address this, thermoset binder materials like epoxy and polyester are used to fill the air voids. The binder material not only enhances mechanical strength but also improves the electrical, thermal, and environmental resistance of mica paper. The resin needs to be robust and elastic enough to endure repeated stress from thermal expansions and contractions.

Partial Discharges [21], [25], [26], [36], [77], [78]

Partial discharge (PD) is the localized breakdown of dielectric voids within the insulation system when subjected to high voltage stress. Typically occurring within void spaces or cavities among insulating materials, such as pores and delamination, PD can also manifest at sharp edges like stator tooth tips and surfaces like the groundwall and inner slot surface, particularly in areas with defects such as cracking.

Partial discharges transpire in electrical insulation systems when the electric field strength surpasses the air's breakdown value, generating current through the process of ionization. Ionization involves the separation of electrons from the atoms of the insulation material, resulting in the formation of ions and electrons. The negative electrons traverse the air towards the more positive conductor, colliding with other ionizing atoms in the process.

As previously mentioned, electric discharge is influenced not only by voltage but also by the electric field. At room temperature and 100 kPa, PD occurs if the electric stress surpasses the electrical breakdown strength of air, defined by $E = V/d > 3$ kV/mm. Here, E represents the electric field strength, V is the potential difference (voltage) across an air-filled void due to a capacitive voltage divider, and d is the separation distance.
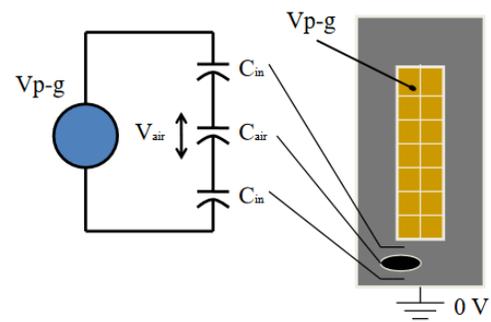

Figure 3.3: Electrical representation of PD [25]

Considering that solid insulation material typically has an electric strength 100 times higher than air, around 200 kV/mm, it is inferred that partial discharges only occur due to air voids. This discharge, involving the flow of electrons, can lead to progressive local degradation of the insulating material. Consequently, PD is recognized as the primary electrical factor initiating aging, which may ultimately result in the failure of ostensibly solid insulation regions.

- <u>Stress relief coatings</u> [21], [25], [76]

A semiconducting coating, typically composed of materials such as silicon carbide mixtures or robust silicon resins with strong mechanical and thermal properties, is applied to the groundwall insulation. This coating plays a crucial role in transferring the earth potential of the iron core to the stator winding, effectively preventing surface discharges on the stator winding. To ensure optimal electrical contact between the groundwall insulation and the iron core, a filler material—often semiconductive—is inserted between them. This filler material not only facilitates electrical contact but also serves the dual purpose of securely restraining the stator winding from any movements within the slot. These measures collectively form a robust defense against mechanical strains and thermal stresses, providing an effective means to suppress partial discharge (PD) activity.

- <u>Impregnation</u> [21], [25], [76], [80], [83]

Impregnation serves the purpose of eliminating air voids within winding conductors and between the winding and the core, aiming to enhance dielectric strength, mechanical robustness, and heat transfer. Two primary manufacturing processes are commonly employed for stator windings: Vacuum pressure impregnation (VPI) and Resin-rich processes. In the VPI method, mica tapes, often referred to as "dry bands," with a resin content ranging from 5% to 15%, are wrapped around copper conductors. Subsequently, vacuum impregnation is carried out using resin supplied from an external storage tank. It can be implemented on individual stator windings or the entire stator. Resin-rich processes utilize mica tapes known as "wet bands," containing a higher resin content of 40%–45%. Under pressure and temperatures ranging from 120 °C to 180 °C, the resin in these tapes melts. The pre-existing resin in the mica tape is utilized to fill voids in the insulation. As suggested by [83], the optimal final resin content for groundwall insulation is 25%–30% for both VPI and resin-rich processes.
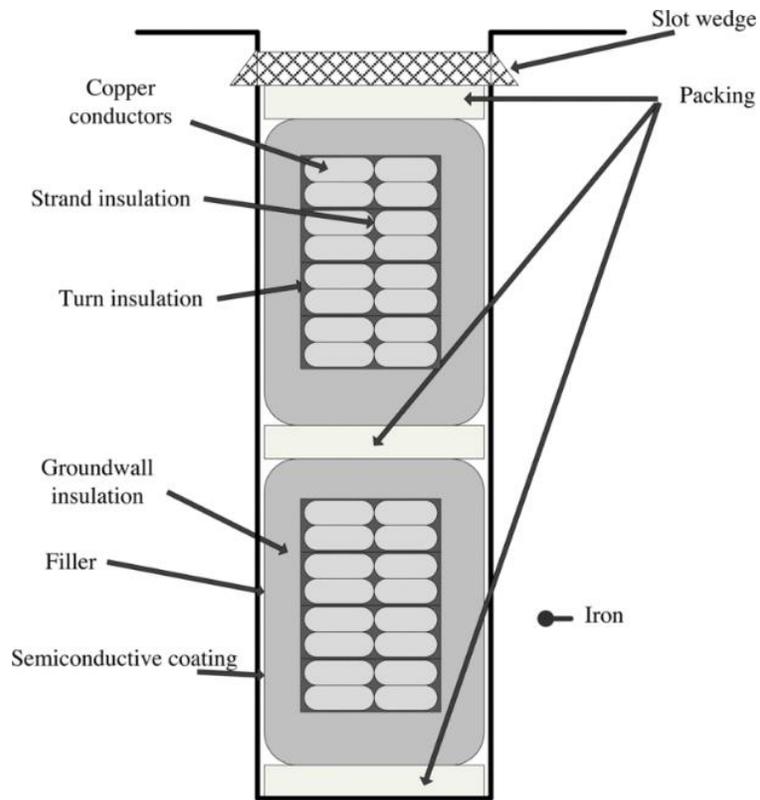
Figure 3.4: Stator Winding
[76]
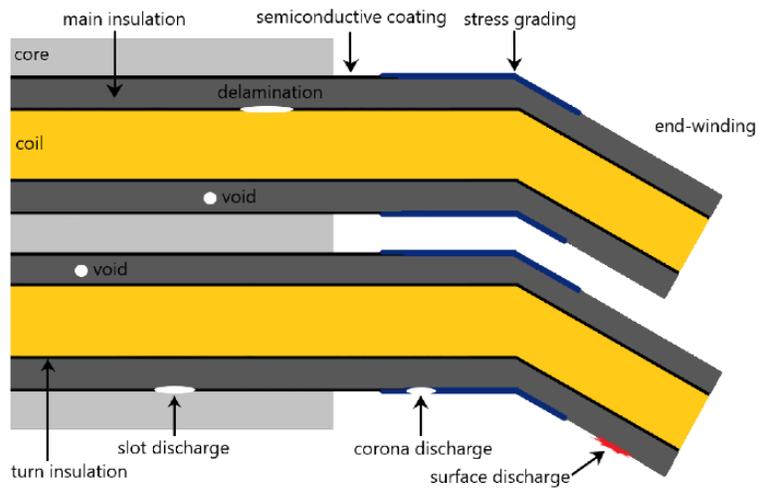
Figure 3.5: PD sources in the winding system
[77]

3.2 Diagnostic Tests

Team stresses and manufacturing stresses significantly contribute to the deterioration and aging of insulation, exacerbating its condition. Therefore, regular diagnostic tests play a pivotal role in the early detection of insulation issues, preventing catastrophic failures, and prolonging the lifespan of electric machines. Insulation testing occurs in various contexts, including intrinsic material characterization for collecting design data, factory acceptance, end-of-line testing on individual machines, or statistically sampled coil assemblies before product dispatch. Other testing contexts encompass scheduled in-service testing for periodic condition assessment, continuous condition monitoring, repair quality verification, and end-of-service testing to establish remanufacture or refurbishment strategies [21]. Consequently, measuring similar values on operational machines can reveal changes in insulation condition, enabling the estimation of the remaining lifetime [76].

There are two categories for electrical insulation tests: online tests and offline tests. Online testing occurs while the electrical machine is in operation, extracting real-time stresses on electric machines to monitor insulation material degradation. However, online testing may not reveal all failures inside an electrical machine comprehensively. Hence, offline tests are essential. In offline tests, methods are applied shortly after an electrical machine shuts down and is disconnected from the supply, providing an estimated maintenance time to avoid unexpected downtime [26]. As offline diagnostic tests are crucial for maintenance, condition monitoring, or experimental test procedures related to the insulation system of electrical machines, the main offline diagnostic tests will be analyzed.

The most significant progress has been made in assessing stator winding insulation, primarily because most machine insulation failures occur in the stator winding. Additionally, most available methods for stator windings offer diagnostic information on the extent of insulation deterioration, not just whether the insulation has already failed [75]. Despite various diagnostic tests, no standalone test can unequivocally determine an insulation system's health with certainty. Therefore, inspection strategies deploy combinations of methods to avoid misdiagnosis and provide a comprehensive assessment [21], [25], [26]. Lastly, when conducting test procedures, adherence to industry standards (IEEE/IEC) and manufacturer guidelines is essential [21].

🔸 Insulation Resistance (IR) & Polarization Index (PI) [25], [81], [82]

One of the most widely used tests for evaluating the insulation of both stator and field windings is the Insulation Resistance (IR) test, often augmented by the Polarization Index (PI) test. These tests serve to identify outright insulation failures, surface contamination, and moisture, providing crucial insights into the overall insulation condition.

As detailed in [82], the test procedure involves applying a direct current (dc) voltage across the winding insulation, measuring the resulting current after a specific duration, and employing Ohm's law to calculate the insulation resistance. An extended version of the insulation resistance test involves recording additional data over 10 minutes, with the Polarization Index calculated as the ratio of the results at one minute to those at ten minutes.

➤ $PI = \frac{R_{10}}{R_1}$

In an ideal insulation system, the test current would be zero, indicating infinite resistance. However, practical insulation systems exhibit a decreasing current magnitude over time, potentially reaching a steady state. This measured current comprises four components: capacitive, conduction, surface leakage, and absorption (or polarization) currents.

- o   Capacitive Current

Upon applying the DC test voltage, a current charges the capacitance formed by the winding insulation, determined by the winding capacitance and the resistance of the winding-test instrument combination. This current quickly decays to zero, typically within a few seconds (<10 s), making it negligible for insulation resistance readings.

- o   Conduction Current

This current results from electron migration through the insulation. It remains constant during the test and is minimal for effective and dry insulation (ideally zero). Elevated conduction current may indicate physical damage, cracks, or moisture absorption in the insulation.

- o   Leakage Surface Current

Independent of the test duration, this current flows along the insulation surface and is often caused by contaminants like oils or conductive dust. Wet surface contaminants can contribute to this current.

- o   Absorption Current

The result of polar molecules reorienting under the applied DC voltage, absorption (or polarization) current tends to decay toward zero in 10 minutes for typical insulation systems. It is an aggregate of various individual currents with different decay time constants.

Analyzing changes in test current or insulation resistance during the test provides insights into insulation condition. A consistently high or steady current may indicate contamination or moisture due to surface leakage or conduction current, while a steadily decreasing current suggests a clean and dry winding due to absorption current.

Electrical insulation testing is a routine part of time-based maintenance to monitor insulation condition and guide maintenance planning. IR and PI testing precede higher voltage tests and are conducted after suspected insulation failures for diagnostic purposes.

Like any electrical testing procedure, it is imperative to implement measures to guarantee the safety of personnel. It is crucial to confirm that only the designated equipment intended for testing is energized, and following the completion of the test, the equipment should be properly grounded for an appropriate duration to dissipate any potentially hazardous charges.

While IR depends on insulation temperature and requires correction for year-to-year comparisons, PI test results can be compared across multiple years without correction due to minimal insulation temperature change during the PI test.

⬇ Polarization/Depolarization Current (PDC) [27], [75], [83]-[85]

The measurement of Polarization and Depolarization Currents (PDC) is a crucial DC method employed to evaluate the insulation condition of various equipment in the power system, including power transformers and rotating machines. Unlike traditional methods like Polarization Index (PI) and Insulation Resistance (IR), which measure polarization current at only one or two points, the PDC measurement continuously assesses both polarization and depolarization currents, offering more comprehensive insights into the dielectric response of the insulation system.

The PDC test involves applying a high constant DC voltage step to a capacitive test object, such as a stator winding, for a duration ranging from 10 to 30 minutes. Subsequently, the DC supply is disconnected, and the test object is short-circuited to ground for an equivalent or shorter duration. Current is measured during both the charging and discharging periods. The current observed during the application of the step DC voltage is known as the polarization current (also referred to as charge or relaxation current), while the current measured during the short-circuit process is termed the depolarization current (or discharge current). The discharge current is then inverted and displayed on the same time axis as the charging current, ideally overlapping. Any deviation from this overlap may indicate insulation contamination, uncured epoxy, or potential delamination of the insulation due to thermal aging in the stator winding.

When testing an entire machine, all three phase windings can be measured simultaneously or one phase winding at a time, with the remaining two either grounded or electrically floating. Moreover, the test can utilize multiple voltage levels in a sequence, ranging from 1 kV to 10 kV.

✦ <u>High Potential (Hi-Pot)</u> [25], [86]-[88]

High-potential (also called over-potential) tests, commonly referred to as "hi-pot" tests, entail applying a voltage higher than the rated voltage between winding conductors and ground. The objective is to uncover insulation flaws that might lead to a near-term failure while in service. These tests are proof-oriented, providing a binary "go/no-go" outcome without offering extensive diagnostic or condition assessment information. The primary assurance from a hi-pot test is that the winding insulation can withstand the test voltage on the day of testing, assuming typical gradual degradation of the insulation system. Should the winding fail to withstand the test voltage, an invasive repair and retest become imperative before the machine can resume operation. Two main types of high-potential tests exist: DC hi-pot tests and AC hi-pot tests.

In a conventional DC over-potential test, similar to the Insulation Resistance (IR) test, the windings are prepared in the same manner. The test voltage is smoothly increased from zero volts to the desired level, maintained for one minute, and then gradually decreased back to zero volts. The winding successfully passes the test if it sustains the test voltage for one minute without disruptive insulation failure or tripping of the test set overcurrent protection. However, this test provides limited diagnostic insights.

The AC over-potential test mirrors the DC version but uses a 50/60 Hz AC voltage. The procedure involves raising the test voltage smoothly, holding it for one minute, and then gradually lowering it. Similar to the DC test, success is determined by the sustained test voltage without disruptive insulation failure or tripping of overcurrent protection. Nevertheless, this test also offers minimal diagnostic information.

Choosing between AC and DC over-potential tests involves several factors. Firstly, the equipment's size and cost influence the decision, as DC test equipment tends to be smaller, less expensive, and more portable. Secondly, the distribution of the applied test voltage across the winding's ground insulation varies between DC and AC tests. In the DC test, voltage distribution aligns with component resistivity, while in the AC test, it aligns with insulation component capacitance. This leads to different voltage distributions, with neither equivalent to the in-service voltage distribution. In modern epoxy mica insulation systems, the DC test may not reveal flaws that the AC test can detect. Additionally, applying an AC voltage equal to or exceeding the winding's rated voltage in AC over-potential testing may induce partial discharges, causing slight aging in the winding.

DC Ramp Test (DCRT) [83], [86], [89]-[91]

The DC Ramp Test is a meticulously controlled examination involving a gradual increase in DC voltage at a constant rate, typically set at 1 or 2 kV/min. The resulting I-V response curve is automatically plotted and displayed on the measuring instrument, serving dual purposes. Firstly, the characteristic curve, derived from the applied voltage and measured current, allows for comparison with future or past test results to identify abnormalities. Secondly, the real-time feedback provided by the curve enables the test technician or engineer to detect sudden changes in current, potentially preventing insulation rupture before it occurs.

Comparing the DC Ramp Test (DCRT) with the Polarization/Depolarization Current (PDC), it becomes evident that, although both tests rely on the same current contributions (absorption and conduction), they may unveil distinct diagnostic features due to differences in their insulation stress. Notably, the capacitive current experiences a rapid decline during a PDC test, contrasting with its nearly constant nature throughout the DCRT due to the continuously increasing voltage. Furthermore, the DCRT typically reaches a higher maximum voltage than PDC tests, allowing it to stress smaller defects more effectively.

Compared to conventional DC hi-pot tests, the DC Ramp Test boasts relative compactness in test equipment. The elimination of manual voltage adjustments enhances both voltage control and test sensitivity. Simultaneously, continuous monitoring of the charge current transforms the assessment of insulation condition from a simple go/no-go test to a more nuanced evaluation.

♦ Capacitance & Dissipation Factor (DF) [92]-[97]

In an ideal scenario, an insulating material would function as a lossless capacitor, leading to a purely capacitive current when subjected to a sinusoidal voltage. This current would be 90° out of phase with the voltage. However, real-world insulating materials exhibit dielectric losses. Consequently, when exposed to a sinusoidal voltage, the resulting current leads the voltage by an angle equal to 90° minus δ, where δ represents the dielectric loss angle.

Under sinusoidal excitation, a non-ideal dielectric is defined by a complex relative permittivity ε_r^*. The real part, ε_r', reflects the relative permittivity, associated with the stored energy inside the insulating material. Meanwhile, the imaginary part, ε_r'', serves as the relative loss index, also known as the loss factor. This factor is linked to the energy dissipated within the insulating material during the process.

Non-ideal insulation is commonly modeled through the use of an ideal capacitor C in parallel to a resistor R, where capacitance denotes the equivalent capacitance between the stator conductors and ground, and resistance represents the dielectric losses within the insulation. Upon energizing the stator conductors (excited with a sinusoidal voltage), capacitive and resistive currents emerge, with δ denoting the angle between the capacitive current and the total current. The dielectric dissipation factor is defined as the tangent of the dielectric loss angle δ. Hence, it can be calculated as the ratio between the resistive current I_R and the capacitive current I_C, or as the ratio between the imaginary and real parts of the complex relative permittivity. The measured capacitance value and tanδ, serve as indicators of the overall health of the system insulation.

➢ $\tan \delta = \dfrac{I_R}{I_c} = \dfrac{\varepsilon_r''}{\varepsilon_r'}$

Further, the dielectric loss is the sum of solid losses (i.e. conduction and polarization losses) and ionization losses (i.e. losses due to the inception of PDs), therefore, for small values of δ, tanδ is determined by the sum of tanδ_S and tanδ_{PD}, where tanδ_S is the term accounting for solid losses, whilst tanδ_{PD} is the ionization loss term:

➢ $tan\,\delta = tan\,\delta_S + tan\,\delta_{PD}$

Capacitance measurements are valuable in identifying thermal deterioration, moisture absorption, and contamination at the end windings of the stator winding, as these factors alter the effective capacitance between the stator conductors and the ground. Simultaneously, the dissipation factor, reflecting dielectric losses in insulation materials, not only signals thermal deterioration, moisture absorption, and end-winding contamination but also highlights corona activities and damage. Consequently, observing the trends in measured capacitance and dissipation factor enables the diagnosis of insulation problems and provides insights into its overall health condition.

In an ideal insulation scenario, the dissipation factor should not rise as the applied voltage increases. At low voltages, the dissipation factor remains unaffected by voltage variations, because even if insulation's voids do exist, the ionization process will not arise and the tanδ value will only be dependent on the solid loss term (i.e. tanδ = tanδ_S). However, when AC voltage is elevated across the insulation in a stator coil or bar and voids exist within the groundwall or main insulation, partial discharges may occur at a certain voltage threshold; this voltage value inducing PD inception is commonly called ionization voltage, corona inception voltage or PDIV. These discharges generate heat, light, and sound, consuming energy that must be supplied by the power source. Consequently, in a defective stator coil or bar containing voids or delamination, the dissipation factor increases beyond the normal level due to inherent dielectric losses in the solid insulation. Partial discharges contribute an additional loss component to the insulation, making the increase in dissipation factor indicative of the void content in the stator winding insulation. In other words, the term tanδ_{PD} will steeply rise along with the excitation voltage. While a high dielectric loss does not necessarily signify a defective insulation system, a low power factor and power factor tip-up are generally preferred. Unfortunately, dielectric dissipation factor

measurements do not reveal the distribution of loss within the insulation system, preventing the identification of specific weak points.
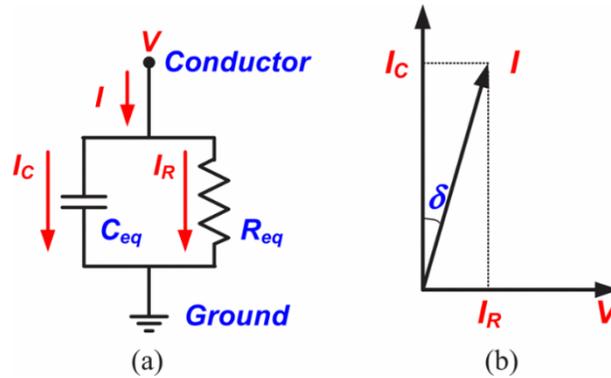

Figure 3.6: (a) Equivalent circuit of insulation: (b) Phasor diagram of resistive and capacitive currents [95]

The fundamental approach involves assessing the dielectric dissipation factor across a range of voltages to derive various characteristic dielectric loss parameters for evaluation. Traditionally, practitioners of dissipation factor measurements rely on three key parameters to gauge insulation condition:

1. The absolute dissipation factor value at a specified voltage, typically the rated phase-to-phase or phase-to-ground voltage.

2. The incremental change in dissipation factor as the voltage is incrementally raised.

3. The alteration in dissipation factor as the voltage increases from prescribed minimum to maximum voltages, known as the dissipation factor tip-up.

More specifically, the dissipation factor tip-up test, also termed delta tan delta, entails measuring the difference between $\tan\delta$ at two designated voltages. The low-voltage dissipation factor, DF_{lv}, serves as an indicator of inherent dielectric losses in the insulation. Subsequently, the voltage is elevated to the rated line-to-ground voltage, and the dissipation factor at this voltage, DF_{hv}, is measured. The dissipation factor tip-up is then calculated as follows:

➢ Dissipation factor tip-up ($\Delta\tan\delta$) = $DF_{hv} - DF_{lv}$
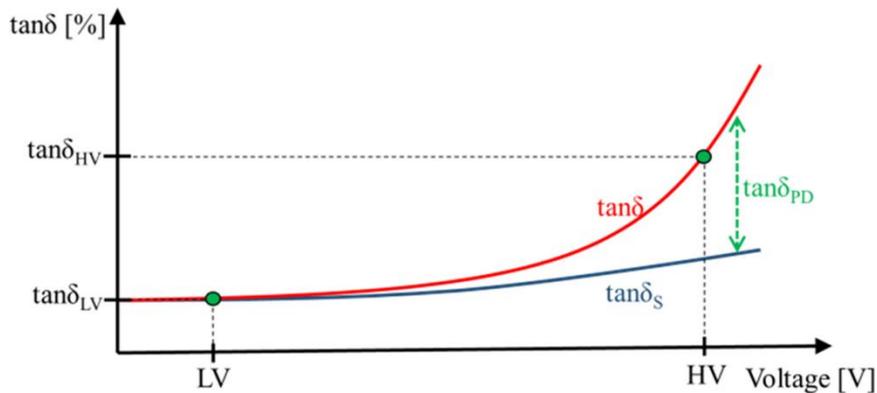
Figure 3.7: Test voltage influence on the tanδ measurement
[97]

For individual stator coils and bars, the test setup involves applying electrodes to the slot portion, where the semicon, acting as the outer corona protection layer in either paint or tape form, has been applied. This electrode is linked to the device measuring the capacitance and dissipation factor. Most measurements utilize a bridge method, such as a Schering bridge or a transformer ratio arm bridge, where the test object is compared to a reference capacitor characterized by extremely low dielectric loss and voltage coefficient. More contemporary bridges employ digital methods to measure the phase difference between currents from the test object and the reference capacitor.

Stator windings rated above 4.0 or 6.0 kV commonly feature a stress control coating (grading system) with a high-resistance material layer on the overhang portions near the stator core. The grading system exhibits a nonlinear resistive characteristic concerning voltage to regulate voltage distribution on the stator coils' surface. Power loss in the grading system increases with applied voltage, impacting the measured power factor and power factor tip-up of the insulation system. Therefore, power factor tests may be misleading for stator windings equipped with a grading system. When testing individual coils and bars, minimizing the tip-up contribution due to the stress relief coating is achievable by "guarding" out the currents from the silicon carbide with grounded aluminum foil or isolating the silicon carbide coating from the semicon coating and grounding it separately.

Partial Discharge (PD) [25], [77], [98]-[101]

Partial discharges (PD) represent small electrical sparks that may occur within any electrical insulation system and PD testing is performed to assess significant stator insulation aging during service. Nowadays, major motor and generator manufacturers routinely gauge PD activity using a conventional PD detector on stator coils or complete windings. During off-line testing, the stator winding is disconnected from the power system and energized to its rated voltage using a test transformer. Such tests help identify manufacturing issues like poor impregnation, insufficient spacing between coils at the end windings, and defective PD suppression coatings.

When a partial discharge occurs, it generates a brief pulse of current, along with radio frequency (RF) emission, light, and a gas pressure wave (sound). Detection of light and sound from a PD is only possible if the PD site is on the surface of the coils. The optical signal from PD in the air primarily falls within the ultraviolet frequency range, while the acoustic signal mainly lies in the ultrasonic range (around 40 kHz). RF emissions cover a frequency range from 0 Hz to a few hundred MHz.

In off-line tests, PD can be measured using:

o A "conventional" detector that measures the associated current pulse from the stator winding.
o A customized radio receiver, often called a "corona probe" or "EMI sniffer," to measure and locate RF emissions.
o An ultrasonic microphone to measure and locate acoustic emissions.
o An ultraviolet imaging device to locate the PD on the surface of the insulation.

If the winding is exposed, all four methods can be applied. However, if the machine is fully assembled, making the stator winding inaccessible, only the first "conventional" PD test can be performed.

In the conventional PD test, adopted for over half a century, the PD current is detected using a high-voltage capacitor on the machine terminals. The capacitor, typically 1 nF, attenuates the

50/60 Hz AC high voltage from the power supply while presenting a low impedance to the high-frequency components of the PD pulse. The output of the detection capacitor is connected to a (typically) 50-ohm resistor in parallel with an oscilloscope, radio receiver, or a specialized PD instrument. The PD pulse current is then converted to mV. A dedicated PD instrument may directly display the mV or convert the pulse currents back to mA, nC (nano Coulombs, a unit of charge), or other derived quantities. Standards emphasize measuring PD in the 50 kHz to 1 MHz frequency range (the low-frequency or LF range) when using a conventional PD detector.

During the off-line PD test, a 50/60 Hz high voltage supply energizes the stator winding to the rated line-to-ground voltage. As the voltage increases, the PD inception voltage (PDIV) is measured, along with the magnitude of the PD at rated line-to-ground voltage. When the voltage is decreased after a set period at a prescribed test voltage, the PD extinction voltage (PDEV) is also measured. The PD magnitude typically expressed as Qm, the pulse magnitude at a PD repetition rate of 10 pulses per second (pps), is often measured at the rated phase-to-ground voltage.

Voltage Endurance (VE) [102]-[106]

The VE test relies on examining a population of specially prepared samples representing the insulation system or randomly selected samples from the evaluated manufacturing product. There are essentially two distinct approaches to the VE test: the first employs a "pass-fail" criterion, while the second involves testing a population of samples until at least 50% of them fail. The second approach enables the assessment of insulation life expectancy through statistical postprocessing of empirical test results. This evaluated life expectancy facilitates the comparison of different insulation systems and the assessment of potential insulation aging under operational electrical stress. Standards that solely employ Pass/Fail criteria offer limited information about the insulation, whereas a VE test conducted until at least 50% of the samples fail provides significantly more insights into the insulation system.

Selecting the testing electrical stresses in a comparative reference with operational conditions poses a perennial challenge. If test stresses are too low compared to operational conditions, the tests' duration may extend to impractical lengths of months or years. Conversely, a substantial increase in operational stress alters the aging mechanism, rendering the test results inconclusive and lacking significance for insulation lifetime prediction and qualification under operational conditions. The test voltage value should be chosen at a level where the electrical aging mechanism aligns with operational conditions but proceeds at an accelerated pace for conclusive test results. To ensure meaningful outcomes, the applied electrical stress should be selected to allow for a test time of no more than 3 months, but at the very least, a few hours.

✦ Surge Test [86], [107], [108]

During the surge test, the stator winding undergoes the application of voltage impulses characterized by short rise times and relatively high magnitudes. This stress is designed to mimic the impact of external surges encountered during service, specifically targeting the turn insulation. Successfully passing this test ensures that the motor possesses the capability to withstand impulses below the corresponding voltage/rise-time level administered in the surge test.

The surge test involves charging a capacitor, denoted as C, to a predetermined level, followed by its discharge into the RLC series circuit. This process induces a damped oscillation at the resonant frequency, where L represents the inductive component of the stator winding.

➢ $f = \frac{1}{2\pi\sqrt{LC}}$
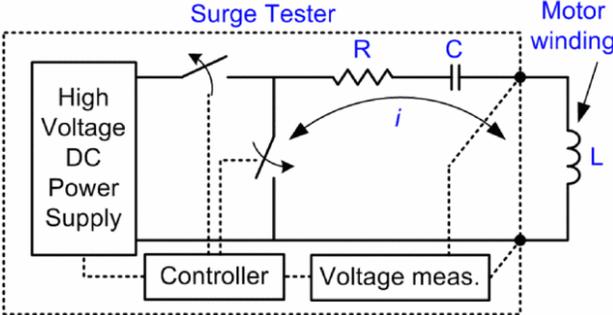
Figure 3.8: Schematic of typical surge test circuit
[107]

The surge voltage level is incrementally raised in discreet steps, gradually reaching the predetermined voltage level. When the surge test voltage is applied to the line end turns with compromised turn insulation, it can trigger arcing due to pre-existing conditions such as exposure between copper turns or the puncturing of weak insulation. If arcing occurs, the inductance value (L) decreases due to shorted turns, and the resonant frequency (f) increases. Consequently, the surge waveform shifts to the left as the voltage step rises, serving as an indicator of arcing between turn insulation. Modern surge testers exhibit high sensitivity, enabling them to detect subtle shifts in the surge waveform caused by a relatively small number of shorted turns.
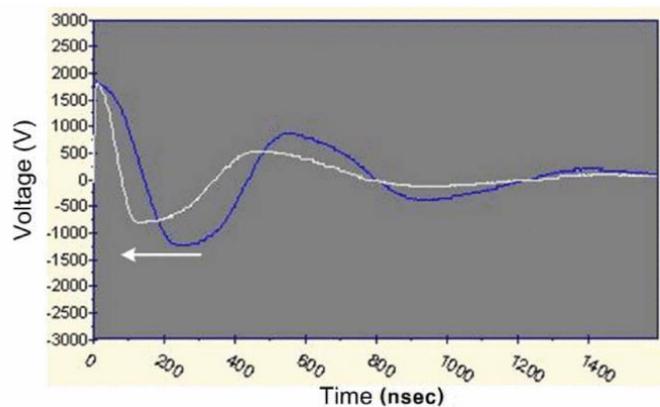
Figure 3.9: Surge waveform measurement under surge test failure
[107]

While the surge test operates on a pass/fail basis and does not provide insights into the specific "condition" of turn insulation, it stands as the sole test capable of potentially averting costly in-service insulation failures caused by fast rise-time surges. Typically conducted for qualification or acceptance purposes, there are reservations about its application in maintenance testing due to the relatively high voltage required. Field concerns regarding maintenance testing revolve around two main issues: 1) the potential degradation of healthy insulation and 2) the risk of failure in insulation that might have operated successfully over an extended period without testing. Results indicate that the PD inception voltage (PDIV) generally exceeds the surge test voltage specified in maintenance testing standards, and there is no noticeable degradation under impulse excitation conditions more severe than those in the surge test. Concerning the first issue, the likelihood of surge testing causing insulation deterioration is minimal. This is supported by the fact that the surge withstands voltage for new motors is significantly higher than the PDIV, and the surge test

72

is an infrequent offline procedure. Addressing the second concern, if a motor with weakened turn insulation fails the surge test, standard practice dictates not operating the machine, as it is likely to fail shortly. Conversely, employing the surge test strategically within the maintenance cycle can prevent unplanned outages and significant financial losses due to in-service motor failures. Therefore, determining the optimal timing and maximum voltage level for surge testing becomes a crucial strategic decision in the maintenance cycle.

Spectroscopy [109]-[112]

Spectroscopy has long been a subject of extensive research, utilized for testing, ex-situ inspection, condition assessment, and partially in-situ, employing various voltage strategies. In the literature, spectroscopy studies can be divided into early investigations utilizing Broadband Dielectric Spectroscopy (BDS), and those within the last two decades focusing on Electrical/Electrochemical Impedance Spectroscopy (EIS).

o   Dielectric Spectroscopy

Dielectric Spectroscopy involves measuring the dielectric properties of a material or component by analyzing the response of the dielectric permittivity across the frequency spectrum. This method evaluates polarization and conductivity by analyzing the response of dipoles and dipole moments within the material, notably leading to dielectric displacement. The real and imaginary parts of the permittivity respectively indicate dielectric strength and loss. This method facilitates the detection of degradation in dielectric samples, conductors, or insulation components. While BDS can detect electrical insulation degradation attributed to phenomena like synergic effects, dielectric relaxation, and conductive contributions, it has limited effectiveness in identifying deficiencies such as corrosion, manufacturing defects, or early-stage insulation failures. Previous research has primarily focused on defining complex dielectric permittivity, complex capacitance, power factor, and tanδ.

o   Impedance Spectroscopy

In the past two decades, the limited effectiveness and interpretational challenges of dielectric spectroscopy have spurred a surge in research interest in electrical impedance spectroscopy. This method has become increasingly popular for modeling electrical insulation in various applications such as power transformers, cables, machine windings, and converter drives. It allows for thorough analysis of the tested component or system, facilitating equivalent circuit analysis through the frequency domain representation of total complex impedance. By employing impedance spectroscopy, researchers can determine the system's electrical circuit order, characterize it, and assess its stability using transfer functions derived from equivalent circuits. The technique utilizes impedance Bode plots to unveil details about amplitude and phase response, including electrical resonances within components. Furthermore, impedance spectroscopy offers the capability to scrutinize impedance functions through Nyquist plots, illustrating the real and imaginary components' locus over the frequency range tested. In recent times, impedance spectroscopy has garnered increased attention from both the research community and industry. It serves as a valuable tool, enabling low-voltage, non-destructive measurements for detecting manufacturing deficiencies, material anomalies, and incipient faults. Additionally, it aids in studying thermal, mechanical, and electrical stresses, as well as assessing the cumulative impact of combined stresses, including environmental factors.

3.3 Insulation Aging via Thermal Cycling

🔸 Thermal Cycling

Insulating materials undergo aging, defined as the irreversible alteration of their properties due to normal use [76]. Single-factor aging occurs when one type of stress dominates, while multifactor aging involves several stresses. Dominating stresses can change throughout a component's lifetime, and aging stresses can manifest simultaneously or sequentially. Even if one mechanism dominates aging, failure can result from multiple stresses. It's advisable to apply several stress factors simultaneously in testing to mimic service conditions, despite the complexity of replicating aging processes in the lab. The primary aging stresses on insulation, known as TEAM stresses (thermal, electrical, ambient, and mechanical stresses), are particularly significant.

The thermal stresses affecting electrical insulation systems encompass various factors, as outlined in reference [76]:

1. Chemical degradation reactions, polymerization, diffusion, and similar processes induce both chemical and physical changes.

2. Thermomechanical effects arise from the forces generated by thermal expansion and contraction.

According to reference [76], thermomechanical effects can instigate five distinct aging processes for winding insulation:

1. *Loss of adhesion:* Over numerous thermal cycles, the bond between groundwall insulation and copper may weaken, leading to adhesion loss at the boundary between copper/strand insulation and groundwall insulation. Delamination at this interface poses a greater risk than voids within the insulation, as it could damage strand insulation. Delamination within the groundwall insulation or at the interface between groundwall insulation and copper conductors also diminishes thermal conductivity, hastening aging.

2. *Delamination between insulation layers and between the insulation and the conductive layer* can occur due to the same shear stresses.

3. *Abrasion on the outer surface of the insulation:* This can result from the expansion and contraction of stator windings, causing the insulation or coating to rub against the slot's side.

4. *Circumferential cracking of insulation (tape separation/girth cracking), particularly in the section extending from the slot:* This phenomenon is common in machines with mica-asphalt insulation and long stator cores. In these machines, groundwall insulation can swell radially just outside the slot when hot, becoming trapped outside the slot when cooled. Consequently, the insulation at the slot's end undergoes stretching and compression during numerous thermal cycles, potentially causing axial (tape separation) and radial (girth cracking) separation of tape layers.

5. *Mechanical damage to the insulation due to distortion of winding end turns:* Thermomechanical forces may loosen the packing of the stator winding, leading to vibration of the stator winding ends and potential damage to the insulation.

According to references [76] and [113], thermomechanical effects stem from the stresses that arise during temperature fluctuations, leading to the expansion and contraction of various materials. These temperature changes are commonly known as thermal cycling (TC). In the stator winding, temperature rises and falls in response to the ohmic losses in the copper conductors. The insulation adjacent to the copper experiences the same temperature as the copper itself, while the temperature gradually decreases throughout the insulation. Cooling is facilitated by the iron core, causing the insulation near the stator core to maintain a similar temperature to the core itself. As the temperature of the stator winding increases, the copper conductor expands, and it contracts as the temperature decreases. However, the insulation, with its lower temperature and coefficient of thermal expansion compared to copper, undergoes less expansion and contraction. This discrepancy in expansion and contraction generates shear stress between the conductors and the insulation. Insufficient bonding between the copper and the insulation may lead to copper separation, resulting in voids between the insulation and the copper and potential debonding,

allowing for relative movement of the copper strands or turns. Additionally, voids can develop between the layers of groundwall insulation due to delamination.

As per reference [114], the thermal expansion of a material is governed by the change in temperature and its coefficient of thermal expansion. This concept typically assumes stress-free volume changes, implying no constraints across any boundaries, allowing for free expansion in all three axes. However, in this scenario, such ideal conditions do not hold. Constraints exist on both the stator and the coil, which hinder thermal expansion along certain axes. For instance, the coil experiences relatively more freedom to expand lengthwise compared to widthwise, with the stator walls providing opposing forces. This opposing force generates stress between the stator wall and the coil during thermal expansion. As the temperature of the copper rises, the coil undergoes volume expansion. If the stator does not expand at a matching rate, significant stress is exerted on the insulation layers bonding the copper conductor to the steel slot. This stress can result in damage and deformation of the insulation. While stresses on the coil are inevitable, they may be heightened during periods of rapid elevation in winding temperature.

As previously discussed, thermomechanical stress arises from thermal gradients and mismatches in thermal expansion between adjacent materials. Thermal cycles, such as on/off duty cycles and changes in load or speed, repeatedly subject insulation components to thermomechanical stress, leading to damage to the integrity of the stator insulation system and a reduction in winding service life [113], [115]. Considering that motors for automotive applications endure variable torque and speed operations [116], and are utilized in environments with continuously changing conditions and complex duty cycles, resulting in fluctuating temperature profiles [117], it's anticipated that the stator winding temperature will vary considerably [118]. Given these conditions, insulation testing for such electric machines should prioritize a variable temperature profile over a constant one in terms of thermal stress. A variable temperature profile more accurately reflects the actual conditions experienced by high-performance electric motors, particularly when they encounter thermal overload for short durations [116]. Therefore, it's crucial to thoroughly investigate the thermal cycle aging performance of epoxy and its micro-composites [119].

Related Work

As previously discussed, the evaluation of insulation systems through thermal stress testing can be conducted via fixed thermal degradation or thermal cycling aging. The fixed thermal degradation involves subjecting the insulation to a constant temperature, traditionally achieved through passive means like convection within specially designed chambers [20], [110], [120]-[123]. Conversely, thermal cycling testing, while less common in literature, offers a more representative evaluation method. This approach effectively replicates the thermomechanical stresses encountered in applications such as electric vehicle (EV) motor windings where thermal gradients are prevalent. Given the significant thermal inertia of such assemblies and the necessity to observe degradation within a reasonable timeframe, standards recommend the active method for thermal cycling. This involves Joule heating, achieved by passing a current through the windings or coils. Subsequently, diagnostic tests are conducted post-stress, or even between stress cycles, to monitor the insulation's condition.

Test Specimen & Thermal Cycles

In many cases, testing the entire machine is impractical due to space constraints. Consequently, thermal stresses and diagnostics are conducted on individual components such as coils, bars, or even motorettes [115]. A diverse array of coils and bars have been studied in the literature, featuring varying rated voltages, insulation materials, thermal classes, and workspaces.

The thermal cycling (TC) experiment typically involves subjecting the coil to repeated heating cycles up to an upper-temperature limit dictated by the insulation class, followed by cooling. Test setups typically utilize current induction for heating and external cooling systems. The coils, arranged either in series [97], [115], [125], [127], [129] or in parallel [124], [130], [132], are connected to the output terminals of a current transformer. Control of the current transformer can be managed via an external digital signal processor (DSP) [97], [118] or by a relay-controlled switch [130], [132]. Temperature measurement is crucial and is often achieved using thermocouples attached to the coils or, in some cases, to dummy/control coils to mitigate

78

potential diagnostic inaccuracies resulting from sensor placement issues [125], [129]. Thermal cameras are also employed for temperature monitoring [126]. Forced air cooling is implemented to control the temperature of the copper.

TC experiments in the literature vary in terms of temperature ranges, rates of temperature change, cycle periods, and total thermal cycles. Temperature ranges typically span from 40-155 °C [113], [115], [126]-[129], [131], with some reaching up to 180-185 °C [124], [130], [132], while others start at 200 °C and reach up to 260 °C and 280 °C, respectively [97], [118]. The duration of temperature rise and cool-down phases determines the period of a thermal cycle, which can range from fast cycles lasting only a few seconds [97], [115], [118] to slower cycles lasting several minutes [113], [124]-[130], [132]. The total number of cycles generally ranges from 200-500 [113], [124]-[127], [129], [130], [132], with diagnostic tests—such as capacitance, dissipation factor, and partial discharge measurements—conducted every 50 cycles to assess the insulation's condition. Breakdown voltage tests may also be performed intermittently.
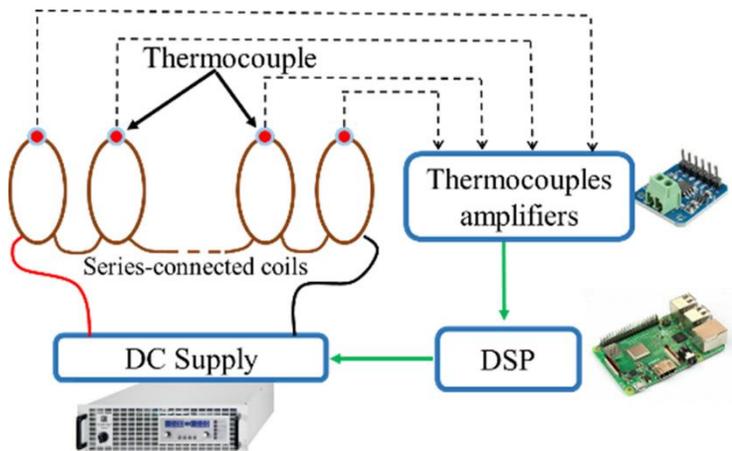
Figure 3.10: Typical testbench for thermal cycling test [97]
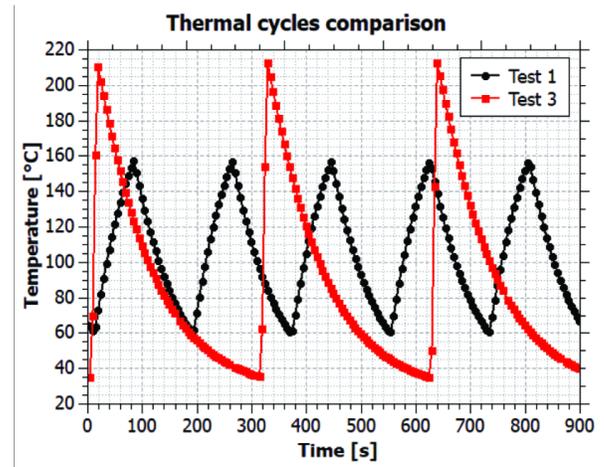
Figure 3.11: Typical thermal cycles [115]

79

o   Capacitance & Dissipation Factor (tanδ)

In thermal cycling (TC) experiments, the values of capacitance, dissipation factor (tanδ), and dissipation factor tip-up (Δtanδ) typically exhibit a general increase with both test voltage and thermal cycles, particularly in later stages. However, noteworthy variations have been observed in certain thermal cycling tests.

According to [125], backup coils tend to exhibit smaller tanδ values compared to serviced coils, with the difference between the tanδ of the backup coil before and after a few aging cycles attributed to moisture and post-curing effects on the insulation.

[97] indicates that both strand-to-strand capacitance and tanδ values are influenced by partial discharge inception voltage (PDIV). Initially, the strand-to-strand capacitance rises rapidly during early aging cycles, followed by a slower increase. Beyond PDIV, capacitance becomes voltage-dependent due to PD activity bridging air-filled voids between strands. Below PDIV, strand-to-strand tanδ measurements are affected by ambient relative humidity (RH), while above PDIV, significant increases are observed due to air void ionization.

In [113], the impact of delamination on capacitance and tanδ values is discussed. Coils subjected to thermal cycling showed variations based on delamination presence. Unaffected coils exhibited increased DF and DF tip-up values with thermal cycles, while capacitance increased marginally with cycle number and linearly with test voltage, indicating little change in void content. Conversely, delaminated coils showed increased DF values but decreased capacitance values after 300 cycles, indicating more than a little change in void content. If debonding occurs, air gaps between copper strands and groundwall insulation will expand, leading to a proliferation of voids. This expanded gap reduces the capacitance value between the copper strands and groundwall insulation. Furthermore, there is a notable increase in DF tip-up values after 300 cycles, indicating a rise in overall void content within the insulation system.

Reference [129] highlights findings where all tested bar types behaved similarly. Following thermal cycles, there was a general increase in tip-up, which continued with cycle number. After 250 or 500 cycles, tip-up values often decreased, albeit not returning to virgin levels. The exact cause of this phenomenon remains uncertain, but it could be attributed to alterations in the physical dimensions of delamination or voids. Essentially, as thermal cycling persists, the depth and area of individual delaminated regions may diminish, even though the overall volume affected by delamination expands.

Lastly, [124] reports a significant dissipation factor tip-up increase, indicating potential ground wall separation, but a notable improvement in dissipation factor measured at 2kV after thermal cycling, likely due to further resin cross-linking from thermal stress.
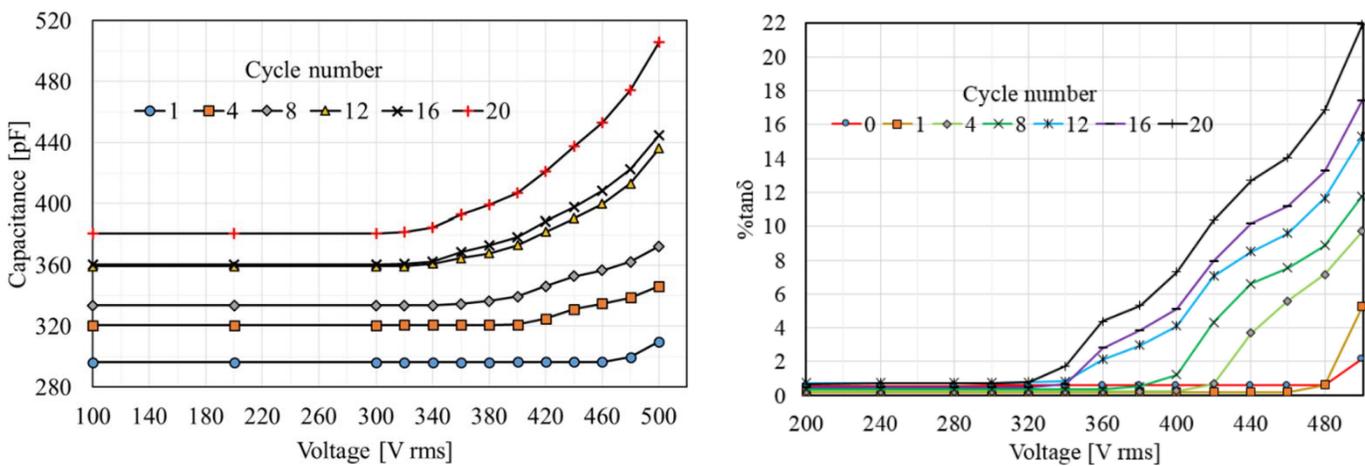
Figure 3.12: Typical increase of capacitance & tanδ values during thermal cycles
[97]

o   Partial Discharges (PDs)

During thermal cycling tests, there is a notable increase in partial discharge (PD) activity alongside a decrease in partial discharge inception voltage (PDIV). These trends vary among the coils and bars with different insulation materials under examination [124], [129].

This increase in PD activity is highlighted in [126], where although there was initially no significant change in PD trends during the early cycles, the average PD value surged significantly later on and continued to rise until eventual failure. This pattern underscores the progressive deterioration of the insulation and conductor interface due to aging, ultimately leading to failure. Tests conducted in [113] corroborate this escalation, noting a greater increase in PD activity for bars compared to coils.

Reference [125] delved into PD activity for both serviced-aged and backup coils, revealing intriguing findings. PD magnitudes exhibited considerable variability during the initial 25 thermal cycles, potentially attributed to static charge buildup in voids. Although PD activity disappeared after 50 to 100 load cycles for both back-up and service-aged coils, this did not necessarily indicate the end of insulation degradation; rather, it might be due to the presence of pseudo glow discharge within closed cavities, comprising minute discharge pulses challenging to detect with conventional PD detectors. A significant increase in PD magnitude for the service-aged coil occurred after the 180th thermal cycle, indicating the onset of PD activity at a specific weak point in the insulating system. Similar variations were observed in [129], where PD magnitudes often decreased after either 250 or 500 thermal cycles, although not returning to virgin condition levels. Authors tentatively attributed this to changes in the physical dimensions of delamination or voids, as thermal cycling progresses, resulting in decreased depth and area of individual delaminated regions despite an overall increase in delamination volume.

Regarding PDIV measurements, there is a consistent global decrease observed with the number of thermal cycles applied [115], [118], potentially leading to values smaller than those of backup coils [125].
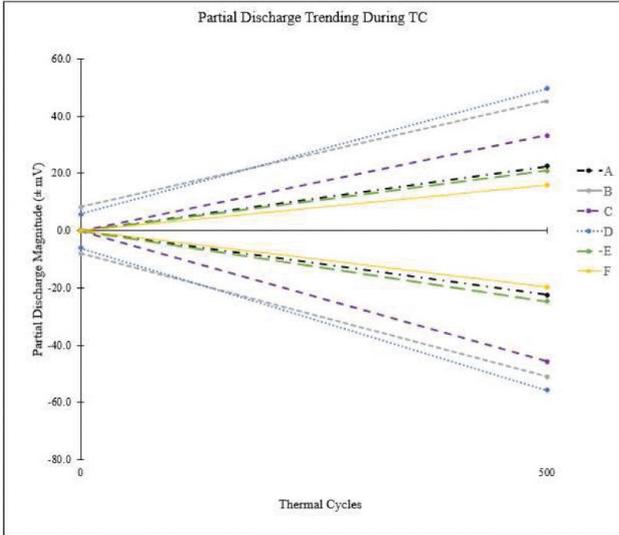
Figure 3.13: Typical increase in partial discharge magnitude during thermal cycles [127]
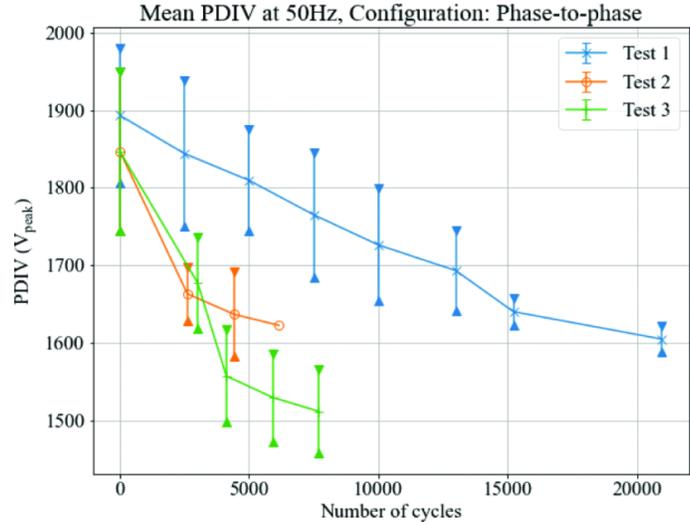

Figure 3.14: Typical PDIV drop after during thermal cycling [115]

o   Breakdown Voltage

Voltage Endurance (Breakdown Voltage) tests have been performed before TC experiments, potentially degrading the insulation and leading to premature delamination [128], but predominantly after thermal cycling (TC) experiments, revealing a reduction in the impulse breakdown voltage of coils.

References [130] and [132] compared impulse breakdown voltages for turn insulation in unaged coils, ranging from 34 kV to 36 kV with an average of 35.5 kV, to coils aged for 200 hours through TC at 185°C, which ranged from 11 kV to 17 kV with an average of 14.0 kV. These results underscore a clear decline in impulse breakdown voltage after cyclic heating and cooling, indicating significant degradation of turn insulation. Additionally, the authors subjected some coils to constant oven aging at 185°C but found no significant difference in breakdown voltages between unaged and oven-aged coils.

In [129], time-to-failure under voltage endurance testing was compared between virgin bars and bars subjected to 500 thermal cycles. For cases where failures occurred, the average time-to-failure for thermally cycled bars was only 24% of that for virgin bars, highlighting the substantial

83

impact of TC on voltage endurance test results and indicating insulation deterioration because of thermal cycling.

The type of insulation used plays a crucial role, as noted in reference [124]. While there was no significant change in surge breakdown voltage before and after TC for DDG over enamel or mica turn over enamel systems, a reduction in surge breakdown voltage was observed for mica over bare copper configurations.

o   Lifetime

In [117], the focus is on experimental investigation to validate the lifetime calculation model when applied to thermal cycling conditions. A novel methodology for estimating lifetime is proposed, which explicitly incorporates thermo-mechanical stress due to cycling. This is achieved by expanding the Arrhenius model, known for its accurate predictions of insulation lifetime under constant temperature conditions.

Reference [118] extracts the B-10 life, representing the time statistically required for 10% of test specimens to fail compared to the initial population. It's highlighted that the service life of specimens significantly diminishes with increasing thermal slew rate. Specifically, when comparing temperature profiles featuring 4°C/s versus 0.5°C/s, service life is reduced by more than 50%.

Furthermore, the authors of [118] attempt to elucidate this drastic shortening of service life by referencing fatigue and tensile curves of polyamide-imide (PAI) as a function of temperature. PAI is commonly used for overcoating enameled wires with a polyester-imide (PEI) basecoat. The PAI topcoat enhances magnet wire properties by providing better abrasion resistance and temperature resistance. The tensile curve illustrates the material's stretch capability under specific pressure up to ultimate tensile strength. At room temperature, PAI exhibits nearly complete elastic behavior, whereas, at higher temperatures, it displays more plastic behavior. This suggests that at elevated temperatures, short-term thermal cycles are likely to induce significant stresses due to mechanical hysteresis effects. This hypothesis is corroborated by fatigue curves, which indicate

the number of cycles PAI can endure under periodic stress: as temperature increases, the number of cycles at break decreases proportionally to stress intensity. Therefore, when insulation experiences abrupt temperature changes (e.g., temperature profiles with notable thermal slew rates), it undergoes stress not only thermally but also mechanically.
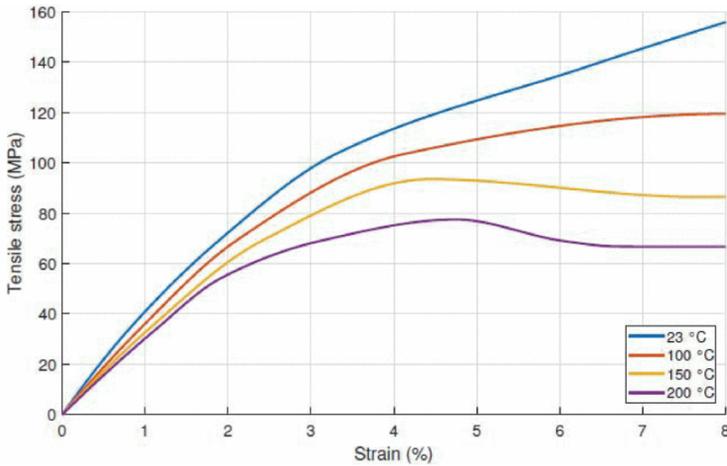

Figure 3.15: Stress-strain of PAI over a broad-temperature range [118]
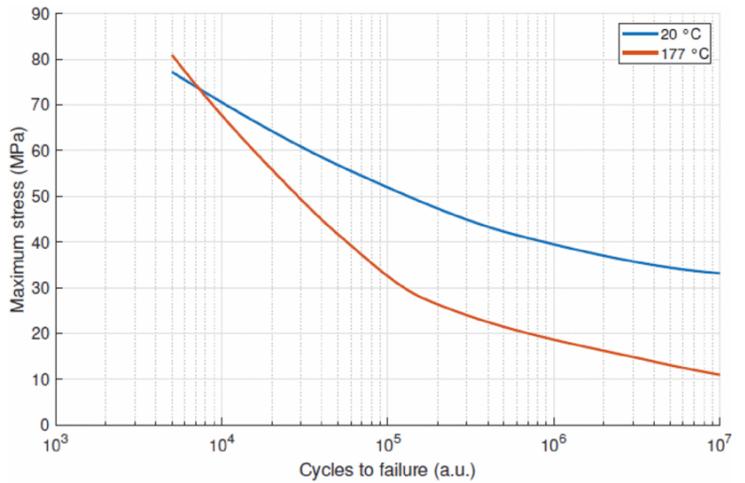
Figure 3.16: Flexural fatigue strength of PAI at two temperature levels [118]

o   Conclusions

Thermal cycling emerges as a substantial accelerant in machine degradation. Nevertheless, the above case studies reveal the effectiveness of thermal cycling tests as tools for quality assurance programs, particularly in pinpointing manufacturing inconsistencies like delamination or weak bonding in prototype and production stator coils and bars [127]. Various diagnostic tools were employed to detect delamination and debonding within the insulation system of stator coils and bars during and after TC testing. Non-destructive diagnostic tests facilitated the identification of delamination or debonding, subsequently corroborated by dissection and microscopic examination [97]. One of the primary stresses arising during thermal cycling is shear stress between the copper conductors and groundwall insulation. This stress can lead to bond loss at this interface, resulting in void formation and consequent increases in DF, capacitance tip-up, and

PD values of bars with debonding [113]. Despite some discrepancies in directly correlating diagnostic test results with observed defects during dissections or linking high dielectric dissipation factor (DDF) tip-up with a linear increase in partial discharges (PD), it is notable that early changes in diagnostic testing, such as tap tests, partial discharge measurements, and DDF tip-up values, can serve as indicators of potential manufacturing defects [127].

4) FRAX SWEEP FREQUENCY RESPONSE ANALYZER

Impedance spectroscopy served as the primary technique for monitoring insulation on the poles during the TEAMstress project. The FRAX-99 Sweep Frequency Response Analyzer manufactured by Megger was the chosen instrument for this purpose. The FRAX Sweep Frequency Response Analyzer (SFRA) is originally designed to identify winding displacements in power transformers or faults in the magnetic core. However, it has been adapted for the specific purpose of testing pole insulation, as verified by the company itself. This versatile system generates attenuation signature curves, facilitating straightforward comparison for any anomalies.

Frequency response pertains to the amplitude ratio and phase difference between voltages measured at two terminals of the test object across a spectrum of frequencies, with one terminal stimulated by a voltage source. The outcome of frequency response measurement manifests as a sequence of amplitude ratios and phase differences at specific frequencies within the frequency range. Frequency Response Analysis (FRA) is the method employed to identify damage through the analysis of frequency response measurements.

To elaborate, a multitude of low-voltage signals with varying frequencies are administered to the test object. Both input and output signals are meticulously gauged in terms of amplitude and phase, and their ratio delineates the frequency response or transfer function of the test object. This comprehensive transfer function furnishes several parameters such as magnitude, phase, impedance, admittance, and correlation as functions of frequency. Notably, the RLC network exhibits distinct impedance values at various frequencies. The transfer function encapsulates the effective impedance of the RLC network across all frequencies. Any geometric alterations induce changes in the RLC network, consequently modifying the impedance/transfer function across different frequencies.

Frequency response measurements are compared to discern potential issues within the test object. Indications of problems include alterations in the overall contour of the frequency response, variations in the number of resonances (peaks) and anti-resonances (valleys), and shifts in the positions of resonant frequencies.

4.1 Instrument Description

o Front Panel Indications

Figure 4.1: Front panel FRAX 99/101

1. **On / Off:** To activate or deactivate the instrument.

2. **DC input:** For connecting the AC/DC adapter.

3. **USB:** Type B USB connector for linking a USB cable to a PC.

4. **Antenna:** (only FRAX101) Bluetooth module enabling Bluetooth communication.

5. **GLD Test:** Conducts ground loop continuity checks.

6. **Generator (Yellow):** Output from the generator linked to the Reference via the Red Clip.

7. **Reference (Red):** Input for the reference, connected to the Generator via the Red Clip.

8. **Measure (Black): I**nput for measurement, connected to the Black Clip.

9. **Protective Earth/Ground connector:** Ensure the instrument is always connected to station earth/ground using a separate earth/ground cable. This connection should be established first and removed last.

o   Sweep Frequency Response

The FRAX Generator (Gen.) output produces a sinusoidal voltage at a specified frequency. The instrument features two distinct input channels: "Reference" (Ref.) and "Measure" (Meas.), which gauge both the generated voltage and the response voltage in terms of amplitude and phase. The device records amplitude and phase data for both the "Reference" and "Measure" channels, along with the ratio of "Measure" divided by "Reference". These values can be graphed and exported as Magnitude, Phase, Impedance, Impedance-Phase, Admittance, and more. FRAX employs the sine correlation technique, wherein the input voltages are multiplied by a sine and cosine function, and then averaged over an integer multiple of the time interval. The sine, cosine, and applied voltage all share the same frequency. This technique is widely recognized and suitable for Sweep Frequency Response Analysis (SFRA) measurements. Due to the identical treatment of signals on both input channels, the phase resolution between them is exceptionally high. The rejection of DC offset and harmonics (referred to as the applied voltage) theoretically approaches infinity. By increasing the integration cycles, the rejection gradually improves.
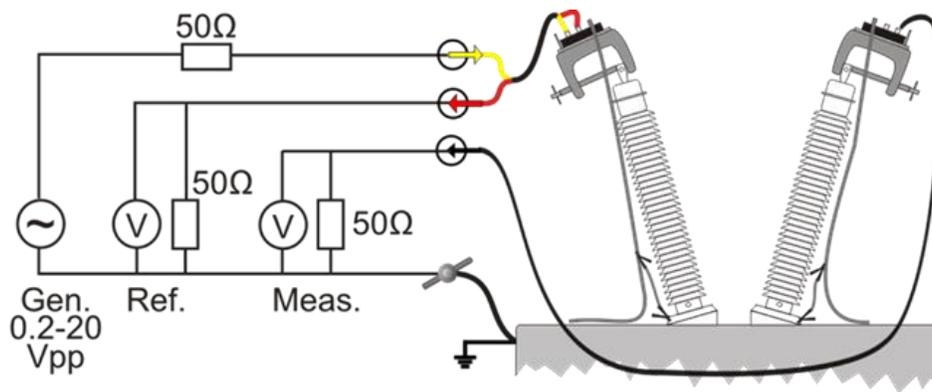
Figure 4.2: SFRA measurement circuitry

4.2 Test Procedure Tutorial

Utilizing the FRAX instrument, three distinct tests were conducted during the pole insulation assessment: one to gauge the overall pole impedance, another to compute the capacitance between the coil and the core, and a third to evaluate the insulation capacitance between turns. In all three tests, the procedure remained consistent, with the only variable being the location to which the analyzer electrodes were attached. The following section outlines a tutorial on executing impedance spectroscopy testing with the FRAX analyzer, irrespective of the particular test being conducted.

o   Verification of System

Before utilization, it's imperative to verify the continuity and integrity of the test leads. The most effective method for ensuring lead integrity and the accurate operation of the equipment is by conducting the SFRA self-check with a standard test object. This self-check holds particular significance for verifying the accuracy of SFRA test equipment, given the inherent challenge of intuitively determining the correctness of results during field measurements.

A short circuit test

- This test ensures the integrity of the test leads.
- Connect the "Source"/"Reference" and "Measure" clips together, and link the respective measurement earth/ground connections.
- The result should ideally show an almost straight line around 0 dB.

An open circuit measurement

- In theory, this should yield a 0-response, indicating a minus infinity dB-response. However, all measurement systems entail internal noise, and the test leads may introduce some response from open clip ends.
- Disconnect the "Source"/"Reference" clip from the "Measure" clip. The clips themselves may influence readings at the highest frequencies. If the "Measure" coaxial cable from the FRAX unit is disconnected, the graph will reveal the noise in the measurement system.

Field test box, FTB-101

- FTB-101 serves as a field test box designed to verify the integrity of leads and equipment, as recommended by CIGRE and several other entities.
- Connect the "Source"/"Reference" clip to the left-hand side connector and the braid from the clip to the bottom connector. Attach the "Measure" clip to the right-hand side connector and the braid from the clip to the bottom connector. Additionally, connect the bottom connector to the ground/earth to mitigate interference at 50/60 Hz.
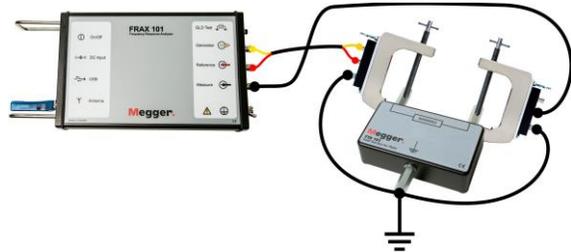
Figure 4.3: Connection for the field test box
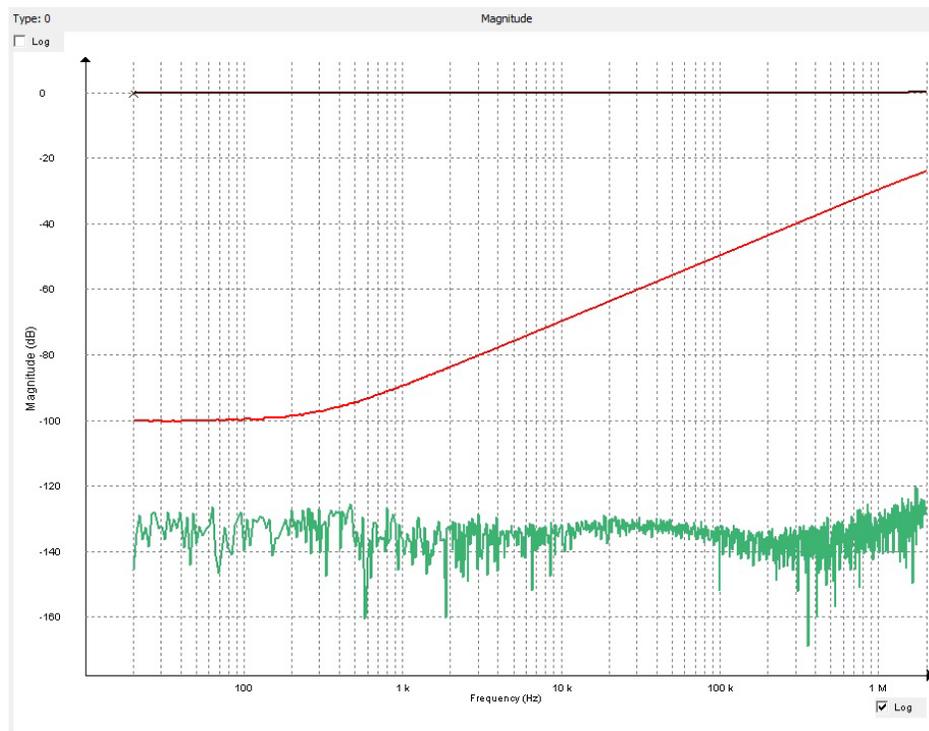
Figure 4.4: The results of the test measurements showing
-short circuit measurement (black),
-open circuit measurement (green),
-field box test measurement (red)

o   Preparation & Connections

To initiate the utilization of the FRAX analyzer, several essential connections must be established. These connections entail the FRAX instrument, two C-clamps, and suitable cables (BNC and ground).

Figure 4.5: C-clamps (left), ground braids (middle), and BNC connectors (right)

The FRAX clamp facilitates consistent connections, ensuring repeatable test outcomes. It accommodates both round and flat connectors and can be easily affixed to any bushing, such as those found on the testbench. Its secure grip enables heavy cables and accessories to be positioned near the bushing without the risk of detachment. Additionally, the clamp integrates all essential connectors (BNC, ground braid, cable strain relief) into a single unit. Maintaining the fixed position of the C-clamps and ensuring a consistent distance between them for every test is crucial, as any deviations could introduce potential variations in the measurements.
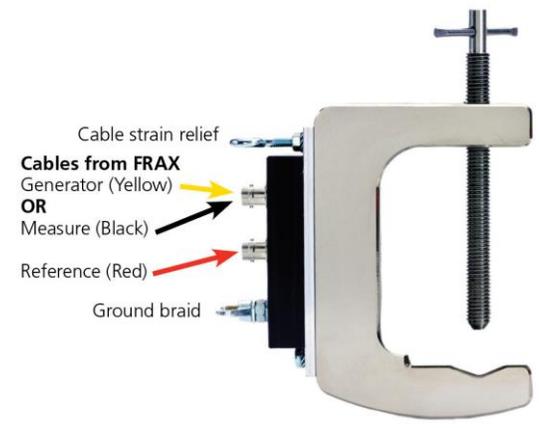
Figure 4.6: C-clamp

More specifically the following steps must be followed:

1. Attach the test lead BNC connectors (Generator (yellow), Reference (red), and Measure (black)) along with the ground braid to the FRAX instrument.

Figure 4.7: FRAX front panel with input connections

2. Connect the red and yellow (generator and reference) connectors to the clamp positioned at the top of one bushing, and attach the corresponding ground braid to the base of the bushing, ensuring it does not come into contact with any conducting part at the top of the bushing.

3. Connect the black (measure) lead to the clamp located at the top of the other bushing, and connect the corresponding ground braid to the base of the bushing, ensuring it does not touch any conducting part at the top.
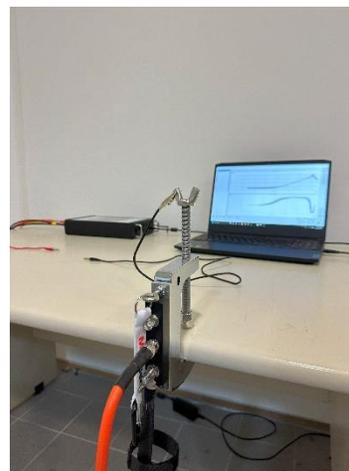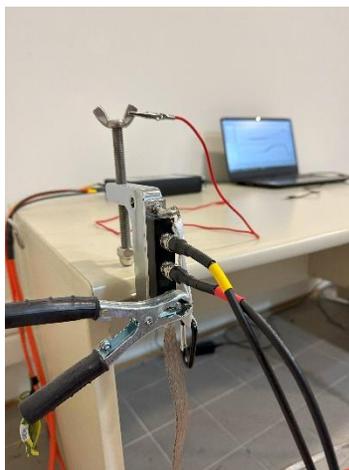
Figure 4.8: The two C-clamps used and their connections

4. Establish a connection between the AC/DC Adapter and the FRAX instrument, ensuring compliance with local safety regulations and the specifications of the AC/DC Adapter.
5. Connect the FRAX instrument to a computer via the USB cable.
6. Next, the cables extending from the top of each C-clamp (red and black) will be linked to the pole to initiate the measurements. The FRAX instrument can now be turned on.
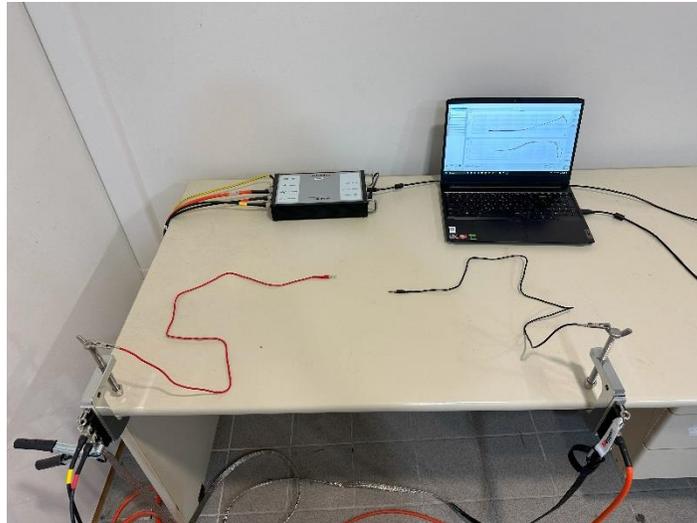
Figure 4.9: The whole testbench

o Establish Communication

1. Open the FRAX software, a requisite tool for utilizing the designated instrument. This software can be installed either through a disk provided with the instrument or via the Megger website.
2. Establish a connection to FRAX by navigating to the "Connect" option in the "File" menu, clicking the "Connect" button located on the right side of the software window, or pressing the F7 key. Successful connection setup will be indicated by the window name changing from "FRAX (Disconnected)" to "FRAX (Connected)". In the event of connection failure, an error message will prompt suggestions for resolution, typically involving selecting the suggested port number highlighted with a green symbol.

o   Create Test & Start Measurement

1. Utilize the "New File" command found in the "File" menu or press Ctrl+N to initiate a new file.

2. The "Measurement type" window will emerge. Within this window, select the tab under "Single Test".

3. Optionally input Nameplate information and click "OK". A "Save As..." dialog will prompt, allowing the selection of file structure and preferred name. By default, the directory will be set to My Documents\FRAX upon initial launch, subsequently reverting to the last used directory. The file name will adhere to the formatting set in the default filename settings. Click "Save" to preserve the file.

4. Execute the measurement by selecting a measurement from the Legend situated on the left side.

5. Commence the measurement by pressing the "Start" button or pressing the (F9) key.

6. Upon completion of the measurement, proceed to a new test by pressing the "Add Test" button or using Ctrl+A, then carry out the subsequent measurement.

o   Additional Settings

When conducting measurements on pole impedance, it's crucial to observe high frequencies where significant changes often occur. Therefore, the stop frequency should be configured to the highest feasible value, which is $2 \cdot 10^7$ Hz. This setting can be adjusted either in the "Measurement Setting" within the "Configuration" drop-down menu, or each time a new test is initiated through the corresponding window. It's important to note that these band settings are not the default ones and must be applied using the "Set band" button.
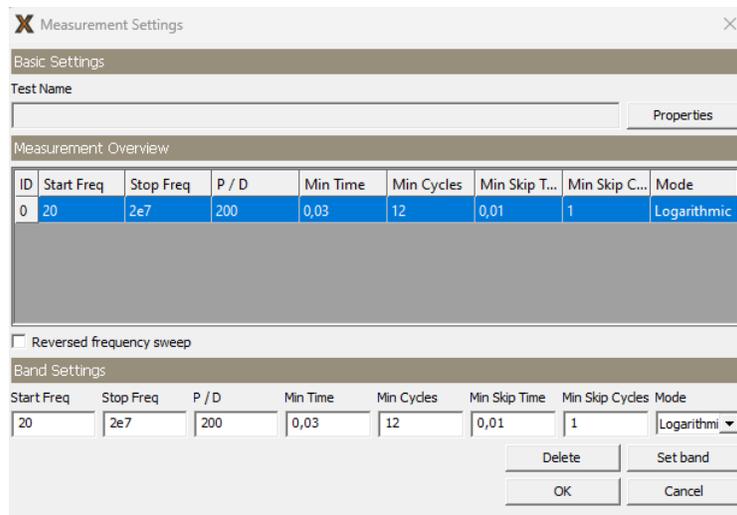
Figure 4.10: Measurements Settings

SFRA analysis provides both magnitude response and impedance/admittance. The magnitude response (in dB) is well-established and standardized, with most published results presented in dB. Conversely, impedance (in Ω) is more commonly understood in engineering circles, particularly among power engineers familiar with impedance in ohms, and offers enhanced resolution for low-impedance circuits. Additionally, impedance representation enables discrimination between resistive and inductive components.

dB-scale

- Magnitude = 20*log(Meas/Ref)
- Phase = Phase (Meas/Ref)

Impedance scale (Admittance Y = 1/Z)

- |Z| = |U/I| = 50*(Ref – Meas)/Meas
- Phase = Phase (Z)

In this project focused on impedance spectroscopy of poles, utilizing the impedance scale is essential. Therefore, it's imperative to incorporate both the Impedance Model and the Impedance and Phase Graph Views. These can be added through the "Models" and "Graph Views" options, respectively, in the "Configuration" drop-down menu.
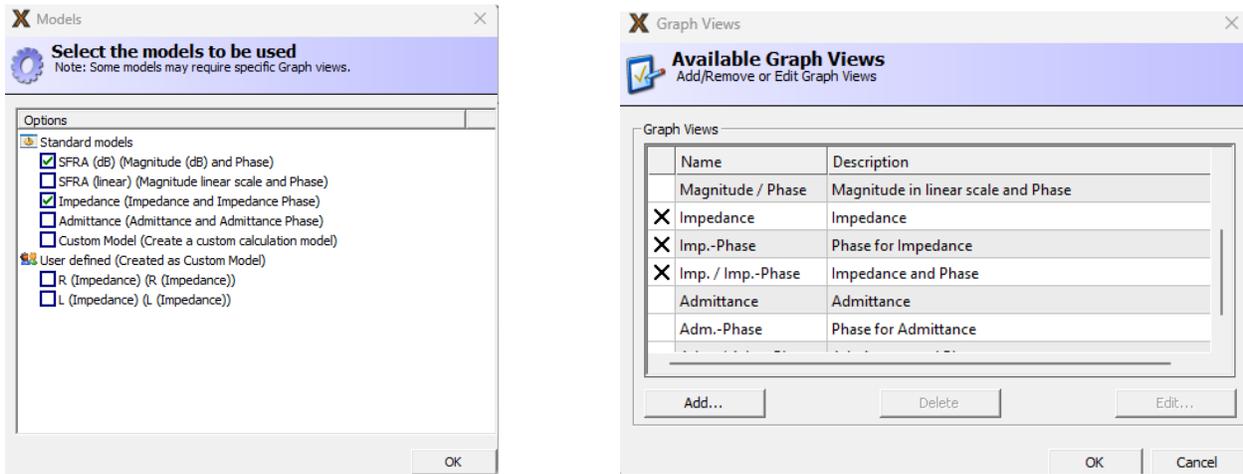
Figure 4.11: Models & graph views

The FRAX software main window is displayed below, showing all areas of interest.
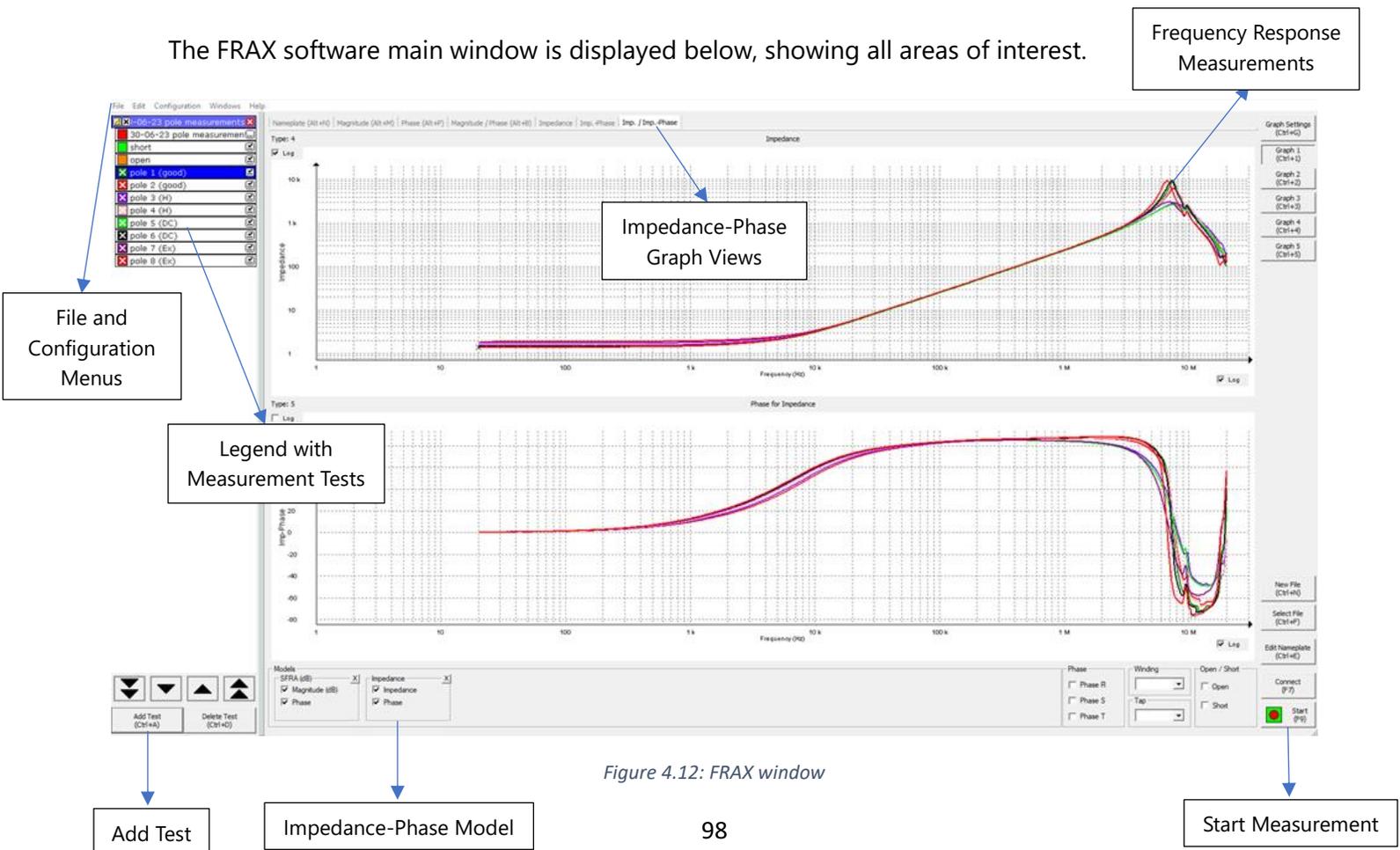
Figure 4.12: FRAX window

98

o   Tests Conducted

As previously mentioned, three tests were conducted utilizing the FRAX analyzer. These included measurement of the overall pole impedance, calculation of the capacitance between the coil and the core, and assessment of insulation capacitance between turns. These tests were conducted both at the project's outset and during degradation testing. The procedure and connection between the FRAX instrument and the C-clamps remained consistent across all tests, as detailed in the preceding section. Only the location to which the analyzer terminals were connected varied. Unfortunately, visual depictions of the poles cannot be provided due to the poles being customer components. These tests are part of the performed work and will be also presented as part of the next chapter.

Pole impedance spectroscopy

The procedure for whole pole impedance spectroscopy is straightforward. The ends of the pole, stripped of thin film insulation, serve as contact points for the impedance spectroscopy electrodes.

Capacitance between coil and core

For measuring the capacitance between the coil and the core, the coil is housed within a 3D-printed box. The box features a conducting bottom on which the pole is positioned, establishing a galvanic connection. An electrode is also provided outside the box. Consequently, the impedance analyzer's terminals are connected to the conductor in contact with the pole and one of the winding's terminals.
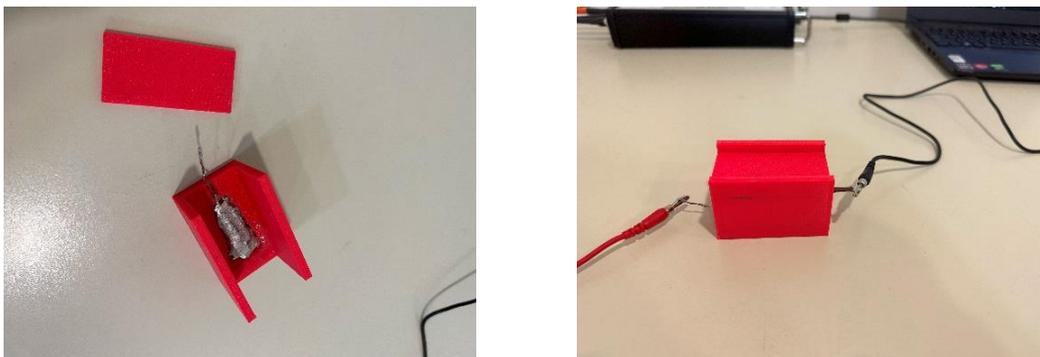

Figure 4.13: Capacitance between coil and core measurement

Insulation capacitance between turns

To assess turn-to-turn capacitance, a custom casing was constructed through 3D printing. This casing comprises two parallel racks designed to accommodate the copper bars. When arranged perpendicular to each other, the two parts facilitate the crossing of two copper bars, thereby enabling their interconnection for dielectric testing.
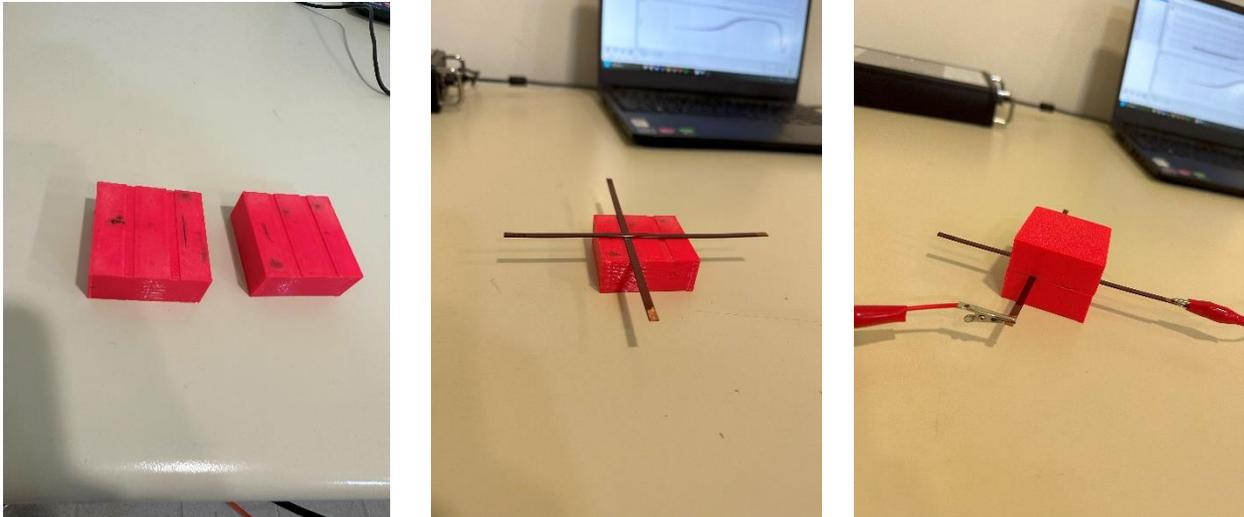

Figure 4.14: Insulation capacitance between turns measurement

o   Export Measurements

Finally, the chosen measurements (those marked with a cross symbol in the legend) can be exported for further analysis and processing using Matlab at a later stage. To do so, navigate to the "Export" option in the "File" drop-down menu. Several export options are available, but CSV was chosen for its compatibility with Matlab software.

5) PERFORMED WORK

The actions undertaken in the TEAMstress project, outlined in the subsequent chapter, focus on comprehending the deterioration processes of insulating materials in poles, used in Permanent Magnet Synchronous Traction Motors (exploiting the YASA topology and the axial flux pathing between two external rotors and an internal stator), developing quality testing procedures, designing models, and conducting analyses. The following section briefly presents most of the parts that were studied, and the tests conducted during the project, but mainly focuses on the thermal cycling stress.

5.1 Pole Model Development

Numerous models in the literature attempt to characterize coil behavior, but many lack the complexity and accuracy required for this project's objectives [133]-[139]. Consequently, the circuit chosen incorporates numerous parameters from both the coil and pole, along with additional factors influenced by the equipment used in measurements. The stator pole, including its armature winding, the selected pole model, and all associated circuit parameters, are detailed below (only a designed structure of the pole is presented, as the pole itself cannot be depicted due to the poles being customer components. Poles typically consist of a core encased in a Nomex layer, with the coil situated externally. The entire assembly undergoes impregnation. These parameters were gathered through statistical experimental testing conducted on 95 poles and 10 copper bars within the winding, utilizing spectroscopy and a high-voltage megohmmeter. The developed model can be used for quality inspection, fault prognosis, and fault diagnosis purposes. A variance of the model's parameters can produce unique patterns using impedance spectroscopy, thus allowing the identification of a fault or a manufacturing issue.
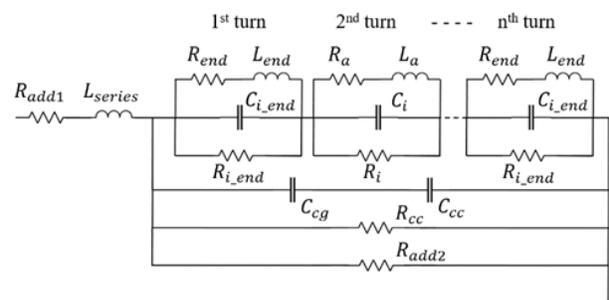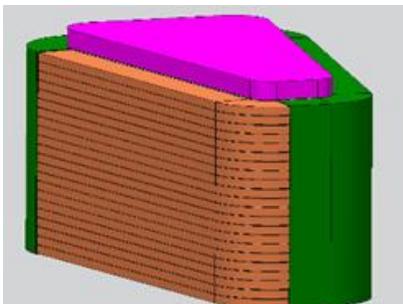

Figure 5.1: Stator pole and its mounted armature winding   Figure 5.2: Equivalent circuit of pole and mounted coil when subjected to impedance spectroscopy

Table 5.1: Equivalent circuit parameters index

R_{add_1}	Additional resistance due to the circuit wiring
L_{series}	In-series inductance due to the instrument augmented by 1 turn's inductance
R_{end}	Internal turn resistance of the first and last turns of the coil
L_{end}	Inductance of the first and last turns of the coil
C_{i_end}	Capacitance between the 1st and 2nd turn of the coil
R_{i_end}	Insulation resistance between the 1st and 2nd turn of the coil
R_a	Internal turn resistance
L_a	Single turn inductance
C_i	Capacitance between two turns of the coil
R_i	Insulation resistance between two turns of the coil
C_{cg}	Added capacitance aiming to measurement correction
C_{cc}	Capacitance between the core and coil
R_{cc}	Insulation resistance between the core and coil
R_{add2}	Shunt resistance of the impedance spectroscopy

The turns exhibit a certain degree of asymmetry in their modeling. All coil turns, except for the first and last ones, share identical properties (R_a, L_a, C_i, R_i). However, the first and last turns differ in properties due to capacitance fringing and coil end effects. Additionally, the surface areas of the first and last turns are smaller compared to those of the inner coil turns. L_{series} represents a parasitic inductance arising from the impedance spectroscopy instrument, augmented by the inductance of one additional turn. This additional turn comprises the combined inductances of the two halves of the first and last turns, which are not linked by capacitance to the second and second-to-last turns of the coil. Further explanation of the parameters is provided later in the text.

o   Internal Coil Resistance

The coil's internal resistance was determined using an ohmmeter. However, considering the spectroscopy's high-frequency range, the skin effect must be accounted for [140]. Consequently, the resistance was computed for each frequency increment, as illustrated below. In the equations, l represents the length, σ denotes conductivity, ρ stands for resistivity, w signifies width, t indicates thickness, δ represents the skin effect depth $\left(\delta = \frac{1}{\sqrt{\pi f \mu \sigma}}\right)$, and the critical frequency for the skin effect is defined as: $f_{se} = \frac{4}{\pi \mu \sigma}\left(\frac{w \cdot t}{w+t}\right)^2$.

$$R_{LF} \approx R_{DC}$$

$$R_{HF} \approx \frac{l}{2 \cdot \sigma \cdot (w + t) \cdot \delta}$$
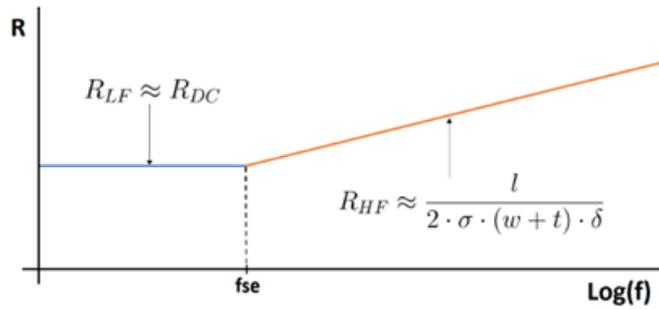
Figure 5.3: Modeling the skin effect's impact in the internal resistance of the coil

o   Coil Inductance

The coil's inductance was determined through frequency response analysis. As the frequency increases, starting from 10^4 Hz, the coil's inductance begins to dominate, and the phase gradually approaches 90°. To ensure precision, the maximum angle (approximately 90°) was identified, occurring at a frequency of 1.977 MHz, indicated by arrows in the figure on the right. Subsequently, the impedance value at this frequency was extracted, representing the total coil impedance. This value was then divided by the total number of turns and incorporated into the model.
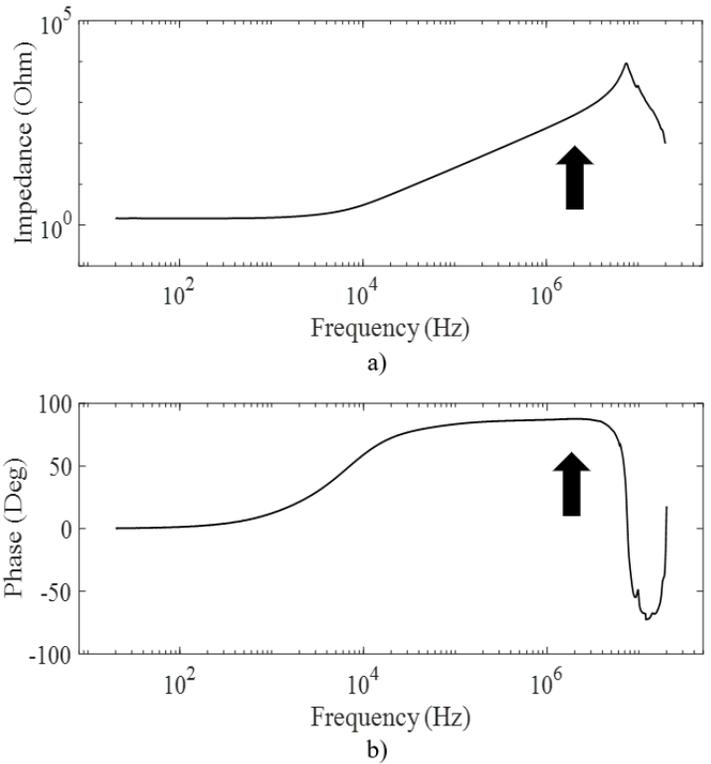
Figure 5.4: Impedance spectroscopy of the coil where:
a) the impedance and
b) the phase versus the frequency

Ninety-five poles were measured to provide robust statistical data. The measured inductances and the corresponding statistical analysis are detailed below. The vast majority of the poles exhibit minimal variation, with an average inductance of 37.9 µH.

Table 5.2: Coil inductance ranges and distributions

Limits (µH)	Number of Points
37.2-37.48	3
37.48-37.76	3
37.76-38.04	30
38.04-38.32	31
38.32-38.6	18
38.6-38.88	4
38.88-39.16	1
39.16-39.44	3
39.44-39.72	1
39.72-40	1
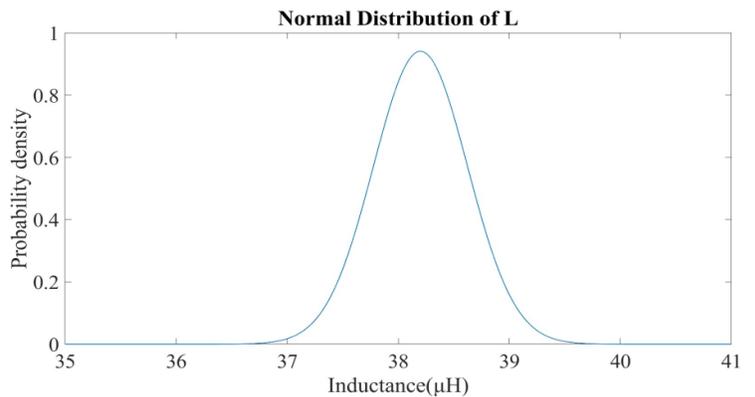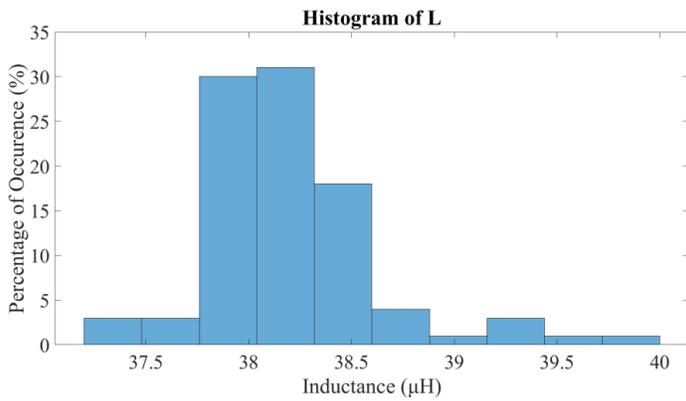
Figure 5.5: Histogram and normal distribution of the measured pole inductance

o   Insulation Capacitance between turns

To assess the capacitance between the coil turns, a sample consisting of 10 copper bars, each insulated with thin-film material and sourced from the same coil wire, was employed.

The process unfolds as follows: two bars are inserted into separate ducts within a custom-made enclosure. These bars are oriented perpendicular to each other, creating a square contact area between them due to their equal width. This arrangement enables vertical movement of the first bar and horizontal movement of the second, facilitating multiple contact points between them. The ends of the bars have been stripped of their thin film insulation and serve as electrical contact points for the impedance spectroscopy electrodes.
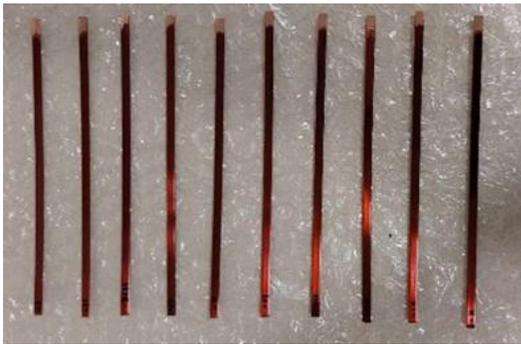

Figure 5.6: The copper wire samples
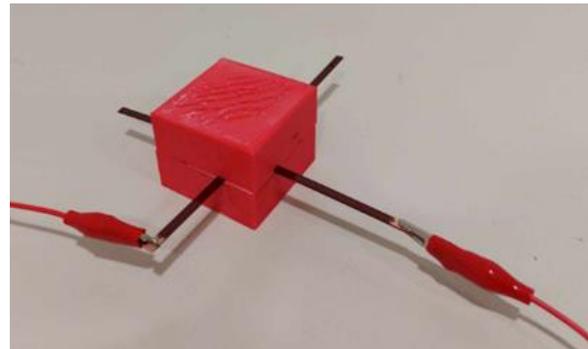
Figure 5.7: Setup for measuring the insulation capacitance between turns

Firstly, the results of the impedance spectroscopy are displayed. A total of 80 measurements were conducted to enable thorough statistical analysis. From these measurements, the minimum angle was identified along with its frequency of occurrence. The chosen frequency was approximately 80 kHz, with angles consistently exceeding 89.8° across all samples. Subsequently, the capacitance of the tested points was determined, with the values categorized and presented in the table below. Additionally, histograms illustrating these values alongside the calculated normal distribution are provided in the subsequent figures. The average capacitance value, C_{mean}, is calculated to be 5.1723 pF. However, the minimum capacitance value, C_{min}, at 4.1262 pF, is 20.2% lower than the average, while the maximum, C_{max}, at 6.1355 pF, is 18.6% higher.

In this study, the mean capacitance value is utilized. However, before incorporating it into the model, adjustments are necessary to align with the correct surface area. Initially, the measured value is normalized according to the surface area. Subsequently, the mean length of one turn and the actual surface area of the turn are computed. Finally, the normalized capacitance is multiplied by the turn's surface area, yielding the value denoted as C_i, which is then integrated into the model.
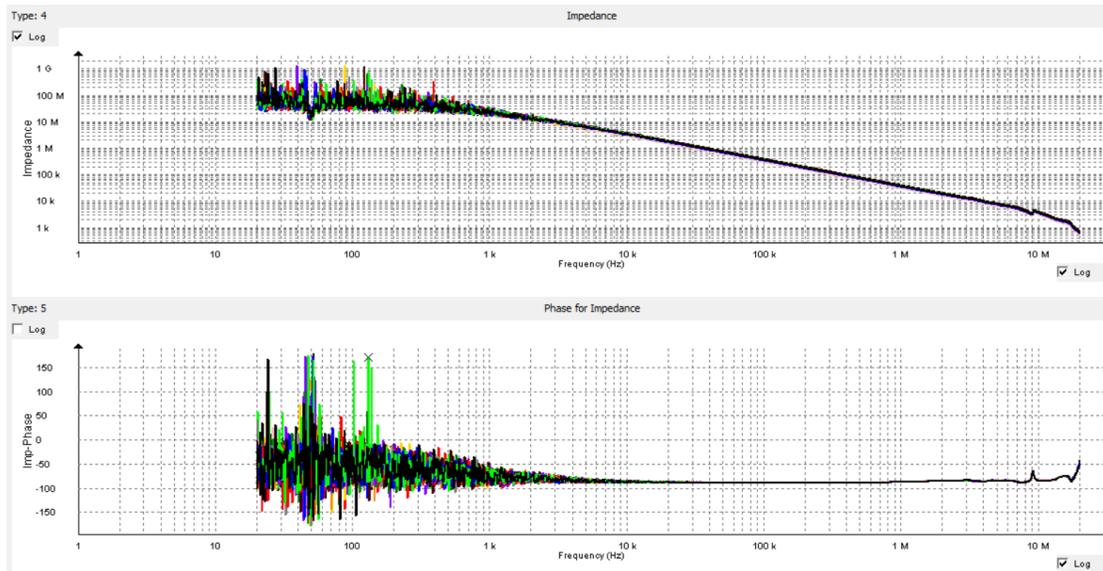

Figure 5.8: Impedance spectroscopy of the contact area between couples of bars

Table 5.3: Capacitance values of the 80 area samples

| Limits (pF)	Number of Points
4.1-4.29	2
4.29-4.48	4
4.48-4.67	8
4.67-4.86	9
4.86-5.05	11
5.05-5.24	11
5.24-5.43	9
5.43-5.62	7
5.62-5.81	6
5.81-6.0	9
6.0-6.19	4
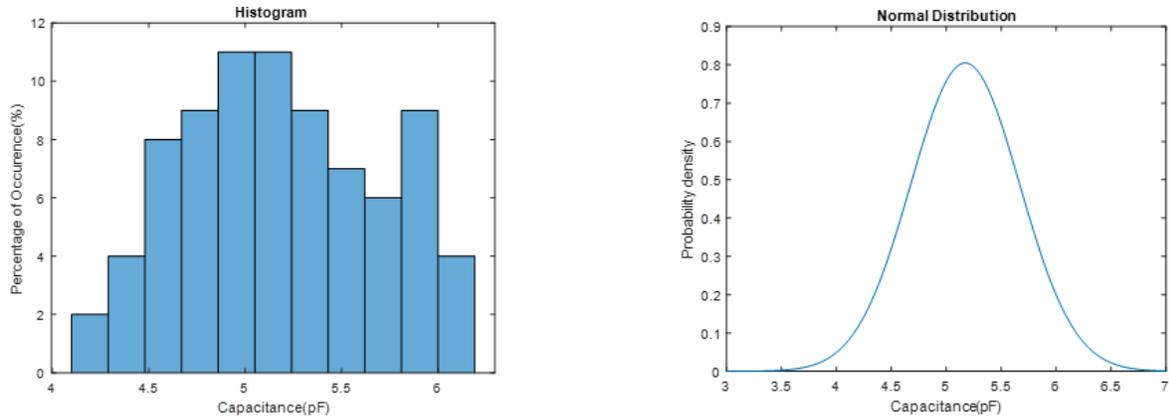
Figure 5.9: Histogram and normal distribution of the measured areas

o   Turn-to-turn Insulation Resistance

Initially, the 10 available copper bars are grouped into 5 pairs for simultaneous testing. Each pair is positioned inside a shielding case within two parallel ducts, with a copper thin plate placed atop, intersecting both bars. The ends of the copper bars are connected on one side and left open on the other. Using a 15 kV Megohmmeter, its electrodes are linked to the connected ends of the bars and the copper electrode. This configuration, depicted in the figure below, is employed because the resistance reaches extremely high values, beyond the instrument's recording capability. Consequently, this setup enables the measurement of two insulation areas in parallel, with their combined result recorded by the instrument.

Figure 5.10: The Megger MIT1525 15kV Insulation Tester

Each sample is subjected to 5 kV for 8 minutes until the measurement stabilizes. By adjusting the position of the copper plate, three distinct locations on the bars can be measured. This process generates a statistically significant dataset, from which the average is extracted for integration into the model.
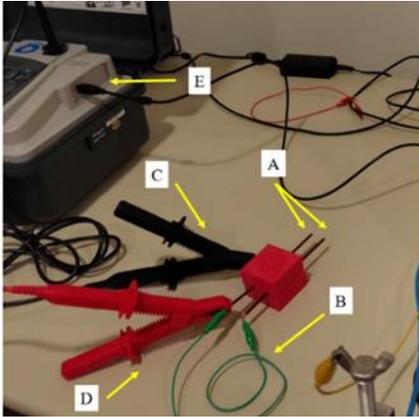
Figure 5.11: Setup for measuring the insulation resistance where:
A) the two copper bars
B) the short circuit at one end of the bars
C) electrode connected to the copper plate on top of the bars
D) electrode connected to the shorted end of the bars
E) the Megohmmeter producing high voltage
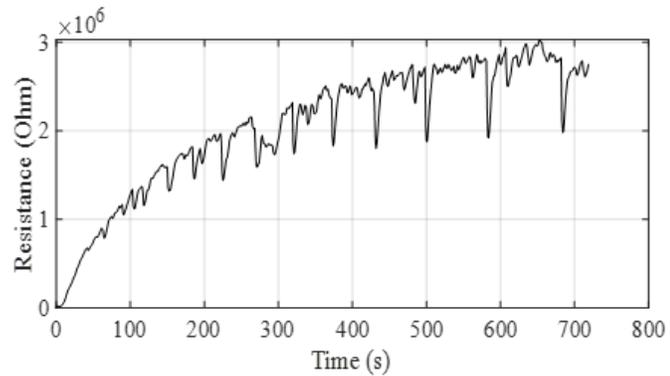
Figure 5.12: Typical measurement of the insulation resistance at 5kV for 8 minutes

o   Insulation Parameters between Coil and Core

The poles are positioned atop a copper plate, ensuring perfect conductivity with the pole surface (see Chapter 4, capacitance between coil and core pictures). To measure the capacitance C_{CC}, one electrode of the analyzer links to one terminal of the coil, while the other connects to the copper plate. The impedance and phase spectra are illustrated in the subsequent figure, with capacitance extracted at a phase angle of -90°. For resistance R_{CC}, the Megohmmeter electrodes are connected similarly, but the measurement lasts 12 minutes to nullify capacitive and charge currents. Statistical analysis conducted over 95 samples is presented below, revealing an average capacitance between coil and core of 0.11 nF, and a corresponding resistance of 2.29 TΩ.
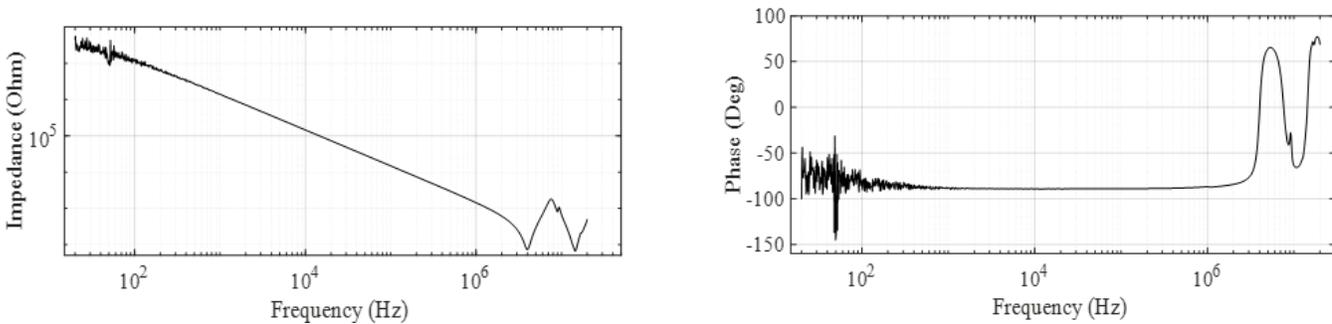

Figure 5.13: Impedance spectroscopy of the insulation between the coil and the core, where: a) the impedance and b) the phase

Capacitance C_{CC}

Table 5.4: Coil-to-pole capacitance ranges and distributions

Capacitance (pF)	Number of Points
10-25	3
70-85	5
85-100	13
100-115	27
115-130	20
130-145	6
145-160	13
160-175	2

Resistance R_{CC}

Table 5.5: Coil-to-pole resistance ranges and distributions

Resistance (TΩ)	Number of Points
0-0.45	6
0.45-0.9	5
0.9-1.35	9
1.35-1.8	14
1.8-2.25	12
2.25-2.7	13
2.7-3.15	13
3.15-3.6	7
3.6-4.05	6
4.05-4.5	4
4.5-4.95	6
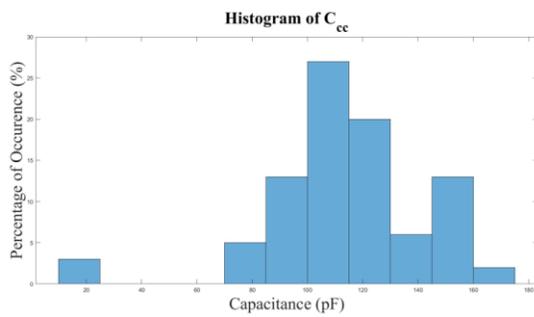
*Figure 5.14: Histogram of coil-to-pole capacitance and resistance*
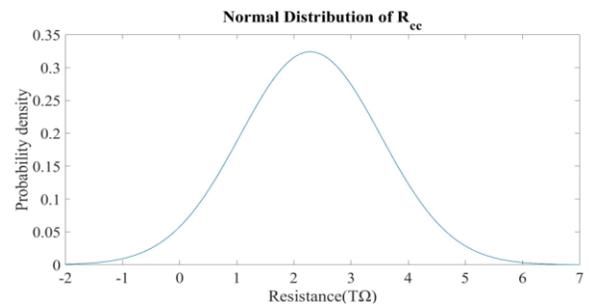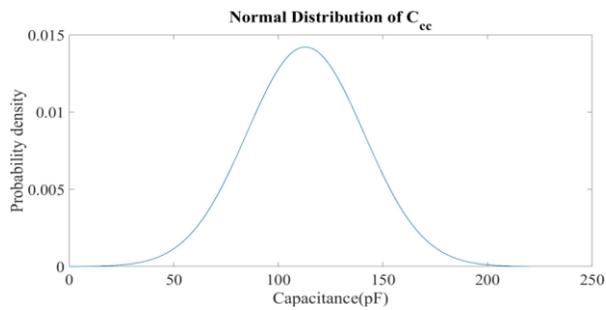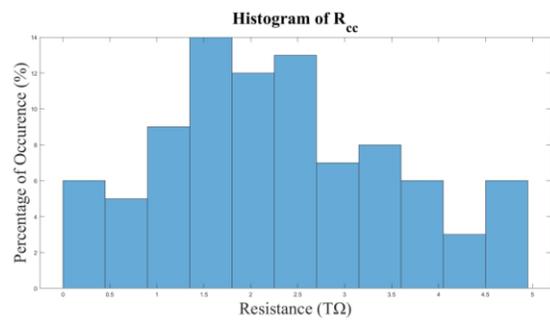
Figure 5.15: Normal distribution of coil-to-pole capacitance and resistance

o   Introducing Additional Parameters

At this stage, an initial model of the pole can be formulated using the physical quantities measured and outlined in the preceding sections. Assuming uniform parameters across all turns (excluding end or fringing effects) and no inclusion of parasitic components, the spectroscopy results will yield the following outcome (presented alongside the experimentally measured pole for reference).
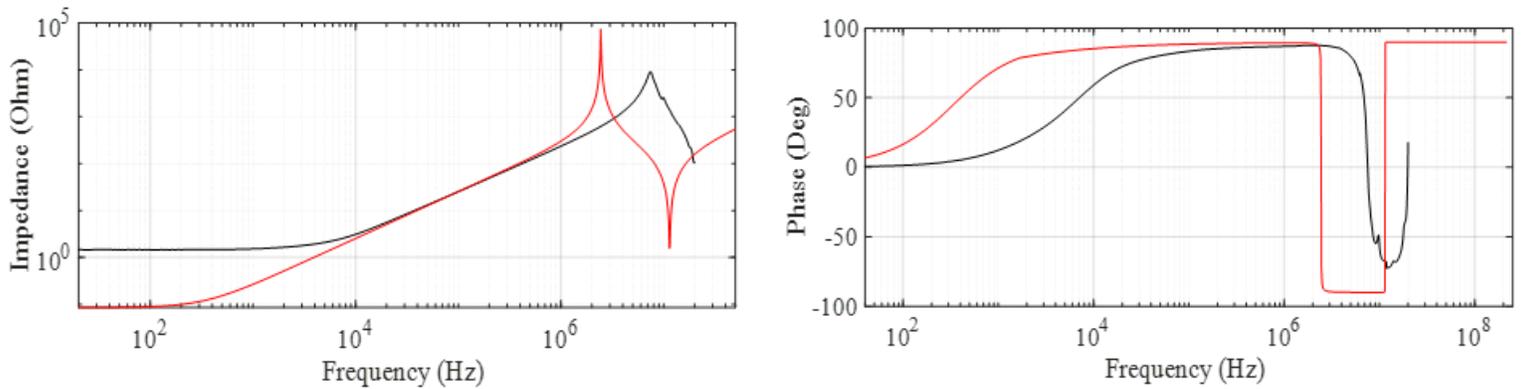

Figure 5.16: Impedance spectroscopy of the asymmetric model (red) and the experimentally measured pole (black) where: a) the impedance and b) the phase

The observed distinctions are as follows:

- There is a notable variance in the maximum amplitude of impedance.

- The frequency at which the maximum amplitude is reached differs.

- The DC impedance exhibits dissimilarity.

- A secondary, minor peak adjacent to the primary peak of the measured pole's impedance is absent in the model.

- The phase of the model exhibits a leftward shift, with its minimum being less than that of the measured data.

The initial and relatively straightforward issue to address is the discrepancy in DC impedance. This variance arises from the electrodes of the impedance analyzer and the supplementary wiring used to connect the poles. Through ohmmeter measurements, an additional resistance R_{add} of 1.37 Ω has been determined.

In the calibration process of the impedance analyzer via a short circuit test, an extra inductance equivalent to 2.09 µH, constituting the first component of the parameter L_{series}, was identified.

Additionally, adjustments are required for the capacitance of the first and last turns of the coil due to the fringing effect, which is particularly significant given the proximity of the copper bars and the fact that the electric field lines form from the sides of the bars and even the external surfaces of the first and last bars of the coil [141], [142]. The fringing k_f has been estimated using the following formula [143]:

➢ $$C = \frac{\varepsilon_0 \varepsilon_r w l}{g} + \frac{\pi \varepsilon_0 \varepsilon_r (l+w)}{\ln\left(\frac{\pi}{2}\left(1+\frac{g}{t}\right) + \sqrt{\frac{\pi^2}{4}\left(1+\frac{g}{t}\right)^2 - 1}\right)}$$

where: w and l represent the width and length of the capacitor plates respectively, while g denotes the distance between the plates and t indicates the thickness of the plates. Finally, it was decided that $k_f \cong 1.1$. Consequently, the insulation capacitance of the first and last turns is set as: $C_{i\_end} = k_f \cdot C_i$.

The parameter L_{end} is determined as $L_{end} = k_L \cdot L_a$, considering the incomplete turns formed by the first and last coils and the inductance's proportionality to the square of the number of turns. An estimate of k_L around 0.8 is derived.

Moreover, the impedance analyzer incorporates two 50 Ω SMD resistors in parallel at its input and output, which, in series with the ground cable, influence the total resistance connected in parallel to the coil during spectroscopy, primarily due to skin effect at high frequencies. The end-result is the reduction of the total resistance connected in parallel to the coil turns.

Finally, the last elusive parameter is C_{cg}, which has proven challenging to measure directly. Nonetheless, its estimation is straightforward as it solely governs the impedance spectra along the frequency axis. The introduction of all parameters, excluding C_{cg}, into the equivalent circuit elucidates the impedance and phase spectra shown in figure 5.17, compared to the experimental ones. Additionally, figure 5.18 illustrates the results from the comprehensive model against the experimental data. Close examination of these two figures reveals the shifting of the spectra attributable to the C_{cg} parameter. Furthermore, the developed equivalent circuit aptly describes the actual device with considerable accuracy. It's worth noting that the second spike to the right of the maximum impedance is a result of the coil's end effects. When $k_f = k_L = 1$, this second spike disappears entirely.
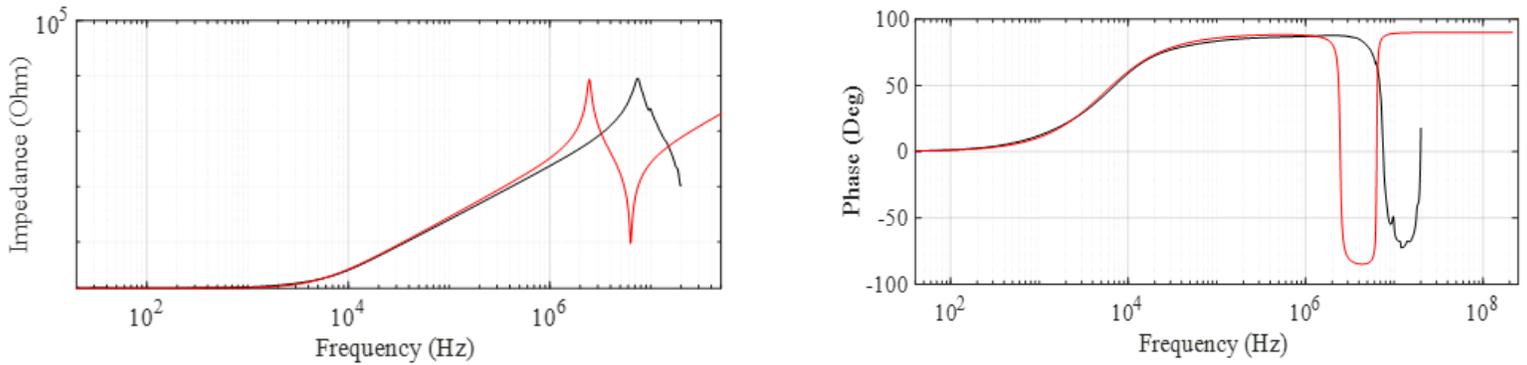

Figure 5.17: Impedance spectroscopy of the model without introducing Ccg (red) and the experimentally measured pole (black) where a) the impedance and b) the phase
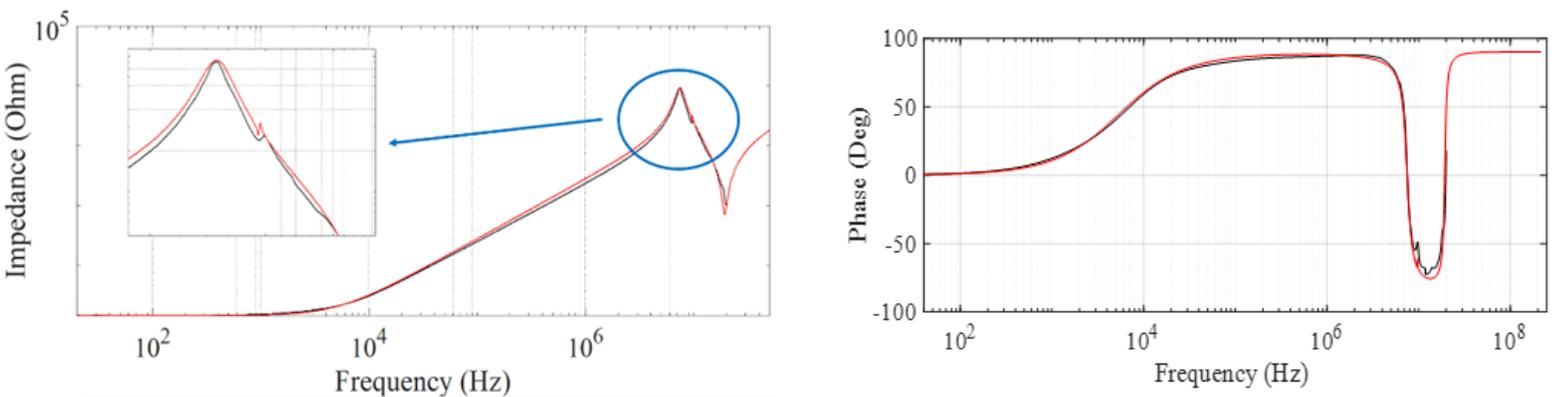

Figure 5.18: Impedance spectroscopy of the complete equivalent circuit model (red) and the experimentally measured pole (black) where a) the impedance and b) the phase

5.2 Thermal Cycling Stress

A thermal cycling test was conducted on the poles to simulate the temperature fluctuations experienced by insulating materials while the motor operates under varying loads, albeit with minimal variations. As mentioned previously, the poles under scrutiny in this project are sourced from Permanent Magnet Synchronous Traction Motors, underscoring the importance of the thermal cycling degradation test in monitoring insulation integrity. Additionally, thermal stress at a constant temperature was applied to eliminate the influence of thermomechanical effects present in thermal cycling stress, and the results were compared with those of the thermal cycling experiment. Both thermal degradation strategies were applied to two types of poles. While their geometrical characteristics are similar, poles from the first group are impregnated and henceforth referred to as Group A, while poles from the second group, lacking impregnation, are denoted as Group B.

Thermal Cycling Stress

Two sets of poles underwent thermal cycling degradation testing. Group A comprised 18 impregnated poles, while Group B consisted of 18 non-impregnated poles. Thermal cycling stress was applied passively using an oven to attain the desired temperatures. The poles under scrutiny were sourced from traction motors with an insulation class of 220 °C. Initially, the experiment aimed to push the cycles to the brink of this insulation class limit (220 °C). However, as negligible changes were observed, the temperature limits were subsequently increased to 240 °C for the final thermal cycles. The temperature ranges remained constant throughout each thermal cycle at 40 °C, with a cycle period of approximately 8 minutes, encompassing the time required for the temperature to ascend from the lower limit to the upper and back. Temperature sensors placed inside the oven monitored the temperature. The insulation condition of the poles was assessed during the thermal cycles using impedance spectroscopy results obtained via the FRAX analyzer and Nyquist plots, which are elaborated on in the following section. Additionally, breakdown voltage was recorded upon completion of all thermal cycles and compared to healthy values.

o   Group A

Group A comprises 18 impregnated poles, representative of the standard poles used in operational traction motors. A total of eight thermal cycles were conducted on these poles. The first six cycles lasted 6 hours each, with temperatures fluctuating between 180 and 220 °C. Subsequently, cycles 7 and 8 intensified in temperature, surpassing the 220 °C insulation class limit and reaching 250 °C; however, these cycles were shorter, lasting 3 hours each. Details of the stressing temperatures and durations are outlined in the table below.

Table 5.6: Stressing temperatures and durations of Group A poles undergoing thermal cycling

Poles of Group A		
Cycle	**Duration**	**Temperature Range**
C1	6 hours	180-220 °C
C2	6 hours	180-220 °C
C3	6 hours	180-220 °C
C4	6 hours	180-220 °C
C5	6 hours	180-220 °C
C6	6 hours	180-220 °C
C7	3 hours	210-250 °C
C8	3 hours	210-250 °C

The impedance spectroscopy figure, illustrating impedance and phase, captures the average behavior of all samples, as depicted below. The focus lies on high frequencies ($>10^6$ Hz), where both the primary and secondary spikes manifest. Alterations in amplitude or frequency shifts within these spikes may potentially occur, hence necessitating a figure displaying only high frequencies to unveil these changes with greater precision owing to thermal cycling stress. Notably, observed changes in low frequencies ($<10^4$ Hz) remain unaffected by thermal stress, stemming from the connection between the pole's terminals and the electrodes of the FRAX analyzer.
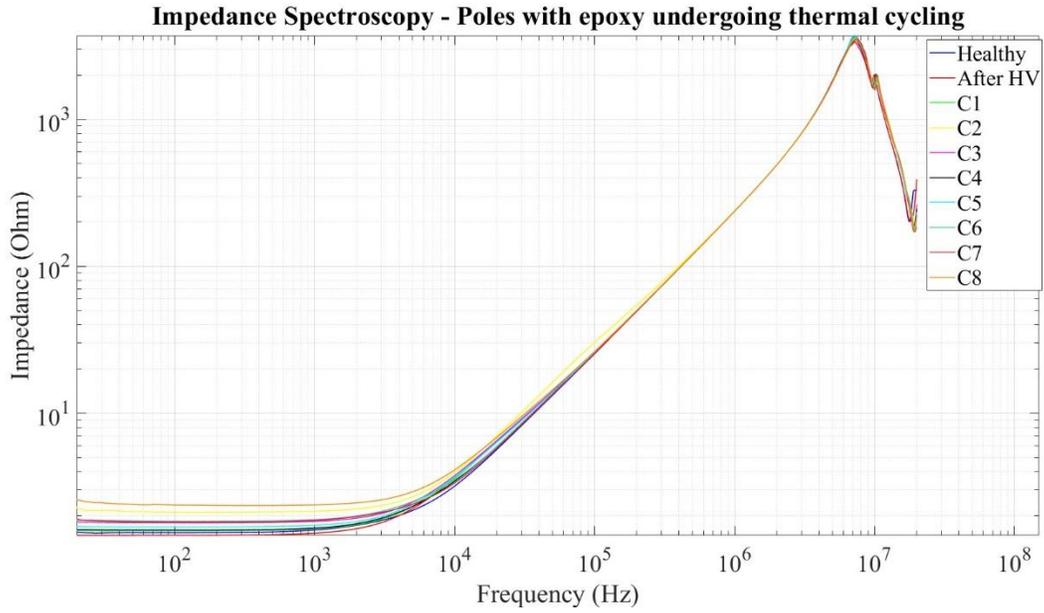
Figure 5.19: Impedance spectroscopy of Group A poles undergoing thermal cycling
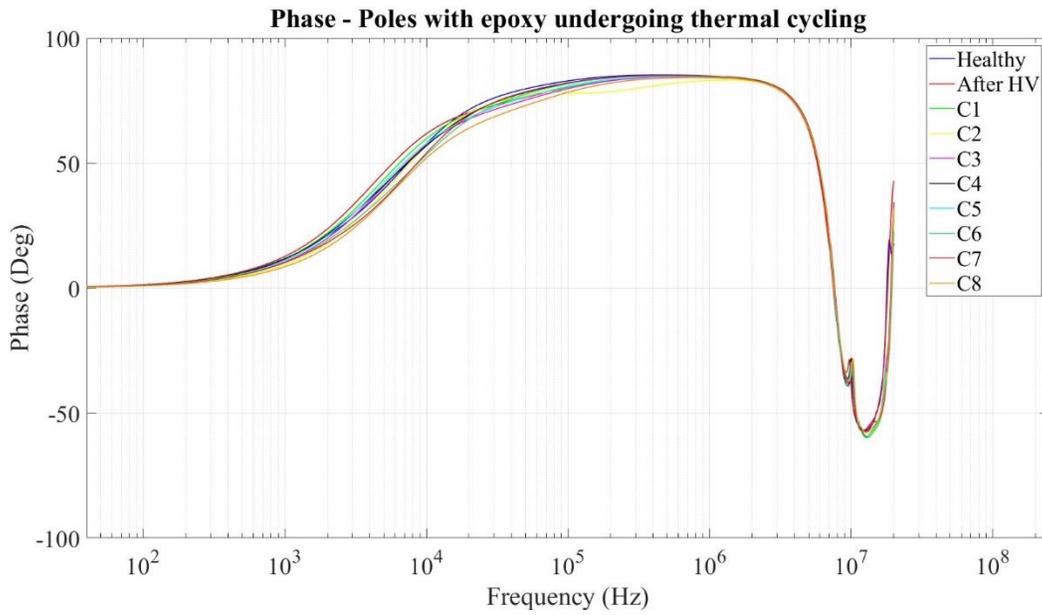

Figure 5.20: Phase of Group A poles undergoing thermal cycling

Before undergoing thermal cycles, all poles underwent an IR test (High Voltage), which slightly degraded the insulation, resulting in a decrease in impedance amplitude. Consequently, the Nyquist ellipsis exhibited a reduced radius, while the secondary impedance spike increased and shifted to the left compared to healthy poles.

Following the completion of the initial thermal cycle, there was a significant shift in results. The ellipsis expanded to its maximum size, impedance increased, and the secondary spike shifted to the right of the healthy one with higher amplitude. This outcome reflects chemical changes in the overall insulating system. Notably, the change in the secondary spike suggests a reduction in thin film capacitance, resulting in higher impedance.

Interestingly, the behavior of impedance spectra and Nyquist plots during accelerated aging is non-monotonic. The amplitude alternately increases or decreases after each cycle, yet the Nyquist ellipsis gradually returns to its original size. The primary indicator of change is the rightward shift and increased amplitude of the secondary spike compared to healthy poles.

This intricate behavior is attributed to chemical composition changes in the coexisting insulating materials (epoxy and thin film). Their electrical parameters exert opposing effects on total impedance. Aging reduces insulation resistance, leading to impedance reduction, while simultaneously decreases capacitance, increasing capacitive reactance, and consequently elevating impedance.
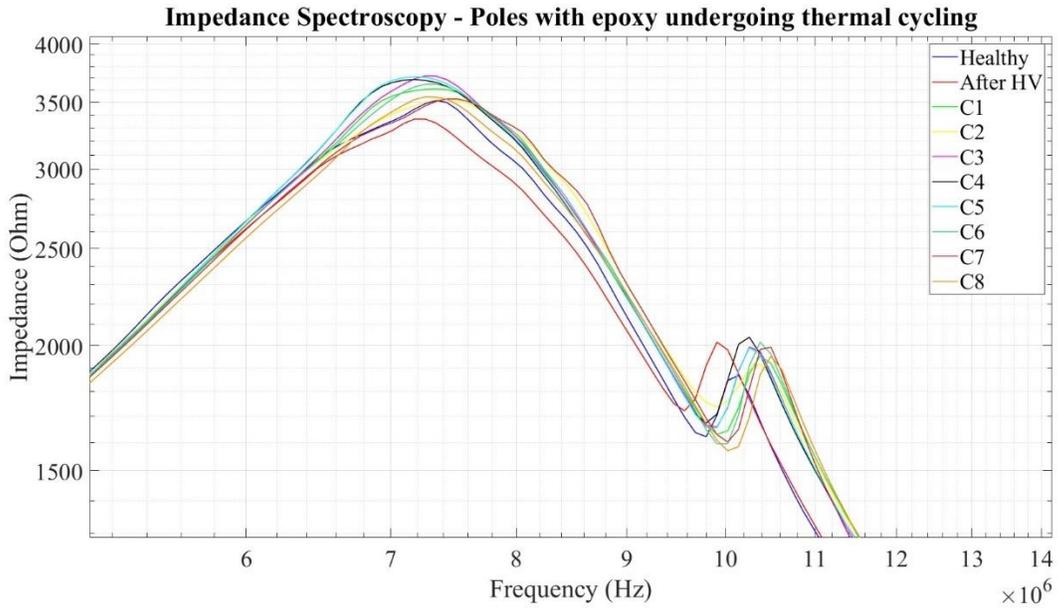
Figure 5.21: Impedance spectroscopy at high frequencies of Group A poles undergoing thermal cycling
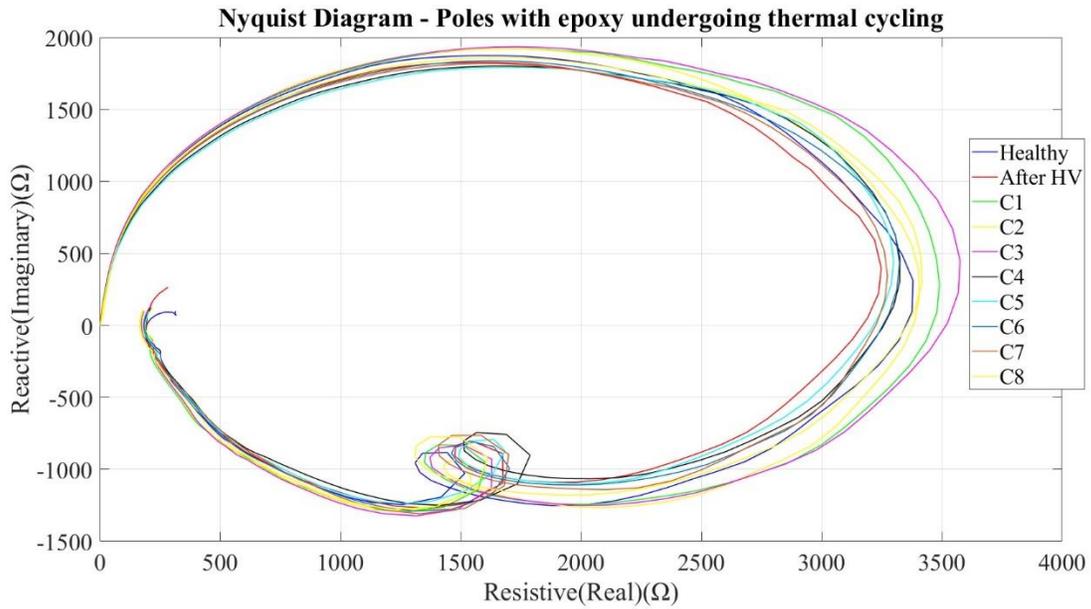

Figure 5.22: Nyquist diagram of Group A poles undergoing thermal cycling

- Group B

Group B consists of 18 non-impregnated poles, characterized by the absence of epoxy alongside the thin film insulation to secure the coil turns. Such poles are not utilized in practical traction motors and were exclusively scrutinized to explore the implications of epoxy absence. Four thermal cycles, each lasting 6 hours, were conducted, with temperatures gradually escalating with each cycle. Details regarding the stressing temperatures, durations, and corresponding results for Group B poles are provided below.

Table 5.7: Stressing temperatures and durations of Group B poles undergoing thermal cycling

| Poles of Group B		
Cycle	Duration	Temperature Range
C1	6 hours	180-220 °C
C2	6 hours	190-230 °C
C3	6 hours	200-240 °C
C4	6 hours	210-250 °C
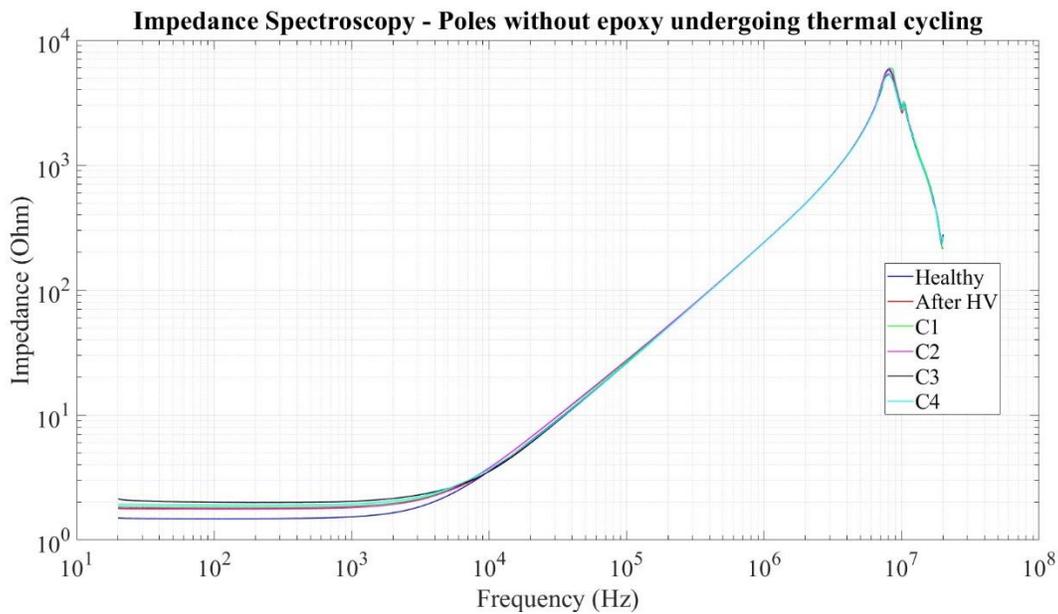
Figure 5.23: Impedance spectroscopy of Group B poles undergoing thermal cycling
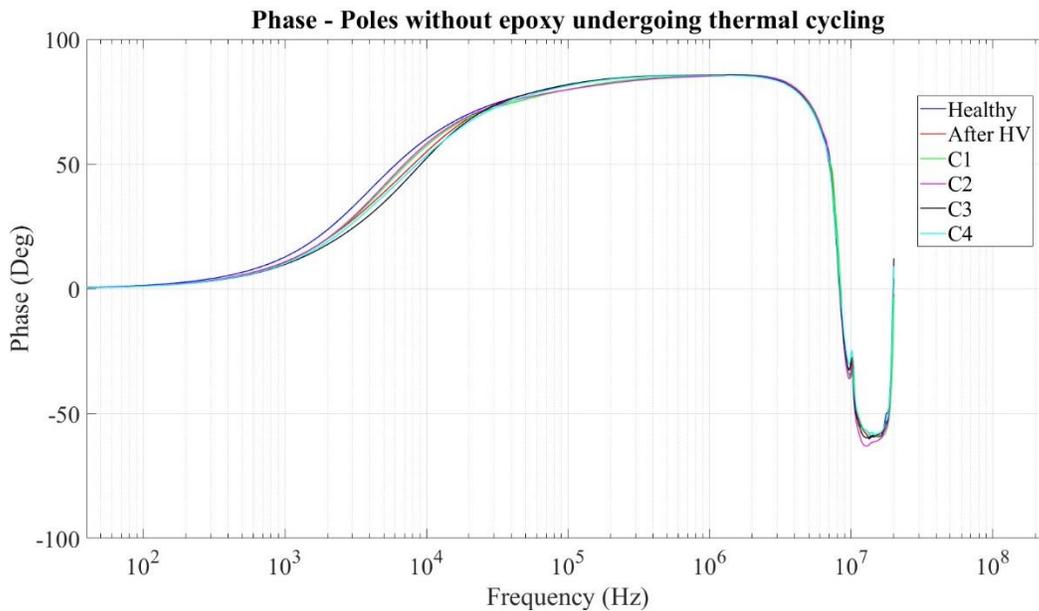
Figure 5.24: Phase of Group B poles undergoing thermal cycling

The impact of the IR test on Group B poles mirrors that of Group A, resulting in a reduction of impedance without any frequency axis shifting. Furthermore, upon subjecting the poles to the initial round of thermal cycling, impedance increases, indicating a reduction in insulation capacitance, a trend also observed in Group A. However, subsequent patterns diverge between the two groups. In Group B, impedance decreases with increasing aging time and stress. Additionally, Nyquist plots demonstrate a consistent reduction in ellipsis size with escalating thermal stress, suggesting a noteworthy observation. Specifically, when considering only thin film insulation (without epoxy), the thin film material experiences a rapid decline in capacitance, followed by a subsequent reduction in resistance at a faster rate than capacitance, ultimately resulting in a monotonic decrease in total coil impedance.
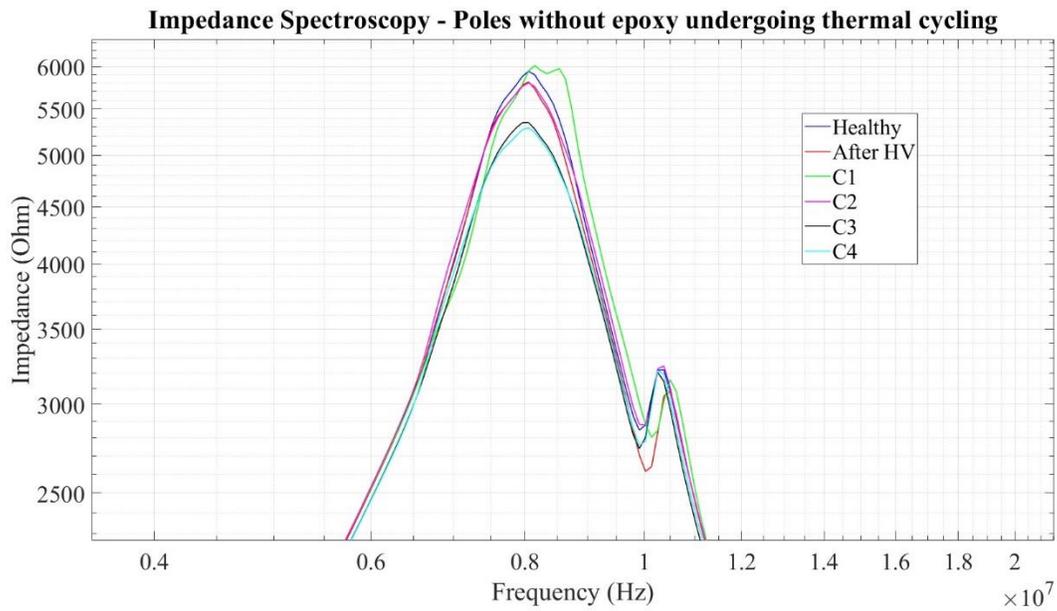
Figure 5.25: Impedance spectroscopy at high frequencies of Group B poles undergoing thermal cycling
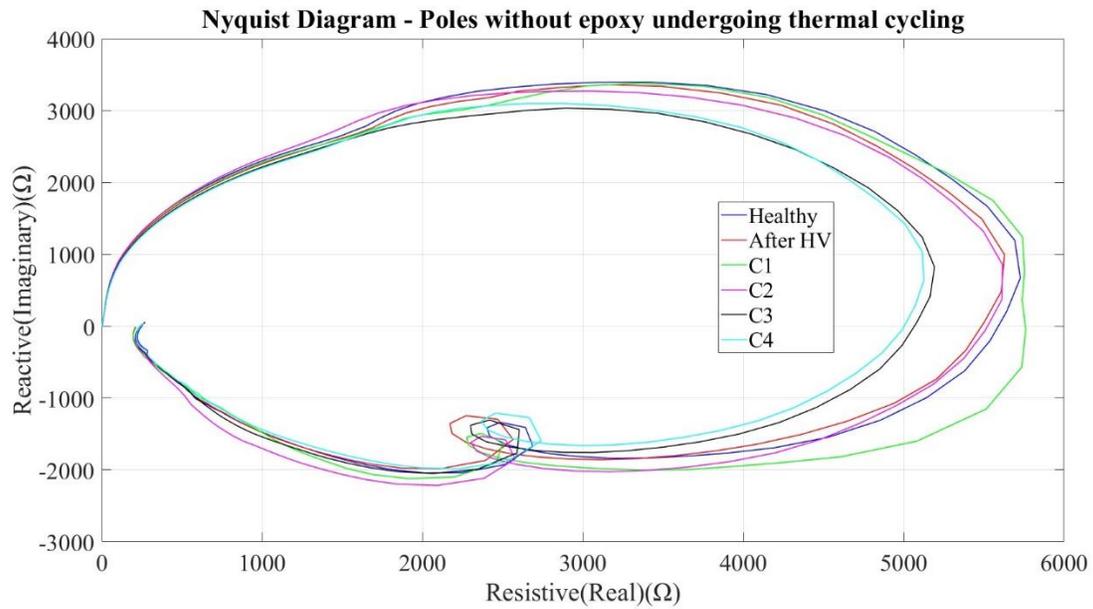

Figure 5.26: Nyquist diagram of Group B poles undergoing thermal cycling

o   Comparison of Groups A & B

The impedance spectroscopy at high frequencies and the Nyquist diagrams, encompassing average values of both impregnated and non-impregnated poles, are illustrated below to discern potential variations.

Upon closer examination of the figures, a notable disparity in pole impedance due to epoxy becomes apparent. The complex impedance of impregnated poles (Group A) is significantly lower than that of non-impregnated ones (Group B). According to the developed model, this divergence suggests that the additional resistance introduced by epoxy does not significantly influence total pole impedance. Thus, the resistance of the thin film already holds substantial prominence relative to other model parameters. If epoxy resistance were impactful, impedance would increase rather than decrease.

However, epoxy incorporation does augment capacitance within the model, resulting in a reduction of capacitive reactance and consequent diminution in Nyquist plot size. Additionally, the introduction of air between turns of non-impregnated poles, where coil turns remain unwelded by the absence of epoxy, reduces turn-to-turn capacitance, thereby elevating reactance and impedance.
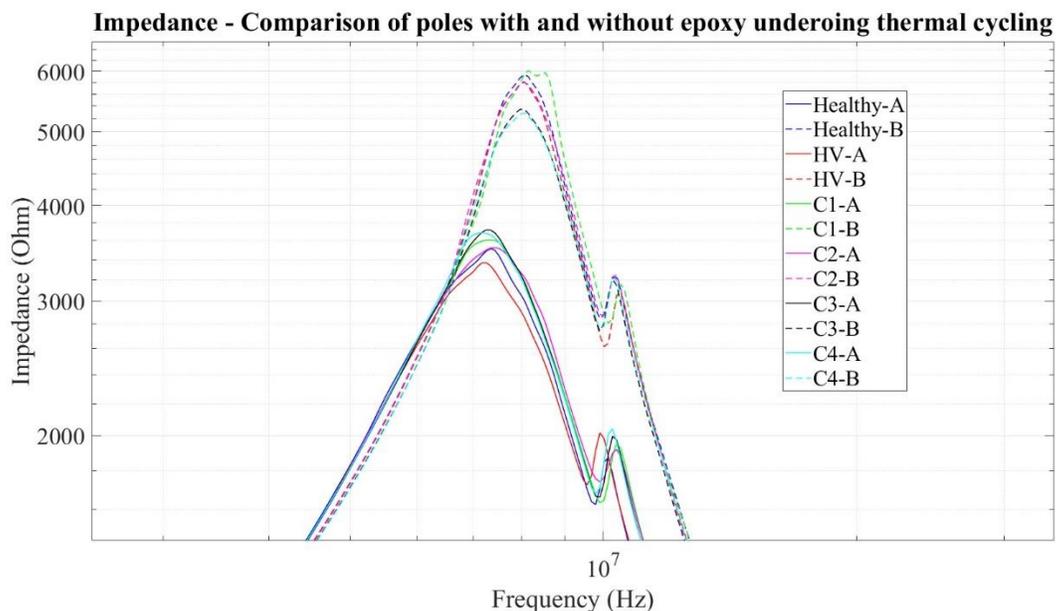

Figure 5.27: Impedance spectroscopy of both Groups compared undergoing thermal cycling
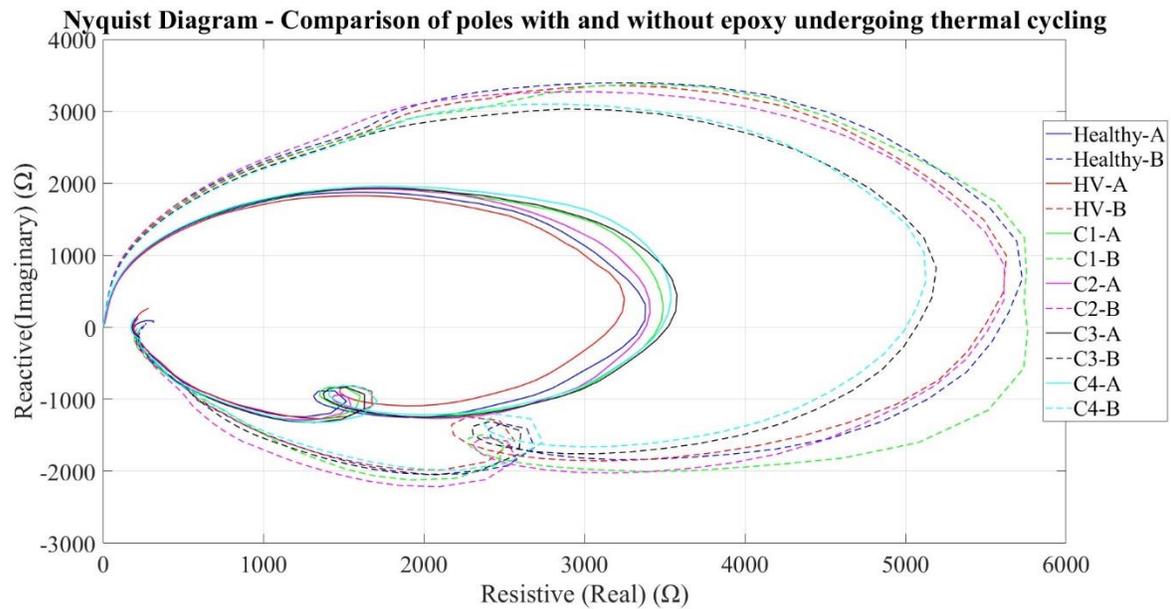
Figure 5.28: Nyquist diagram of both Groups compared undergoing thermal cycling

o   Breakdown Voltage Testing

After undergoing thermal cycling stress, Group A poles underwent early voltage breakdown tests utilizing a 15 kV Megohmmeter. Each pole had a copper bar affixed to its side, ensuring full contact with all turns. High-voltage electrodes were connected to one terminal of the coil and the outer copper bar, generating a high voltage difference to stress the insulation. Voltage increment was programmed in a ramp-like fashion. Upon nearing insulation breakdown, the instrument halted measurement to prevent sudden current surge, capturing the breakdown voltage. Initially, a subset of poles underwent solely the high voltage test to determine coil-to-pole resistance without additional stressors, were measured, serving as a reference for healthy poles.

The normal distribution, with average values and standard deviations, is depicted below in the accompanying table. Notably, thermal cycling stress emerges as a crucial factor in insulation degradation, evidenced by a 28.5% decrease in average breakdown voltage following 8 thermal cycles. Concurrently, the deviation increased by 19.8%.

Table 5.8: Average values and standard deviations of breakdown voltage

Normal Distributions Parameters		
Status	**Average Value (V)**	**Standard Deviation (V)**
Healthy	9.5466e+03	635.29
After 8 thermal cycles	6.8303e+03	761.14
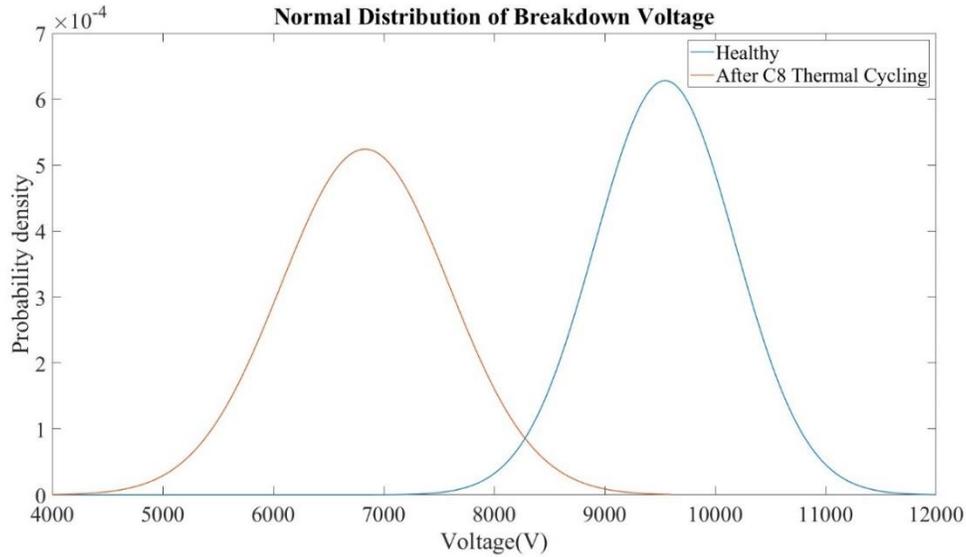
Figure 5.29: Normal distribution of breakdown voltage

✚ Fixed Thermal Stress

To gauge the specific degradation resulting from prolonged high-temperature operation, free from the confounding influence of thermomechanical effects inherent in thermal cycling stress, a series of fixed thermal stress cycles was devised. This experiment aimed to offer comparative insights alongside thermal cycling stress outcomes. In this instance, 6 poles from Group A (epoxy) and 6 poles from Group B (non-epoxy) were utilized concurrently and subjected to identical conditions within the same oven. The temperature was initially set at 200 °C for the inaugural cycle, progressively escalating to 240 °C across 7 cycles, once more surpassing the upper limit of the insulation class. The stressing temperatures and durations are delineated in the table below.

Poles of both groups		
Cycle	**Duration**	**Temperature**
C1	6 hours	200 °C
C2	6 hours	207.5 °C
C3	6 hours	215 °C
C4	6 hours	220 °C
C5	6 hours	225 °C
C6	6 hours	230 °C
C7	6 hours	240 °C

The impedance spectroscopy results, illustrating impedance and phase for both groups of poles, are presented below. Similar to the outcomes observed with thermal cycling stress, these results portray the collective behavior of all samples. Variations observed at low frequencies are attributed to the frequency response analyzer rather than thermal stress. Conversely, high frequencies are of paramount importance, as changes in amplitude and shifts in the main or secondary spike may occur. To facilitate a deeper understanding and comparison, impedance focusing on frequencies approximately $\approx 10^7$ Hz is provided alongside Nyquist diagrams. This allows for enhanced insight into the observed variations.

o   Group A – Impregnated Poles
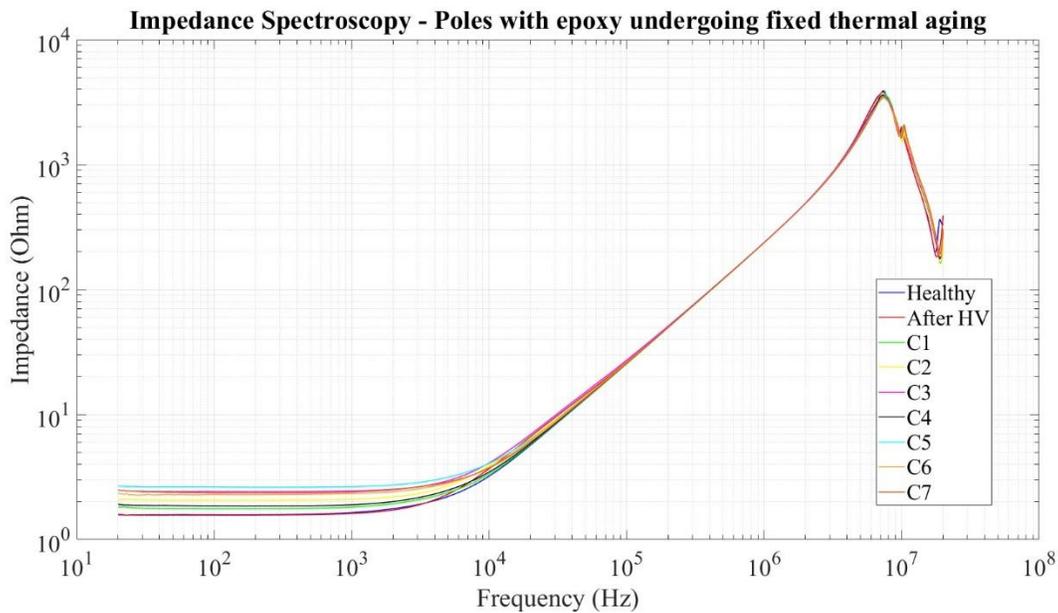
Figure 5.30: Impedance spectroscopy of Group A poles undergoing fixed thermal stress
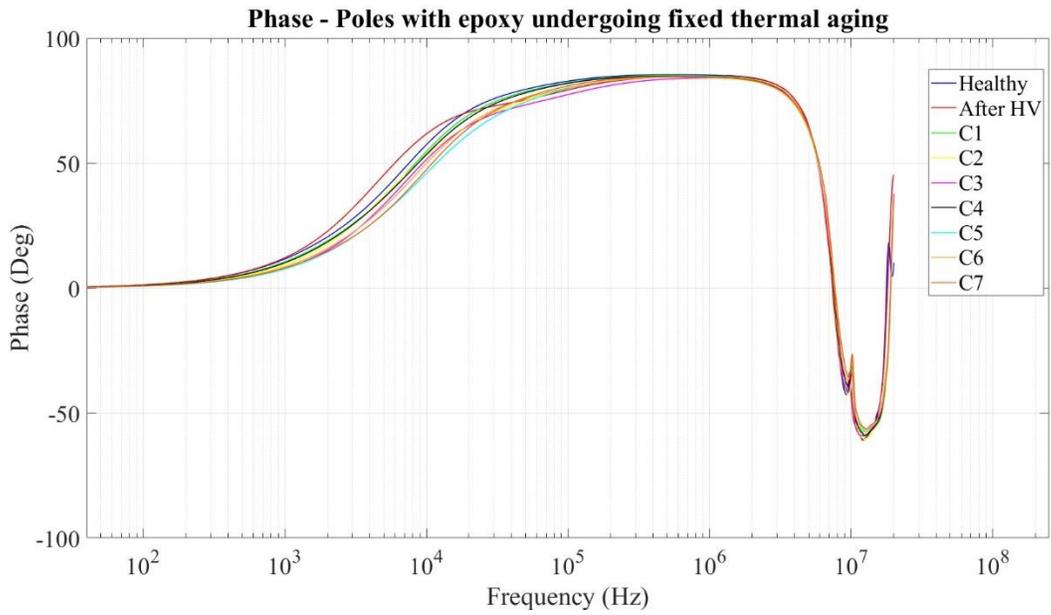
Figure 5.31: Phase of Group A poles undergoing fixed thermal stress

○ Group B – Non-impregnated Poles
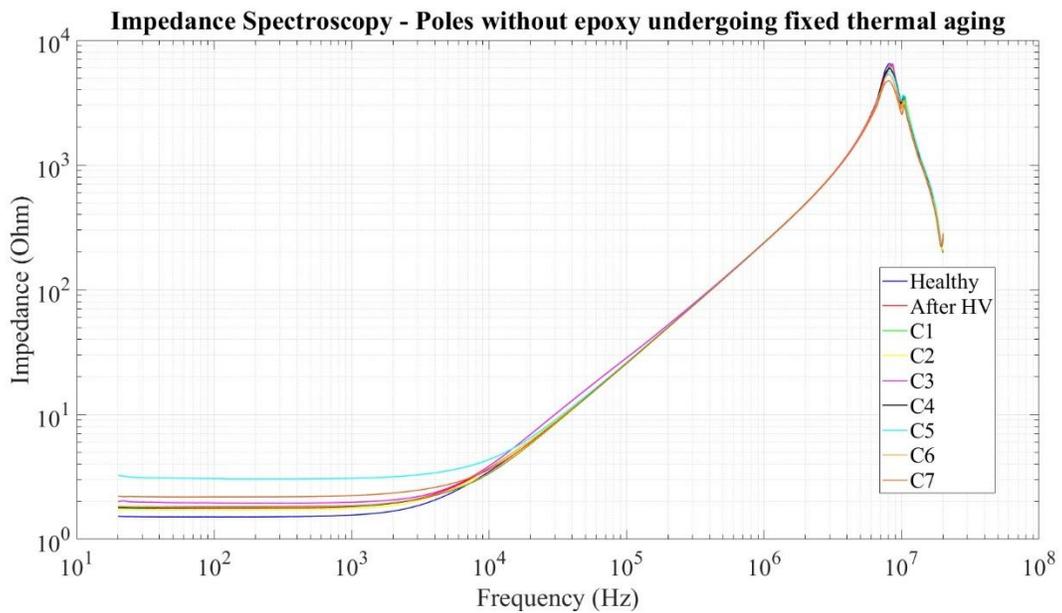
Figure 5.32: Impedance spectroscopy of Group B poles undergoing fixed thermal stress
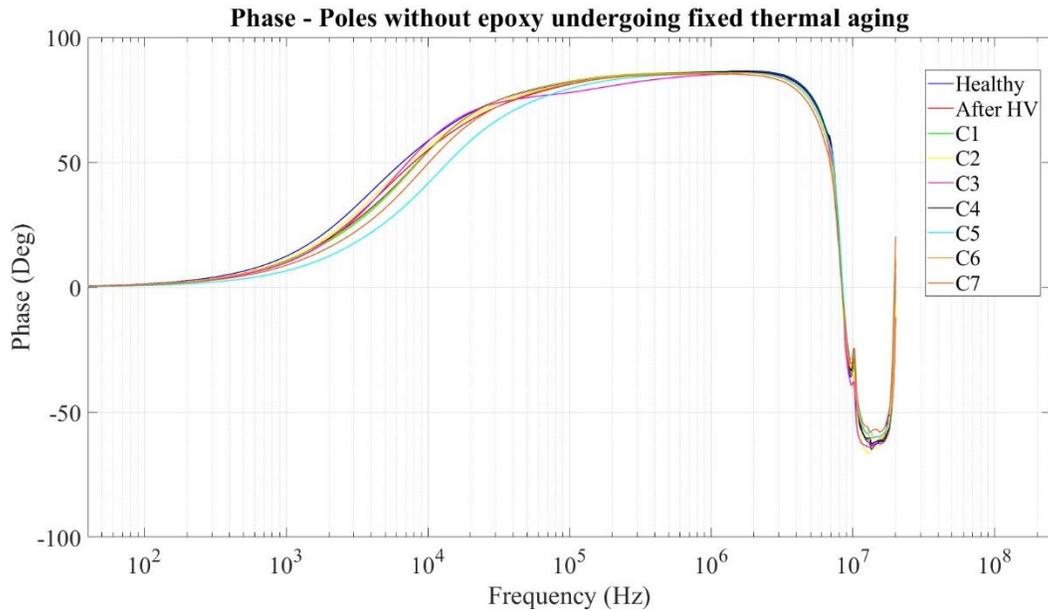
Figure 5.33: Phase of Group B poles undergoing fixed thermal stress

In the absence of thermomechanical phenomena, the influence of fixed thermal stress on coil impedance follows a more discernible pattern. Specifically, impregnated poles exhibit a consistent reduction in impedance with increasing thermal stress, accompanied by a slight rightward shift in spectra. Conversely, non-impregnated poles do not demonstrate this monotonic behavior throughout the entire procedure. At temperatures below the maximum permissible limit (220°C), impedance does not display a clear pattern. However, during the last three stress cycles, there is a noticeable, monotonic decrease in ellipsis size among non-impregnated poles, indicating a reduction in insulation resistance. It is noteworthy that impregnated poles show a similar trend, albeit with changes in ellipsis shape following the final stressing. This could potentially be attributed to concurrent alterations in the dielectric properties of both the epoxy and thin-film insulating materials.
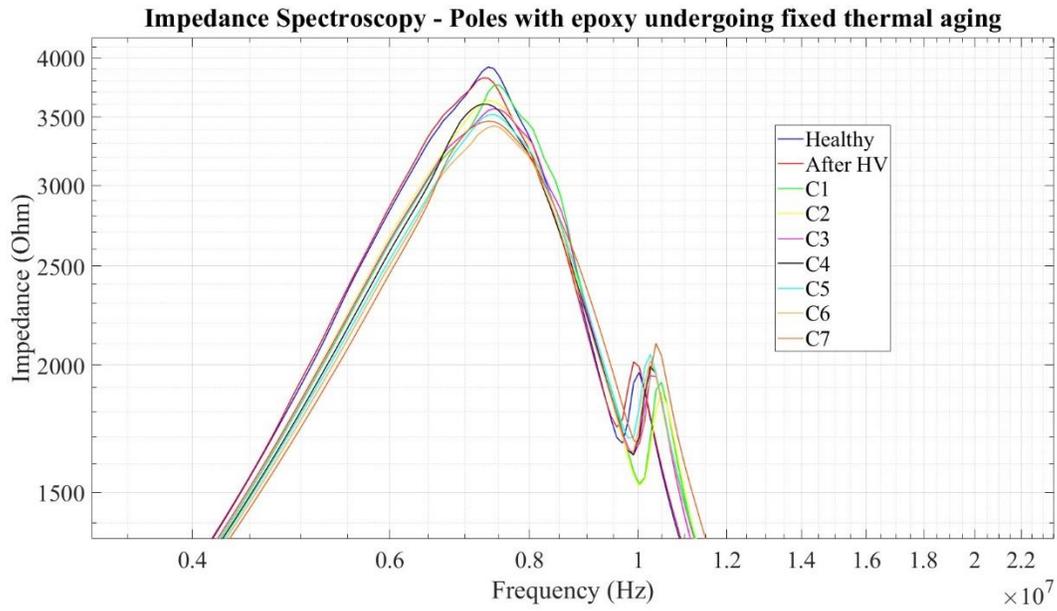
Figure 5.34: Impedance spectroscopy at high frequencies of Group A poles undergoing fixed thermal stress
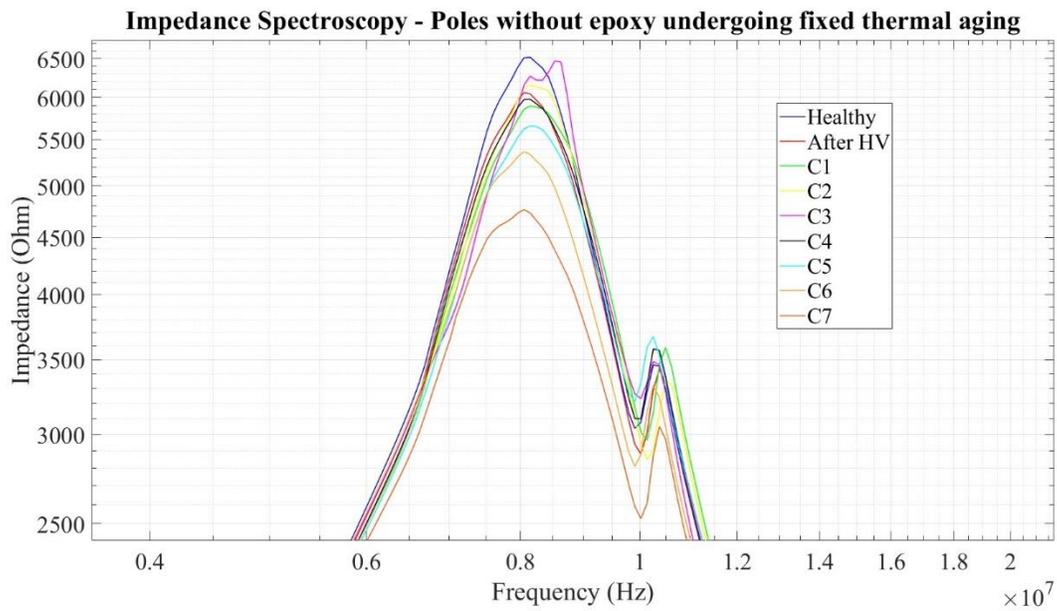
Figure 5.35: Impedance spectroscopy at high frequencies of Group B poles undergoing fixed thermal stress
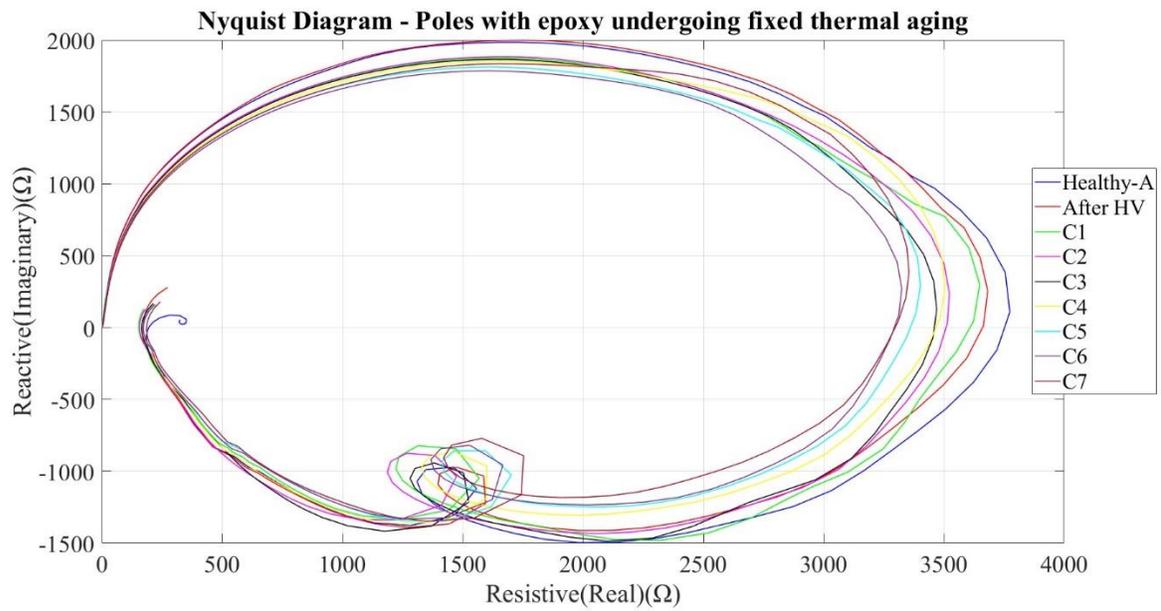
Figure 5.36: Nyquist diagram of Group A poles undergoing fixed thermal stress
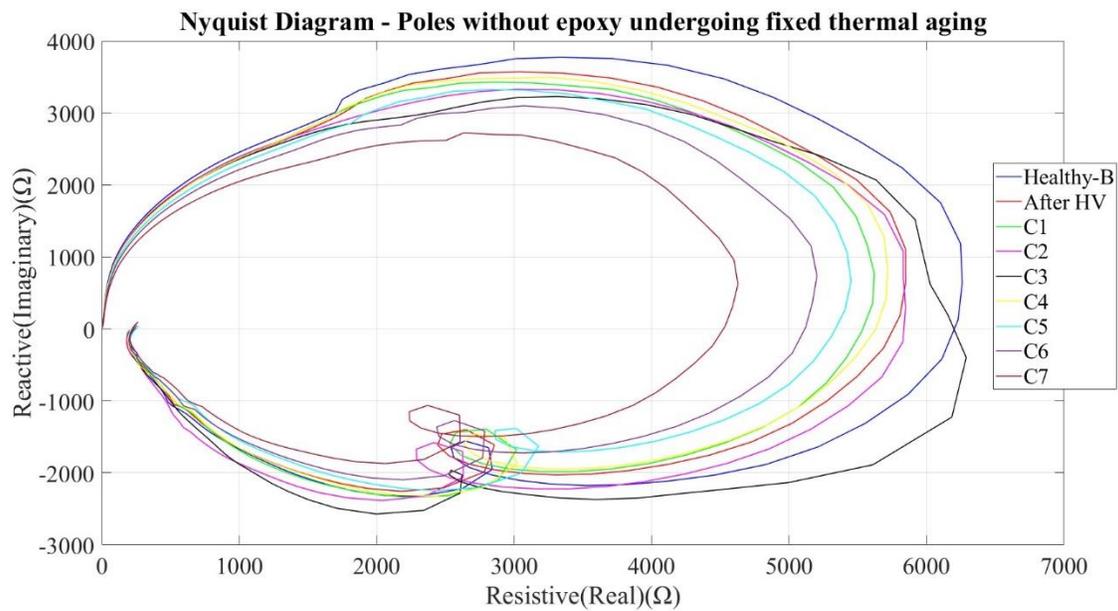
Figure 5.37: Nyquist diagram of Group B poles undergoing fixed thermal stress

o   Comparison of Groups A & B

Upon comparing the average values of impregnated and non-impregnated poles as depicted in the impedance and Nyquist figures, similar conclusions can be drawn as with thermal cycling stress. Specifically, impregnated poles exhibit significantly lower impedance and a reduced Nyquist ellipsis size. This disparity is not primarily attributable to additional resistance introduced by epoxy, but rather to capacitance variations due to epoxy (Group A poles), or introduced air (Group B poles).
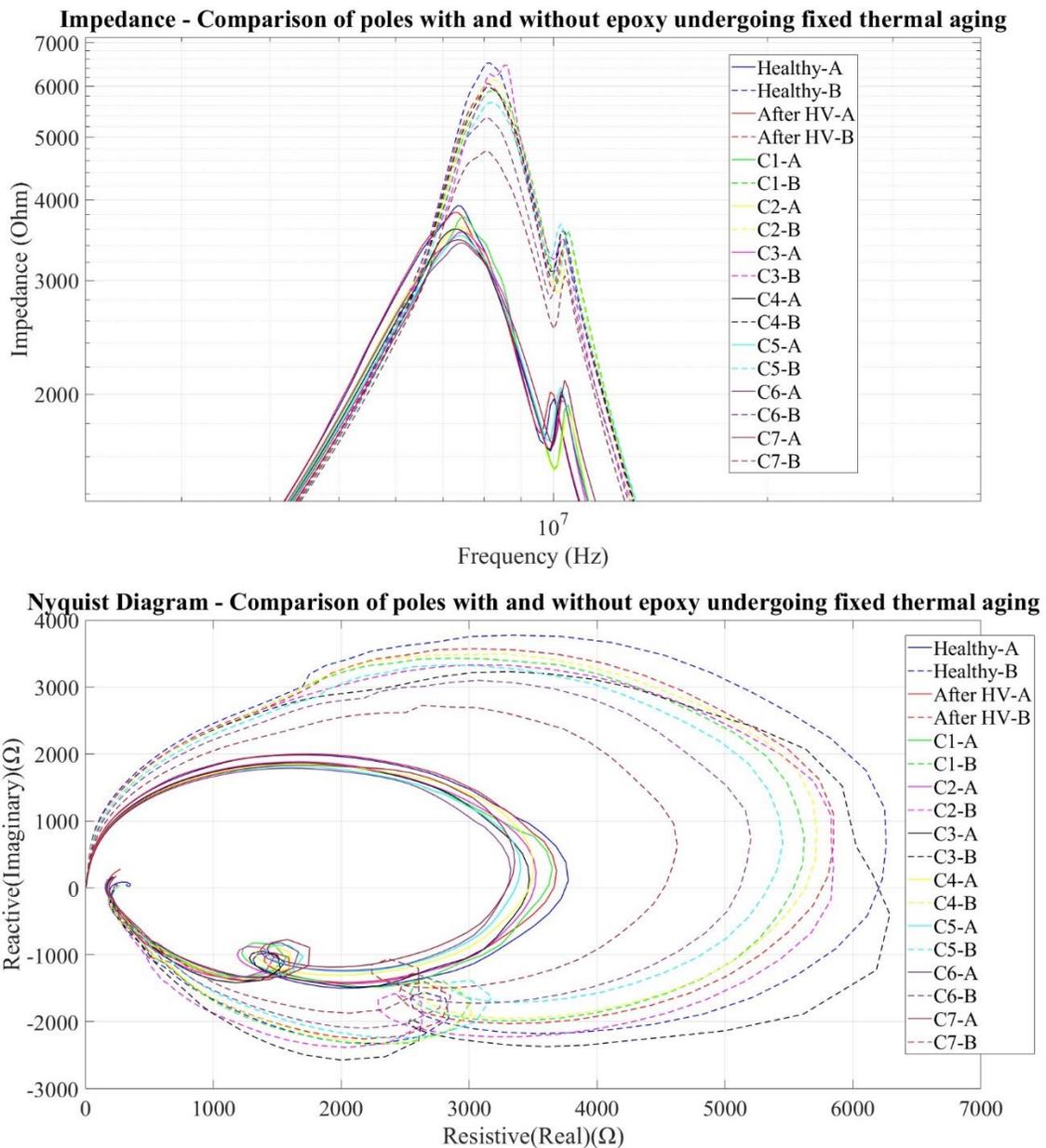
Figure 5.38: Impedance spectroscopy and Nyquist diagram of both Groups compared undergoing fixed thermal stress

5.3 Multi-Stress Analysis

In addition to thermal and thermomechanical stress, investigating the impact of mechanical stress is crucial. Mechanical stress can manifest in various forms and is primarily induced by the diverse forces generated within the machinery and exerted on the conductors. To address this concern, an in-house designed mechanical accelerator has been developed.

This device comprises an inverter-fed induction motor, whose rotational motion is converted into linear oscillation. The resultant pulsating linear movement is imparted to a wagon holding six poles connected in series and shorted. Enclosed within a C-shaped iron chamber, the wagon moves along a track lined with a series of magnets. Consequently, the poles are not only subjected to mechanical vibration induced by the induction motor but also experience an electromotive force (EMF) according to Faraday's law. This induces eddy currents, thereby giving rise to Laplace forces at twice the frequency of the oscillation.

Figure 5.39: The developed device for mechanical stressing of the poles
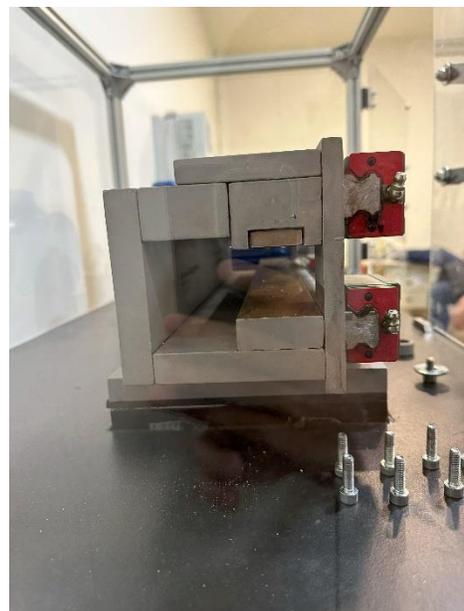
Figure 5.40: Sideview of the iron chamber

The test conducted served as a continuation of the thermal cycling stress. Following the completion of the thermal cycling testing, the poles of Group A (epoxy impregnated), underwent two mechanical cycles, with high-voltage testing conducted in between, thus resulting in an electromechanical test procedure. To elaborate, the complete stressing procedure is outlined in the table below, including the 8 thermal cycles and the 1st high-voltage testing, which are already discussed.

Table 5.10: Complete stressing procedure

Stressing Procedure		
Type of Stress	**Duration**	**Parameters**
Thermal Cycling	8 cycles	
1st High-Voltage	Until breakdown	Voltage Ramp Increment
1st Mechanical	1 hour	5 Hz (motor)
2nd High-Voltage	Until breakdown	Voltage Ramp Increment
2nd Mechanical	1 hour	5 Hz (motor)
3rd High-Voltage	Until breakdown	Voltage Ramp Increment

As previously mentioned in the high-voltage testing section conducted after the 8 thermal cycles, healthy values were established using poles that had only undergone the high-voltage test, solely to determine their coil-to-pole resistance. The procedure for the early breakdown test measurement remained consistent, utilizing the 15 kV Megohmmeter. In total, 2 mechanical stressing cycles and 3 breakdown voltage measurements were executed.

The impedance spectroscopy figure and the Nyquist diagram of the multi-stress testing are presented below. A non-monotonic behavior can be observed as there is no clear pattern that the amplitude or the ellipsis follows. Despite that, it can be noted that after the pole reaches a critical degradation state (after the 2nd mechanical cycle and the 3rd high-voltage measurement), the electromechanical stress tends to elevate the impedance and increase the size of the Nyquist ellipsis. This is a clear consequence of delamination effects caused by the drop in the insulation capacitance and consequently the increase of the capacitive reactance.
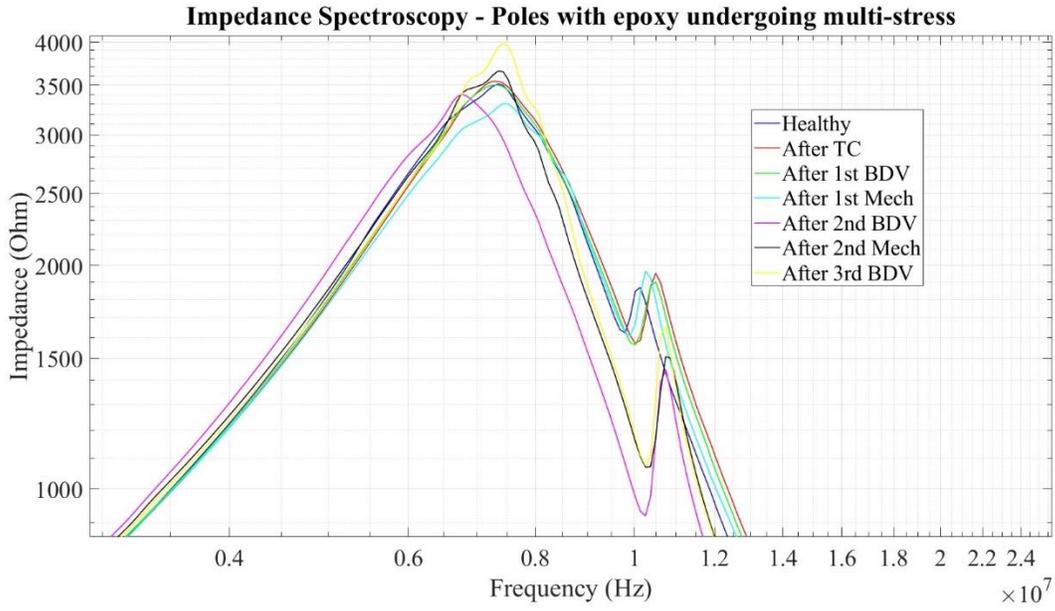
Figure 5.41: Impedance spectroscopy at high frequencies of Group A poles undergoing multi-stress
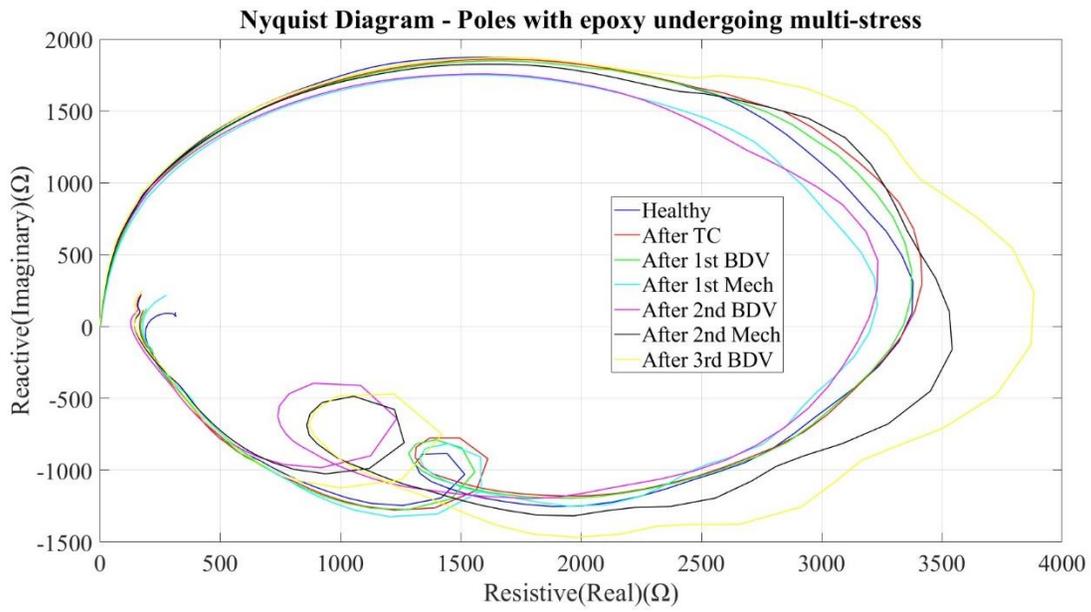
Figure 5.42: Nyquist diagram of Group A poles undergoing multi-stress

The resulting histogram is presented alongside the computed Normal and Weibull distributions. Although the two distributions exhibit minor differences, a more consistent trend is observed in the normal distribution. A table displaying the averages and standard deviations is provided below. It is evident that mechanical vibrations profoundly affect insulation integrity. Despite negligible changes in the average breakdown voltage (with drops of 1% and 3.5% after each mechanical stress cycle compared to the condition after thermal cycling), the standard deviation is notably impacted, experiencing increases of 64% and 146% after each mechanical stress cycle relative to the condition after thermal cycling, suggesting that certain poles experienced a significant reduction in their breakdown voltage.
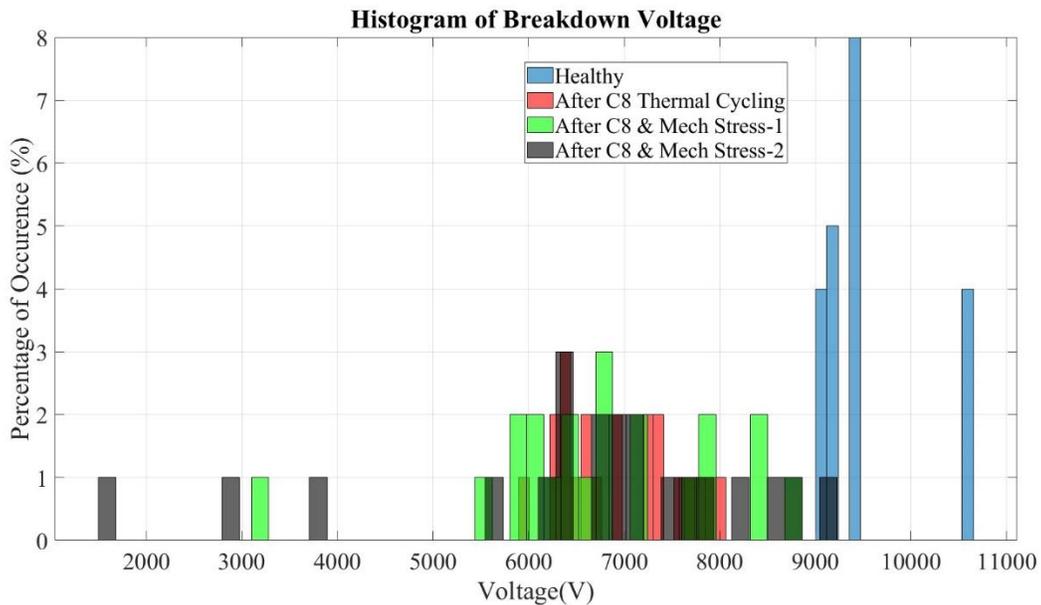
Figure 5.43: Histogram of breakdown voltage throughout the complete stressing procedure

Table 5.11: Average values and standard deviations of breakdown voltage

Normal Distribution Parameters		
Status	**Average Value (V)**	**Standard Deviation (V)**
Healthy	9.5466e+03	635.29
After 8 thermal cycles	6.8303e+03	761.14
After 1st mechanical cycle	6.7665e+03	1246.26
After 2nd mechanical cycle	6.5908e+03	1869.71
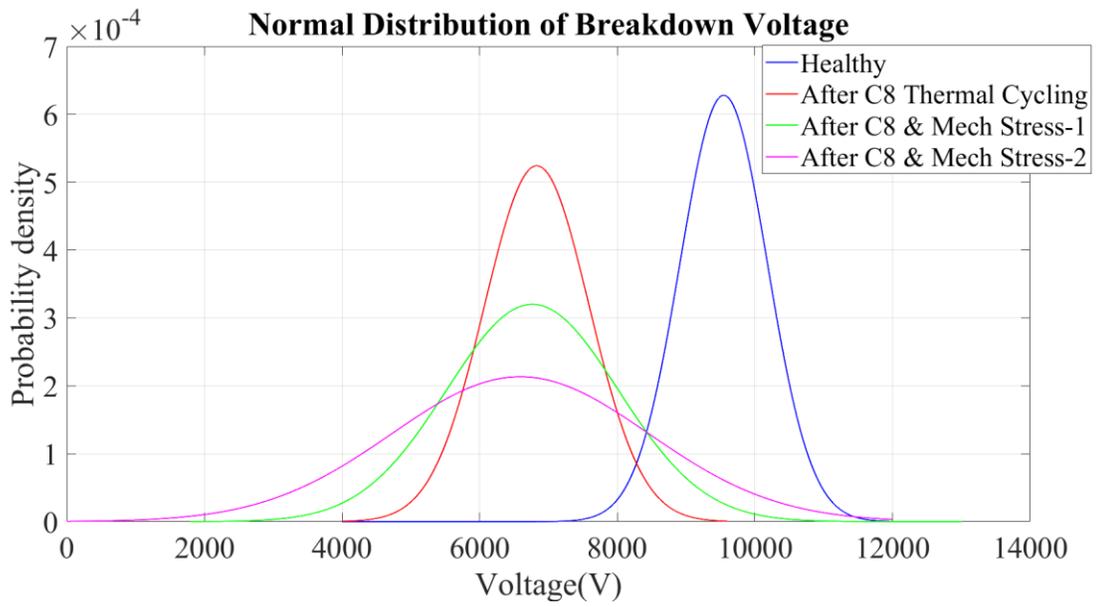
Figure 5.44: Normal distribution of breakdown voltage
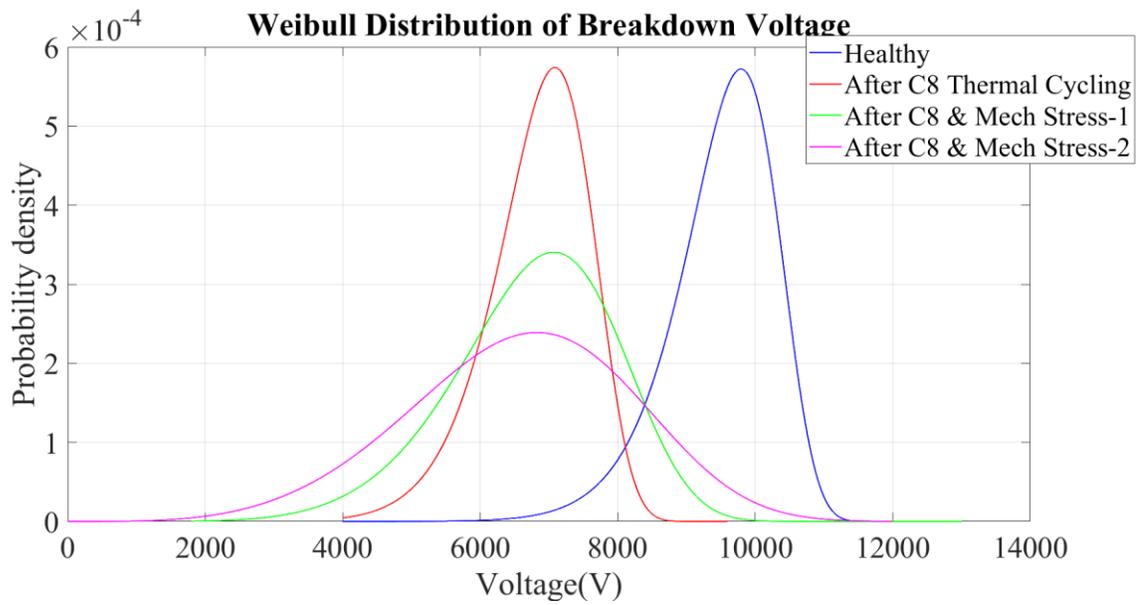
Figure 5.45: Weibull distribution of breakdown voltage

5.4 Conclusions and Future Work

↯ <u>Conclusions</u>

At the project's outset, a methodology was established to create an accurate equivalent circuit representation of motor poles with mounted armature coils, rooted in experimental testing. This model, derived from experimentation, factors in the end effects of the coil and the parasitic impact of the impedance analyzer, making it adaptable to various equipment setups. Besides providing an accurate depiction and deep understanding of motor pole behavior, this model facilitated the development of a fault library detectable through impedance spectroscopy. Simultaneously, it enabled the study of material tolerances and manufacturing defects via statistical analysis of measured parameters across a significant pole population.

The experiments conducted yielded extensive insights into traction motor poles subjected to different accelerated degradation mechanisms, particularly focusing on thermal cycling stress. Impedance spectroscopy and Nyquist diagrams served as crucial monitoring methods, revealing nuanced information about fault diagnosis and overall impedance spectrum changes. In fact, spectroscopy includes a main and a second maximum impedance at high frequencies, which are very informative when it comes to the diagnosis of faults, while at the same time, the Nyquist plot can be very useful to identify overall changes in the impedance spectra because they combine the impedance and phase versus the frequency pieces of information.

While impedance spectroscopy alone may detect manufacturing faults in individual poles, its reliability diminishes with degradation due to conflicting parameter changes. For instance, aged poles may exhibit curve figures resembling healthy conditions, complicating the degradation assessment, especially when multiple dielectric materials, such as thin film and epoxy, are involved. Monotonic outcomes in impedance spectroscopy are observed only under fixed thermal stress on non-impregnated poles; however, impregnated poles undergoing thermal cycling exhibit complex behaviors, due to different insulating materials and thermomechanical effects. The poles may also change color after being subjected to thermal cycling stress, but unfortunately, this discoloration of thermally aged poles compared to healthy ones cannot be depicted.

Electromechanical stress exacerbates material weakening post-thermal cycling stress, attributed to early delamination effects within the coil. This stress enlarges the Nyquist ellipsis after poles reach critical degradation states, indicative of delamination effects caused by the drop in the insulation capacitance and consequently the increase of the capacitive reactance.

Regarding breakdown voltage, high-voltage testing revealed significant insulation degradation, while at the same time stressed the insulation electrically. Thermal cycling stress decreases breakdown voltage, yet the standard deviation of sample distribution remains akin to healthy cases. Conversely, electromechanical stress affects the standard deviation but not the average breakdown voltage. Despite the average breakdown voltage remaining unchanged after consecutive mechanical stress cycles post-thermal degradation, weak spots induced by mechanical stress lead to early insulation breakdown at significantly lower voltages.

⚓ Recommendations for Future Work

Like any research endeavor, this project is subject to time constraints and calls for further exploration in the future. While the pole model developed here is intricate and analytical compared to existing literature, there remain aspects ripe for enhancement to achieve a more comprehensive and precise representation. One such aspect is the incorporation of individual complex inductance between each turn and the core, offering the potential to unveil location-specific fault information for more detailed degradation analysis.

Regarding the thermal cycling test and stress mechanisms overall, it is advisable to conduct additional thermal cycles with extended durations to observe more pronounced and severe degradation outcomes. Exploring various TEAM stresses in combination can illuminate the holistic impact of complex degradation and yield accurate insights into motor pole longevity and integrity. Additionally, conducting a series of degradation studies with adjacent poles would enable investigation into the turn-to-turn short circuit mechanism.

6) REFERENCES

[1]   A. Krings and C. Monissen, "Review and Trends in Electric Traction Motors for Battery Electric and Hybrid Vehicles," 2020 International Conference on Electrical Machines (ICEM), Gothenburg, Sweden, 2020, pp. 1807-1813, doi: 10.1109/ICEM49940.2020.9270946.

[2]   M. S. Patil and S. S. Dhamal, "A Detailed Motor Selection for Electric Vehicle Traction System," *2019 Third International conference on I-SMAC (IoT in Social, Mobile, Analytics and Cloud) (I-SMAC)*, Palladam, India, 2019, pp. 679-684, doi: 10.1109/I-SMAC47947.2019.9032616.

[3]   M. Wang and Z. Chen, "Research on Permanent Magnet Structure of Permanent Magnet Synchronous Motor for Electric Vehicle," 2022 2nd International Conference on Electrical Engineering and Control Science (IC2ECS), Nanjing, China, 2022, pp. 990-993, doi: 10.1109/IC2ECS57645.2022.10087921.

[4]   J Chapman, Stephen. *Electric machinery fundamentals*. McGraw-hill, 2004.

[5]   Tsegaye, Shewit, and Kinde A. Fante. "Analysis of synchronous machine excitation systems: comparative study." *International Journal of Energy and Power Engineering* 10.12 (2017): 1492-1496.

[6]   Schmuelling, S., et al. "Comparison of Different Methods for Excitation of Synchronous Machines." *Maszyny Elektryczne: Zeszyty Problemowe*, vol. 3, no. 107, Sieć Badawcza Łukasiewicz - Instytut Napędów i Maszyn Elektrycznych Komel, 2015, pp. 89–93.

[7]   J. K. NØland, M. Giset and E. F. Alves, "Continuous Evolution and Modern Approaches of Excitation Systems for Synchronous Machines," 2018 XIII International Conference on Electrical Machines (ICEM), Alexandroupoli, Greece, 2018, pp. 104-110, doi: 10.1109/ICELMACH.2018.8507212.

[8]   J. K. Nøland, S. Nuzzo, A. Tessarolo and E. F. Alves, "Excitation System Technologies for Wound-Field Synchronous Machines: Survey of Solutions and Evolving Trends," in *IEEE Access*, vol. 7, pp. 109699-109718, 2019, doi: 10.1109/ACCESS.2019.2933493.

[9]   C. Ranjan, "Modelling Theory and Applications of the Electromagnetic Vibrational Generator", Sustainable Energy Harvesting Technologies - Past, Present and Future. InTech, Dec. 22, 2011. doi: 10.5772/27236.

[10]   Widmer, James D., Richard Martin, and Mohammed Kimiabeigi. "Electric vehicle traction motors without rare earth magnets." *Sustainable Materials and Technologies* 3 (2015): 7-13.

[11]   S. J. Galioto, P. B. Reddy, A. M. EL-Refaie and J. P. Alexander, "Effect of Magnet Types on Performance of High-Speed Spoke Interior-Permanent-Magnet Machines Designed for Traction Applications," in *IEEE Transactions on Industry Applications*, vol. 51, no. 3, pp. 2148-2160, May-June 2015, doi: 10.1109/TIA.2014.2375380.

[12]   S. Huang, M. Aydin, and T.A. Lipo, "TORUS Concept Machines: PrePrototyping Assessment for Two Major Topologies". Int. Conf. Rec. IEEE IAS Annual Meeting, Chicago, pp. 1619-1625, Oct. 2001.

[13]   T. J. Woolmer and M. D. McCulloch, "Analysis of the Yokeless And Segmented Armature Machine," *2007 IEEE International Electric Machines & Drives Conference*, Antalya, Turkey, 2007, pp. 704-708, doi: 10.1109/IEMDC.2007.382753.

[14]   N. Ahmed and G. J. Atkinson, "A Review of Soft Magnetic Composite Materials and Applications," *2022 International Conference on Electrical Machines (ICEM)*, Valencia, Spain, 2022, pp. 551-557, doi: 10.1109/ICEM51905.2022.9910712.

[15]   B. Zhang, T. Seidler, R. Dierken and M. Doppelbauer, "Development of a Yokeless and Segmented Armature Axial Flux Machine," in *IEEE Transactions on Industrial Electronics*, vol. 63, no. 4, pp. 2062-2071, April 2016, doi: 10.1109/TIE.2015.2500194.

[16]   Wang, Guangchen, et al. "Thermal Model Approach to the YASA Machine for In-Wheel Traction Applications." *Energies* 15.15 (2022): 5431.

[17]   C. Wang, X. Hu, X. Wang, W. Geng, Q. Li and J. Hou, "Design and Performance Analysis of Single-phase Axial Flux Permanent Magnet Motor for Coaxial Cascade," *2022 24th European Conference on Power Electronics and Applications (EPE'22 ECCE Europe)*, Hanover, Germany, 2022, pp. 1-7.

[18]   J. Yun and S. B. Lee, "Influence of Aluminum Die-Cast Rotor Porosity on the Efficiency of Induction Machines," in *IEEE Transactions on Magnetics*, vol. 54, no. 11, pp. 1-5, Nov. 2018, Art no. 8104905, doi: 10.1109/TMAG.2018.2841912.

[19]   C. -W. Seo, D. Jang, Y. -H. Hwang, I. -S. Song, Y. -J. Kim and S. -Y. Jung, "Optimal Design of Induction Machine for Spindle Motor Considering Rotor Conductor Bar Porosity," *2023 26th International Conference on Electrical Machines and Systems (ICEMS)*, Zhuhai, China, 2023, pp. 3760-3763, doi: 10.1109/ICEMS59686.2023.10344838.

[20]   M. Sumislawska, K. N. Gyftakis, D. F. Kavanagh, M. D. McCulloch, K. J. Burnham and D. A. Howey, "The Impact of Thermal Degradation on Properties of Electrical Machine Winding Insulation Material," in *IEEE Transactions on Industry Applications*, vol. 52, no. 4, pp. 2951-2960, July-Aug. 2016, doi: 10.1109/TIA.2016.2544745.

[21]   P. A. Panagiotou, A. Lambourne and G. W. Jewell, "Survey of Insulation in Electrical Machines for Aerospace: Systems, Materials & Inspection," *2022 International Conference on Electrical Machines (ICEM)*, Valencia, Spain, 2022, pp. 2318-2324, doi: 10.1109/ICEM51905.2022.9910857.

[22]   M. Borghei and M. Ghassemi, "Insulation Materials and Systems for More- and All-Electric Aircraft: A Review Identifying Challenges and Future Research Needs," in *IEEE Transactions on Transportation Electrification*, vol. 7, no. 3, pp. 1930-1953, Sept. 2021, doi: 10.1109/TTE.2021.3050269.

[23]   T. W. Dakin, "Electrical Insulation Deterioration Treated as a Chemical Rate Phenomenon," in *Transactions of the American Institute of Electrical Engineers*, vol. 67, no. 1, pp. 113-122, Jan. 1948, doi: 10.1109/T-AIEE.1948.5059649.

[24]   G. C. Montanari and L. Simoni, "Aging phenomenology and modeling," in *IEEE Transactions on Electrical Insulation*, vol. 28, no. 5, pp. 755-776, Oct. 1993, doi: 10.1109/14.237740.

[25]   G.C. Stone, E.A. Boulter, I. Culbert and H. Dhirani, "Electrical insulation for rotating machines: design evaluation aging testing and repair" in , John Wiley & Sons, vol. 21, 2004, ISBN 0-471-44506-1.

[26]   R. Hemmati, F. Wu and A. El-Refaie, "Survey of Insulation Systems in Electrical Machines," *2019 IEEE International Electric Machines & Drives Conference (IEMDC)*, San Diego, CA, USA, 2019, pp. 2069-2076, doi: 10.1109/IEMDC.2019.8785099.

[27]   S. Jeenmuang, P. Pannil, S. Mongkolsatitpong, S. Trakuldit, V. Wuti and N. Pattanadech, "The Application of Polarization and Depolarization Current on the Large Turbo-generators," *2022 9th International Conference on Condition Monitoring and Diagnosis (CMD)*, Kitakyushu, Japan, 2022, pp. 118-121, doi: 10.23919/CMD54214.2022.9991272.

[28]   Y. Rao, Y. Wang and W. Wang, "A Simplified Modeling and Analysis Method for Interturn Short-Circuit Fault of Permanent Magnet Synchronous Motor," *2023 26th International Conference on Electrical Machines and Systems (ICEMS)*, Zhuhai, China, 2023, pp. 4450-4455, doi: 10.1109/ICEMS59686.2023.10345238.

[29]   L. Frosini, "Monitoring and Diagnostics of Electrical Machines and Drives: a State of the Art," *2019 IEEE Workshop on Electrical Machines Design, Control and Diagnosis (WEMDCD)*, Athens, Greece, 2019, pp. 169-176, doi: 10.1109/WEMDCD.2019.8887815.

[30]   J. -R. Riba Ruiz, J. A. Rosero, A. Garcia Espinosa and L. Romeral, "Detection of Demagnetization Faults in Permanent-Magnet Synchronous Motors Under Nonstationary Conditions," in *IEEE Transactions on Magnetics*, vol. 45, no. 7, pp. 2961-2969, July 2009, doi: 10.1109/TMAG.2009.2015942.

[31]   B. M. Ebrahimi and J. Faiz, "Configuration Impacts on Eccentricity Fault Detection in Permanent Magnet Synchronous Motors," in *IEEE Transactions on Magnetics*, vol. 48, no. 2, pp. 903-906, Feb. 2012, doi: 10.1109/TMAG.2011.2172977.

[32]   B. M. Ebrahimi, J. Faiz, M. Javan-Roshtkhari and A. Zargham Nejhad, "Static Eccentricity Fault Diagnosis in Permanent Magnet Synchronous Motor Using Time Stepping Finite Element Method," in *IEEE Transactions on Magnetics*, vol. 44, no. 11, pp. 4297-4300, Nov. 2008, doi: 10.1109/TMAG.2008.2001534.

[33]   Ukil, Abhisek, Shuo Chen, and Andrea Andenna. "Detection of stator short circuit faults in three-phase induction motors using motor current zero crossing instants." *Electric Power Systems Research* 81.4 (2011): 1036-1044.

[34]   J. Tang, X. Ding, Y. Wang, D. Li, B. Chen and C. Wang, "Condition Monitoring of Permanent Magnet Synchronous Motor under Different Stator Fault Severity," *2021 Global Reliability and Prognostics and Health Management (PHM-Nanjing)*, Nanjing, China, 2021, pp. 1-4, doi: 10.1109/PHM-Nanjing52125.2021.9613131.

[35]   Y. Qi, E. Bostanci, V. Gurusamy and B. Akin, "A Comprehensive Analysis of Short-Circuit Current Behavior in PMSM Interturn Short-Circuit Faults," in *IEEE Transactions on Power Electronics*, vol. 33, no. 12, pp. 10784-10793, Dec. 2018, doi: 10.1109/TPEL.2018.2809668.

[36]   A. Upadhyay, M. Alaküla and F. J. Márquez-Fernández, "Characterization of Onboard Condition Monitoring Techniques for Stator Insulation Systems in Electric Vehicles - A Review," *IECON 2019 - 45th Annual Conference of the IEEE Industrial Electronics Society*, Lisbon, Portugal, 2019, pp. 3179-3186, doi: 10.1109/IECON.2019.8926678.

[37]   Y. Zuo, A. Darabi, C. Lai and K. Lakshmi Varaha Iyer, "Online Interturn Short Circuits Fault Monitoring for Permanent Magnet Synchronous Machines," *IECON 2022 – 48th Annual Conference of the IEEE Industrial Electronics Society*, Brussels, Belgium, 2022, pp. 1-6, doi: 10.1109/IECON49645.2022.9968716.

[38]   B. -G. Gu, J. -H. Choi and I. -S. Jung, "Development and Analysis of Interturn Short Fault Model of PMSMs With Series and Parallel Winding Connections," in *IEEE Transactions on Power Electronics*, vol. 29, no. 4, pp. 2016-2026, April 2014, doi: 10.1109/TPEL.2013.2265400.

[39]   J. Faiz and H. Nejadi-Koti, "Demagnetization Fault Indexes in Permanent Magnet Synchronous Motors—An Overview," in *IEEE Transactions on Magnetics*, vol. 52, no. 4, pp. 1-11, April 2016, Art no. 8201511, doi: 10.1109/TMAG.2015.2480379.

[40]   J. Hong *et al.*, "Detection and Classification of Rotor Demagnetization and Eccentricity Faults for PM Synchronous Motors," in *IEEE Transactions on Industry Applications*, vol. 48, no. 3, pp. 923-932, May-June 2012, doi: 10.1109/TIA.2012.2191253.

[41]   J. Hong, D. Hyun, S. B. Lee, J. -Y. Yoo and K. -W. Lee, "Automated Monitoring of Magnet Quality for Permanent-Magnet Synchronous Motors at Standstill," in *IEEE Transactions on Industry Applications*, vol. 46, no. 4, pp. 1397-1405, July-Aug. 2010, doi: 10.1109/TIA.2010.2049811.

[42]   Hendershot, James R., and Timothy John Eastham Miller. *Design of brushless permanent-magnet motors*. Oxford University Press, 1995.

[43]   J. A. Haylock, U. M. Hoefer and A. G. Jack, "Predicting and preventing demagnetisation in permanent magnet motor drives", *Proc. 3rd Int. Conf. Power Electron. Mach. Drives*, pp. 474-478, 2006-Mar.

[44]   R. Speed and A. K. Wallace, "Remedial strategies for brushless DC drive failures," in *IEEE Transactions on Industry Applications*, vol. 26, no. 2, pp. 259-266, March-April 1990, doi: 10.1109/28.54251.

[45]   D. Kastha and B. K. Bose, "Investigation of fault modes of voltage-fed inverter system for induction motor drive," *Conference Record of the 1992 IEEE Industry Applications Society Annual Meeting*, Houston, TX, USA, 1992, pp. 858-866 vol.1, doi: 10.1109/IAS.1992.244307.

[46]   Furlani, Edward P. *Permanent magnet and electromechanical devices: materials, analysis, and applications*. Academic Press, 2001.

[47]   C. W. Cheng, H. C. Man and F. T. Cheng, "Magnetic and corrosion characteristics of Nd-Fe-B magnet with various surface coatings," in *IEEE Transactions on Magnetics*, vol. 33, no. 5, pp. 3910-3912, Sept. 1997, doi: 10.1109/20.619612.

[48]   A. El-Moneim, A. Gebert, F. Schneider, O. Gutfleisch and L. Schultz, "Grain growth effects on the corrosion behavior of nanocrystalline NdFeB magnets", *Corros. Sci.*, vol. 44, no. 5, pp. 1097-1112, May 2002.

[49]   K. . -C. Kim, S. . -B. Lim, D. . -H. Koo and J. Lee, "The Shape Design of Permanent Magnet for Permanent Magnet Synchronous Motor Considering Partial Demagnetization," in *IEEE Transactions on Magnetics*, vol. 42, no. 10, pp. 3485-3487, Oct. 2006, doi: 10.1109/TMAG.2006.879077.

[50]   R. Jigyasu, A. Sharma, L. Mathew and S. Chatterji, "A Review of Condition Monitoring and Fault Diagnosis Methods for Induction Motor," 2018 Second International Conference on Intelligent Computing and Control Systems (ICICCS), Madurai, India, 2018, pp. 1713-1721, doi: 10.1109/ICCONS.2018.8662833.

[51]   J. A. Antonino-Daviu, A. Quijano-Lopez, V. Fuster-Roig and C. Nevot, "Case stories of induction motors fault diagnosis based on current analysis," 2016 Petroleum and Chemical Industry Conference Europe (PCIC Europe), Berlin, Germany, 2016, pp. 1-9, doi: 10.1109/PCICEurope.2016.7604635.

[52]   V. Gurusamy, G. -A. Capolino, B. Akin, H. Henao, R. Romary and R. Pusca, "Recent Trends in Magnetic Sensors and Flux-Based Condition Monitoring of Electromagnetic Devices," in IEEE Transactions on Industry Applications, vol. 58, no. 4, pp. 4668-4684, July-Aug. 2022, doi: 10.1109/TIA.2022.3174804.

[53]   Y. Park et al., "Stray Flux Monitoring for Reliable Detection of Rotor Faults Under the Influence of Rotor Axial Air Ducts," in IEEE Transactions on Industrial Electronics, vol. 66, no. 10, pp. 7561-7570, Oct. 2019, doi: 10.1109/TIE.2018.2880670.

[54]   K. N. Gyftakis, P. A. Panagiotou and D. Spyrakis, "Recent Experiences with MCSA and Flux Condition Monitoring of Mechanical Faults in 6kV Induction Motors for Water Pumping Applications," 2019 IEEE 12th International Symposium on Diagnostics for Electrical Machines, Power Electronics and Drives (SDEMPED), Toulouse, France, 2019, pp. 214-219, doi: 10.1109/DEMPED.2019.8864923.

[55]   A. Ceban, R. Pusca and R. Romary, "Study of Rotor Faults in Induction Motors Using External Magnetic Field Analysis," in IEEE Transactions on Industrial Electronics, vol. 59, no. 5, pp. 2082-2093, May 2012, doi: 10.1109/TIE.2011.2163285.

[56]   H. Henao, C. Demian and G. . -A. Capolino, "A frequency-domain detection of stator winding faults in induction machines using an external flux sensor," in IEEE Transactions on Industry Applications, vol. 39, no. 5, pp. 1272-1279, Sept.-Oct. 2003, doi: 10.1109/TIA.2003.816531.

[57]   P. Song, W. Li, S. Mukundan and N. C. Kar, "An Overview of Noise-Vibration-Harshness Analysis for Induction Machines and Permanent Magnet Synchronous Machines," 2020 10th International Electric Drives Production Conference (EDPC), Ludwigsburg, Germany, 2020, pp. 1-8, doi: 10.1109/EDPC51184.2020.9388189.

[58]   T. Sun, J. -M. Kim, G. -H. Lee, J. -P. Hong and M. -R. Choi, "Effect of Pole and Slot Combination on Noise and Vibration in Permanent Magnet Synchronous Motor," in IEEE Transactions on Magnetics, vol. 47, no. 5, pp. 1038-1041, May 2011, doi: 10.1109/TMAG.2010.2093872.

[59]   S. Fábry, M. Češkovič and N. Gecejová, "Aircraft Gas Turbine Engine Vibration Diagnostic Method," 2022 New Trends in Aviation Development (NTAD), Novy Smokovec, Slovakia, 2022, pp. 54-60, doi: 10.1109/NTAD57912.2022.10013635.

[60]   M. Barański, "New vibration diagnostic method of PM generators and traction motors - detecting of vibrations caused by unbalance," 2014 IEEE International Energy Conference (ENERGYCON), Cavtat, Croatia, 2014, pp. 28-32, doi: 10.1109/ENERGYCON.2014.6850401.

[61]   N. Emery, Y. Li and B. Bilgin, "Frequency-Band Analysis for Acoustic Noise Characterization of an Interior Permanent Magnet Motor," IECON 2021 – 47th Annual Conference of the IEEE Industrial Electronics Society, Toronto, ON, Canada, 2021, pp. 1-5, doi: 10.1109/IECON48115.2021.9589425.

[62]   K. N. Gyftakis, D. V. Spyropoulos, J. C. Kappatou and E. D. Mitronikas, "A Novel Approach for Broken Bar Fault Diagnosis in Induction Motors Through Torque Monitoring," in IEEE Transactions on Energy Conversion, vol. 28, no. 2, pp. 267-277, June 2013, doi: 10.1109/TEC.2013.2240683.

[63]   A. M. da Silva, R. J. Povinelli and N. A. O. Demerdash, "Rotor Bar Fault Monitoring Method Based on Analysis of Air-Gap Torques of Induction Motors," in IEEE Transactions on Industrial Informatics, vol. 9, no. 4, pp. 2274-2283, Nov. 2013, doi: 10.1109/TII.2013.2242084.

[64]   A. Fedele, C. Bruzzese, E. Santini and V. Anastasio, "Monitoring of Load-Fault-Induced Torsional Resonances in High-Speed Alternators by Speed and Torque Estimation," IECON 2019 - 45th Annual Conference of the IEEE Industrial Electronics Society, Lisbon, Portugal, 2019, pp. 3679-3684, doi: 10.1109/IECON.2019.8927588.

[65]   M. Zagirnyak, D. Mamchur and A. Kalinov, "Induction motor diagnostic system based on spectra analysis of current and instantaneous power signals," IEEE SOUTHEASTCON 2014, Lexington, KY, USA, 2014, pp. 1-7, doi: 10.1109/SECON.2014.6950721.

[66]   M. V. Zagirnyak, D. G. Mamchur and A. P. Kalinov, "Elimination of the influence of supply mains low-quality parameters on the results of induction motor diagnostics," The XIX

International Conference on Electrical Machines - ICEM 2010, Rome, Italy, 2010, pp. 1-6, doi: 10.1109/ICELMACH.2010.5608071.

[67]   Zagirnyak, Mykhaylo, Dmytro Mamchur, and Andrii Kalinov. "Comparison of induction motor diagnostic methods based on spectra analysis of current and instantaneous power signals." *Przeglad Elektrotechniczny* 88.12 (2012): 221-224.

[68]   H. Ma, Z. Zhang, P. Ju, W. Shi and C. Wang, "Stator fault detection of doubly-fed induction generators using rotor instantaneous power spectrum," 2015 IEEE 10th International Symposium on Diagnostics for Electrical Machines, Power Electronics and Drives (SDEMPED), Guarda, Portugal, 2015, pp. 165-170, doi: 10.1109/DEMPED.2015.7303685.

[69]   E. Reséndiz-Ochoa, L. A. Morales-Hernández, I. A. Cruz-Albarran and S. Álvarez-Junco, "Induction Motor Failure Analysis using Machine Learning and Infrared Thermography," 2022 IEEE International Autumn Meeting on Power, Electronics and Computing (ROPEC), Ixtapa, Mexico, 2022, pp. 1-6, doi: 10.1109/ROPEC55836.2022.10018653.

[70]   M. A. Herrera-Arellano, I. R. Terol-Villalobos, L. A. Morales-Hemandez and M. Valtierra-Rodriguez, "Infrared thermography-based automatic assessment of control components for electric machines," 2017 IEEE 11th International Symposium on Diagnostics for Electrical Machines, Power Electronics and Drives (SDEMPED), Tinos, Greece, 2017, pp. 578-584, doi: 10.1109/DEMPED.2017.8062413.

[71]   X. Wang, S. Si, Y. Li and Y. Li, "A Fault Diagnosis Method for Rotating Machinery Under Variable Speed Condition Based on Infrared Thermography," 2018 International Conference on Sensing,Diagnostics, Prognostics, and Control (SDPC), Xi'an, China, 2018, pp. 30-34, doi: 10.1109/SDPC.2018.8664850.

[72]   D. Lopez-Perez and J. Antonino-Daviu, "Application of infrared thermography to fault detection in industrial induction motors: Case stories," 2016 XXII International Conference on Electrical Machines (ICEM), Lausanne, Switzerland, 2016, pp. 2172-2177, doi: 10.1109/ICELMACH.2016.7732823.

[73]   A. M. Garzón, N. Laiton, V. Sicachá, D. F. Celeita and T. D. Le, "Smart equipment failure detection with machine learning applied to thermography inspection data in modern power systems," 2023 11th International Conference on Smart Grid (icSmartGrid), Paris, France, 2023, pp. 01-05, doi: 10.1109/icSmartGrid58556.2023.10171065.

[74]   Alvarado-Hernandez, Alvaro Ivan et al. "Infrared Thermography Smart Sensor for the Condition Monitoring of Gearbox and Bearings Faults in Induction Motors." *Sensors (Basel, Switzerland)* vol. 22,16 6075. 14 Aug. 2022, doi:10.3390/s22166075

[75]   G. C. Stone, "Condition monitoring and diagnostics of motor and stator windings – A review," in *IEEE Transactions on Dielectrics and Electrical Insulation*, vol. 20, no. 6, pp. 2073-2080, December 2013, doi: 10.1109/TDEI.2013.6678855.

[76]   M. Istad, M. Runde and A. Nysveen, "A Review of Results From Thermal Cycling Tests of Hydrogenerator Stator Windings," in *IEEE Transactions on Energy Conversion*, vol. 26, no. 3, pp. 890-903, Sept. 2011, doi: 10.1109/TEC.2011.2127479.

[77]   Cruz, Jonathan dos Santos, Fabiano Fruett, Renato da Rocha Lopes, Fabio Luiz Takaki, Claudia de Andrade Tambascia, Eduardo Rodrigues de Lima, and Mateus Giesbrecht. 2022. "Partial Discharges Monitoring for Electric Machines Diagnosis: A Review" *Energies* 15, no. 21: 7966. https://doi.org/10.3390/en15217966

[78]   Dmitriev, V., Oliveira, R.M.S., Zampolo, R.F., Moutinho de Vilhena, P.R., de Souza Brasil, F., Fernandes, M.F. (2024). "Partial Discharges: Physics and Classification". In: Partial Discharges in Hydroelectric Generators. Power Systems. Springer, Cham. https://doi.org/10.1007/978-3-031-36604-8_2

[79]   Vogelsang, Ruben. "Time to breakdown of high voltage winding insulations with respect to microscopic properties and manufaturing qualities." PhD diss., ETH Zurich, 2004.

[80]   R. Brütsch and M. Chapman, "Insulating systems for high voltage rotating machines and reliability considerations," *2010 IEEE International Symposium on Electrical Insulation*, San Diego, CA, USA, 2010, pp. 1-5, doi: 10.1109/ELINSL.2010.5549737.

[81]   S. Cotner, "Observations on the Polarization Index Test as Applied to Strip-On-Edge Field Windings of Salient Pole Hydro Generators," *2021 IEEE Electrical Insulation Conference (EIC)*, Denver, CO, USA, 2021, pp. 401-404, doi: 10.1109/EIC49891.2021.9612259.

[82]   "IEEE Recommended Practice for Testing Insulation Resistance of Electric Machinery," in *IEEE Std 43-2013 (Revision of IEEE Std 43-2000)* , vol., no., pp.1-37, 6 March 2014, doi: 10.1109/IEEESTD.2014.6754111.

[83]   C. Hudon, N. Amyot, S. Bernier, E. David and M. Essalihi, "Comparison of DC Ramp and Polarization and Depolarisation Tests on Hydrogenerators," *2018 IEEE Electrical Insulation Conference (EIC)*, San Antonio, TX, USA, 2018, pp. 114-119, doi: 10.1109/EIC.2018.8481087.

[84]   E. David, R. Soltani and L. Lamarre, "PDC measurements to assess machine insulation," in *IEEE Transactions on Dielectrics and Electrical Insulation*, vol. 17, no. 5, pp. 1461-1469, October 2010, doi: 10.1109/TDEI.2010.5595547.

[85]   E. David, L. Lamarre and D. N. Nguyen, "Measurements of polarization/depolarization currents for modern epoxy-mica bars in different conditions," *2007 Electrical Insulation Conference and Electrical Manufacturing Expo*, Nashville, TN, USA, 2007, pp. 189-193, doi: 10.1109/EEIC.2007.4562617.

[86]   S. Cotner, "Insulation testing of AC generator windings," *2017 IEEE Electrical Insulation Conference (EIC)*, Baltimore, MD, USA, 2017, pp. 447-450, doi: 10.1109/EIC.2017.8004652.

[87]   "IEEE Standard 95", *IEEE Recommended Practice for Insulation Testing of AC Electric Machinery (2300V and Above) With High Direct Voltage*.

[88]   "IEEE Standard 115", *IEEE Guide: Test Procedures for Synchronous Machines*.

[89]   T. Chophel, T. Suwanasri and C. Suwanasri, "Condition Assessment of Generator Insulation using Diagnostic Tests," *2019 7th International Electrical Engineering Congress (iEECON)*, Hua Hin, Thailand, 2019, pp. 1-4, doi: 10.1109/iEECON45304.2019.8938897.

[90]   E. David, G. C. Stone and M. Sasic, "Dielectric response of machine insulation extracted from DC ramp test on individual stator bars," *2017 IEEE Electrical Insulation Conference (EIC)*, Baltimore, MD, USA, 2017, pp. 46-49, doi: 10.1109/EIC.2017.8004643.

[91]   A. Nair, E. David and T. Godin, "Experience with DC Ramp Test Performed on Asphalt-Mica insulated Hydraulic Generators," *Conference Record of the 2008 IEEE International Symposium on Electrical Insulation*, Vancouver, BC, Canada, 2008, pp. 166-169, doi: 10.1109/ELINSL.2008.4570302.

[92]   Fei Liu, Xingyi Huang and Pingkai Jiang, "Diagnosis of generator stator winding insulation based on dissipation factor measurement," *Proceedings of 2014 International Symposium on Electrical Insulating Materials*, Niigata, Japan, 2014, pp. 120-123, doi: 10.1109/ISEIM.2014.6870735.

[93]   H. Sedding, G. Stone and A. Shaikh, "Dielectric dissipation factor acceptance criteria for stator winding insulation," *2016 IEEE International Conference on Dielectrics (ICD)*, Montpellier, France, 2016, pp. 955-958, doi: 10.1109/ICD.2016.7547775.

[94]   R. Omranipour and S. U. Haq, "Effect of stress grading systems and guarding techniques on measured power factor and power factor tip-up of electric machinery stator windings," *2009 IEEE Electrical Insulation Conference*, Montreal, QC, Canada, 2009, pp. 414-419, doi: 10.1109/EIC.2009.5166382.

[95]   P. Zhang, P. Neti and K. Younsi, "Online Monitoring of Capacitance and Dissipation Factor of Motor Stator Winding Insulation During Accelerated Life Testing," *2018 IEEE Energy Conversion Congress and Exposition (ECCE)*, Portland, OR, USA, 2018, pp. 3267-3271, doi: 10.1109/ECCE.2018.8558036.

[96]   N. Phloymuk, P. Nimsanong, N. Phumipunepon, S. Potivejkul, T. Wiangtong and N. Pattanadech, "The Dissipation Factor (tan δ) Monitoring of A Stator Winding Insulation of A Synchronous Machine," *2018 Condition Monitoring and Diagnosis (CMD)*, Perth, WA, Australia, 2018, pp. 1-4, doi: 10.1109/CMD.2018.8535666.

[97]   Madonna, Vincenzo, Paolo Giangrande, and Michael Galea. "Evaluation of strand-to-strand capacitance and dissipation factor in thermally aged enamelled coils for low-voltage electrical machines." *IET Science, Measurement & Technology* 13.8 (2019): 1170-1177.

[98]   G. Stone, H. Sedding and W. Veerkamp, "What Medium and High Voltage Stator Winding Partial Discharge Testing Can - And Can Not - Tell You," *2021 IEEE IAS Petroleum and Chemical Industry Technical Conference (PCIC)*, San Antonio, TX, USA, 2021, pp. 293-302, doi: 10.1109/PCIC42579.2021.9728995.

[99]   G. C. Stone, M. K. W. Stranges and D. G. Dunn, "Recent developments in IEEE and IEC standards for off-line and on-line partial discharge testing of motor and generator stator

windings," *2014 IEEE Petroleum and Chemical Industry Technical Conference (PCIC)*, San Francisco, CA, USA, 2014, pp. 79-84, doi: 10.1109/PCICon.2014.6961921.

[100]   *IEEE Guide to the Measurement of Partial Discharges in Rotating Machinery*.

[101]   *Off-Line Partial Discharge Measurements on the Winding Insulation*, 2017.

[102]   A. Gegenava and A. Khazanov, "Statistical Review of Voltage Endurance Test of Insulation for High Voltage Rotating Machines Stator Windings with Combined Standard and Accelerated Tests. "Three Steps Test" TST.," *2023 IEEE Electrical Insulation Conference (EIC)*, Quebec City, QC, Canada, 2023, pp. 1-4, doi: 10.1109/EIC55835.2023.10177305.

[103]   A. Gegenava, A. Khazanov and B. Moore, "Acceleration factors for faster Voltage Endurance Testing on generator insulation systems," *2017 IEEE Electrical Insulation Conference (EIC)*, Baltimore, MD, USA, 2017, pp. 177-180, doi: 10.1109/EIC.2017.8004717.

[104]   A. Khazanov, B. Vakser, A. Gegenava and P. E. B. Moore, "Voltage endurance test at increasing voltage as a tool to express determinations of mathematical model parameters of electrical aging," *2017 IEEE Conference on Electrical Insulation and Dielectric Phenomenon (CEIDP)*, Fort Worth, TX, USA, 2017, pp. 810-815, doi: 10.1109/CEIDP.2017.8257532.

[105]   Q. Zhuang, P. H. F. Morshuis, D. Djairam, J. J. Smit and Z. Xu, "Life prediction for transformer winding insulated with epoxy resin and thickness-reduced paper through voltage endurance tests," *2012 International Conference on High Voltage Engineering and Application*, Shanghai, China, 2012, pp. 115-118, doi: 10.1109/ICHVE.2012.6357066.

[106]   A. Khazanov and A. Gegenava, "Step Increased Voltage Endurance Test as a Tool for Evaluation of Life Expectancy for Stator Windingb Ground Wall Insulation High Voltage Rotating Machines.," *2023 IEEE Electrical Insulation Conference (EIC)*, Quebec City, QC, Canada, 2023, pp. 1-5, doi: 10.1109/EIC55835.2023.10177355.

[107]   J. Yang *et al.*, "Experimental evaluation of using the surge PD test as a predictive maintenance tool for monitoring turn insulation quality in random wound AC motor stator windings," in *IEEE Transactions on Dielectrics and Electrical Insulation*, vol. 19, no. 1, pp. 53-60, February 2012, doi: 10.1109/TDEI.2012.6148502.

[108]   Wilson, John. "Current state of surge testing induction machines." *Iris Rotating Machine Conference*. 2003.

[109]   P. A. Panagiotou, A. Lambourne and G. W. Jewell, "Ex-situ Inspection of Concentrated Stator Coils by Means of Impedance Spectroscopy," *2022 International Conference on Electrical Machines (ICEM)*, Valencia, Spain, 2022, pp. 2331-2337, doi: 10.1109/ICEM51905.2022.9910588.

[110]   P. A. Panagiotou, E. J. W. Stone, J. Mühlthaler, A. Reeh, A. Lambourne and G. W. Jewell, "Thermal Degradation Profile of Concentrated Stator Winding Insulation by Impedance Spectroscopy," *2023 IEEE 14th International Symposium on Diagnostics for Electrical Machines, Power Electronics and Drives (SDEMPED)*, Chania, Greece, 2023, pp. 554-560, doi: 10.1109/SDEMPED54949.2023.10271468.

[111] P. Neti and S. Grubic, "Online Broadband Insulation Spectroscopy of Induction Machines Using Signal Injection," in *IEEE Transactions on Industry Applications*, vol. 53, no. 2, pp. 1054-1062, March-April 2017, doi: 10.1109/TIA.2016.2639014.

[112] F. Perisse, P. Werynski and D. Roger, "A New Method for AC Machine Turn Insulation Diagnostic Based on High Frequency Resonances," in *IEEE Transactions on Dielectrics and Electrical Insulation*, vol. 14, no. 5, pp. 1308-1315, October 2007, doi: 10.1109/TDEI.2007.4339494.

[113] H. Zhu, C. Morton and S. Cherukupalli, "Quality evaluation of stator coils and bars under thermal cycling stress," *Conference Record of the 2006 IEEE International Symposium on Electrical Insulation*, Toronto, ON, Canada, 2006, pp. 384-387, doi: 10.1109/ELINSL.2006.1665338.

[114] V. Peesapati *et al.*, "Impact of thermal cycling on high voltage coils used in marine generators using FEA methods," *2015 IEEE Electrical Insulation Conference (EIC)*, Seattle, WA, USA, 2015, pp. 434-437, doi: 10.1109/ICACACT.2014.7223543.

[115] S. Pin, S. Dreuilhe, L. Fetouhi, M. Szczepanski, S. Stemmer and G. Belijar, "Lifetime estimation of type I random-wound electrical machines under active thermal cycling," *2022 IEEE Electrical Insulation Conference (EIC)*, Knoxville, TN, USA, 2022, pp. 294-298, doi: 10.1109/EIC51169.2022.9833168.

[116] Madonna, Vincenzo, Paolo Giangrande, and Michael Galea. "Evaluation of strand-to-strand capacitance and dissipation factor in thermally aged enamelled coils for low-voltage electrical machines." *IET Science, Measurement & Technology* 13.8 (2019): 1170-1177.

[117] A. Griffo, I. Tsyokhla and J. Wang, "Lifetime of Machines Undergoing Thermal Cycling Stress," *2019 IEEE Energy Conversion Congress and Exposition (ECCE)*, Baltimore, MD, USA, 2019, pp. 3831-3836, doi: 10.1109/ECCE.2019.8913216.

[118] L. Lusuardi, A. Cavallini, V. Madonna, P. Giangrande and M. Galea, "Unconventional accelerated thermal ageing test for traction electric motors in vehicles," *2020 IEEE Electrical Insulation Conference (EIC)*, Knoxville, TN, USA, 2020, pp. 212-216, doi: 10.1109/EIC47619.2020.9158744.

[119] Y. Long *et al.*, "Effect of Thermal Cycle Ageing on the Breakdown Performance of Epoxy and Its Micro-composites," *2021 IEEE Conference on Electrical Insulation and Dielectric Phenomena (CEIDP)*, Vancouver, BC, Canada, 2021, pp. 113-116, doi: 10.1109/CEIDP50766.2021.9705385.

[120] K. N. Gyftakis, P. A. Panagiotou, N. Lophitis, D. A. Howey and M. D. McCulloch, "Breakdown resistance analysis of traction motor winding insulation under thermal ageing," *2017 IEEE Energy Conversion Congress and Exposition (ECCE)*, Cincinnati, OH, USA, 2017, pp. 5819-5825, doi: 10.1109/ECCE.2017.8096964.

[121] K. N. Gyftakis, M. Sumislawska, D. F. Kavanagh, D. A. Howey and M. McCulloch, "Dielectric characteristics of electric vehicle traction motor winding insulation under thermal ageing,"

2015 IEEE 15th International Conference on Environment and Electrical Engineering (EEEIC), Rome, Italy, 2015, pp. 313-318, doi: 10.1109/EEEIC.2015.7165179.

[122]   P. A. Panagiotou, K. N. Gyftakis, N. Lophitis, M. D. McCulloch and D. A. Howey, "Investigation of traction motor windings' insulation capacitance at switching frequencies under accelerated thermal stress," *2017 IEEE 11th International Symposium on Diagnostics for Electrical Machines, Power Electronics and Drives (SDEMPED)*, Tinos, Greece, 2017, pp. 537-543, doi: 10.1109/DEMPED.2017.8062407.

[123]   D. F. Kavanagh, K. N. Gyftakis and M. D. McCulloch, "Thermal Degradation Phenomena of Polymer Film on Magnet Wire for Electromagnetic Coils," in *IEEE Transactions on Industry Applications*, vol. 57, no. 1, pp. 458-467, Jan.-Feb. 2021, doi: 10.1109/TIA.2020.3040201.

[124]   J. Williams, B. McDermid, T. Reid and M. Nikrandt, "A comparison of the electrical performance of various turn and strand insulation systems before and after rapid thermal cycling," *2014 IEEE Electrical Insulation Conference (EIC)*, Philadelphia, PA, USA, 2014, pp. 407-411, doi: 10.1109/EIC.2014.6869419.

[125]   B. Singh, F. Mauseth, E. Eberg and E. Kantar, "Analysis of Partial Discharge Activity for Multi-Stress Accelerated Aged Stator Bars," *2023 IEEE Electrical Insulation Conference (EIC)*, Quebec City, QC, Canada, 2023, pp. 1-4, doi: 10.1109/EIC55835.2023.10177329.

[126]   M. G. Santos *et al.*, "Continuous Partial Discharges Analysis During Automated Thermal Cycle Aging Experiment," in *IEEE Transactions on Energy Conversion*, vol. 35, no. 4, pp. 1989-1992, Dec. 2020, doi: 10.1109/TEC.2020.3025434.

[127]   A. Shaikh, "Thermal cycling test as a quality control and/or acceptance test for HV form-wound stator coils and bars," *2023 IEEE Electrical Insulation Conference (EIC)*, Quebec City, QC, Canada, 2023, pp. 1-5, doi: 10.1109/EIC55835.2023.10177350.

[128]   D. Train and L. Melia, "A combined voltage-endurance and thermal cycling test for stator coils and bars," *[Proceedings] 1992 Annual Report: Conference on Electrical Insulation and Dielectric Phenomena*, Victoria, BC, Canada, 1992, pp. 679-686, doi: 10.1109/CEIDP.1992.283140.

[129]   G. C. Stone, J. F. Lyles, J. M. Braun and C. L. Kaul, "A thermal cycling type test for generator stator winding insulation," in *IEEE Transactions on Energy Conversion*, vol. 6, no. 4, pp. 707-713, Dec. 1991, doi: 10.1109/60.103645.

[130]   B. K. Gupta, "Effectiveness of thermo-mechanical stress in accelerated aging of turn insulation in motor coils," *Conference Record of the 1992 IEEE International Symposium on Electrical Insulation*, Baltimore, MD, USA, 1992, pp. vol. 79-82, doi: 10.1109/ELINSL.1992.247047.

[131]   H. Mitsui, K. Yoshida, Y. Inoue and S. Kenjo, "Thermal Cyclic Degradation of Coil Insulation for Rotating Machines," in *IEEE Transactions on Power Apparatus and Systems*, vol. PAS-102, no. 1, pp. 67-73, Jan. 1983, doi: 10.1109/TPAS.1983.317999.

[132]   B. K. Gupta, W. T. Fink and R. M. Boggia, "Use of thermal cycling as type test for turn insulation in motor coils," *Proceedings of 1994 IEEE International Symposium on Electrical Insulation*, Pittsburgh, PA, USA, 1994, pp. 107-110, doi: 10.1109/ELINSL.1994.401456.

[133]   W. Xue, Z. Huang, X. Xu, B. Shen and Z. Jin, "Ramping Loss Analysis of No-Insulation HTS Coil Under External Field Using an Improved Equivalent Circuit Model," in *IEEE Transactions on Applied Superconductivity*, vol. 31, no. 8, pp. 1-5, Nov. 2021, Art no. 4902105, doi: 10.1109/TASC.2021.3101779.

[134]   X. Cao, H. Yang and X. Bai, "Equivalent Capacitance Model of Segmented Induction Coil in Electromagnetic Exploration System for Deep Resources," in *IEEE Sensors Journal*, vol. 21, no. 6, pp. 7756-7767, 15 March15, 2021, doi: 10.1109/JSEN.2021.3051477.

[135]   M. Fujieda *et al.*, "Analysis on Surge Voltage in Inverter-fed Motor Using Frequency Response Analysis," *2019 10th International Conference on Power Electronics and ECCE Asia (ICPE 2019 - ECCE Asia)*, Busan, Korea (South), 2019, pp. 1487-1492, doi: 10.23919/ICPE2019-ECCEAsia42246.2019.8797230.

[136]   H. Zhang, S. Wang, D. Yuan and X. Tao, "Double-Ladder Circuit Model of Transformer Winding for Frequency Response Analysis Considering Frequency-Dependent Losses," in *IEEE Transactions on Magnetics*, vol. 51, no. 11, pp. 1-4, Nov. 2015, Art no. 8402304, doi: 10.1109/TMAG.2015.2442831.

[137]   K. Nakahara and F. Kuroki, "Equivalent circuit model of multi-layered coils for integrated sensor applications in medium-wave frequencies," *2016 IEEE International Symposium on Radio-Frequency Integration Technology (RFIT)*, Taipei, Taiwan, 2016, pp. 1-3, doi: 10.1109/RFIT.2016.7578133.

[138]   Z. Zhao, Y. Chen, Y. Yu, M. Han, C. Tang and C. Yao, "Equivalent Broadband Electrical Circuit of Synchronous Machine Winding for Frequency Response Analysis Based on Gray Box Model," in *IEEE Transactions on Energy Conversion*, vol. 36, no. 4, pp. 3512-3521, Dec. 2021, doi: 10.1109/TEC.2021.3081933.

[139]   H. Elmadah, D. Roger and N. Takorabet, "HF model of High Temperature machine coils," *2019 19th International Symposium on Electromagnetic Fields in Mechatronics, Electrical and Electronic Engineering (ISEF)*, Nancy, France, 2019, pp. 1-2, doi: 10.1109/ISEF45929.2019.9097071.

[140]   G. Lv, D. Zeng and T. Zhou, "Analysis of Secondary Losses and Efficiency in Linear Induction Motors With Composite Secondary Based on Space Harmonic Method," in *IEEE Transactions on Energy Conversion*, vol. 32, no. 4, pp. 1583-1591, Dec. 2017, doi: 10.1109/TEC.2017.2717938.

[141]   X. Chen, Z. Zhang, S. Yu and T. -G. Zsurzsan, "Fringing Effect Analysis of Parallel Plate Capacitors for Capacitive Power Transfer Application," *2019 IEEE 4th International Future Energy Electronics Conference (IFEEC)*, Singapore, 2019, pp. 1-5, doi: 10.1109/IFEEC47410.2019.9015111.

[142]   P. Chen, J. Liu, H. Zhang and B. Chu, "Increase of capacitance of thick dielectrics by fringe effect," in *IEEE Transactions on Dielectrics and Electrical Insulation*, vol. 26, no. 5, pp. 1716-1719, Oct. 2019, doi: 10.1109/TDEI.2019.008291.

[143]   Y. Feng, B. Shao, X. Tang, Y. Han, T. Wu and Y. Suzuki, "Improved Capacitance Model Involving Fringing Effects for Electret-Based Rotational Energy Harvesting Devices," in *IEEE Transactions on Electron Devices*, vol. 65, no. 4, pp. 1597-1603, April 2018, doi: 10.1109/TED.2018.2803145.